

Electronic Theses and Dissertations, 2004-2019

2016

Advanced Blue Phase Liquid Crystal Displays

Daming Xu
University of Central Florida

 Part of the [Electromagnetics and Photonics Commons](#), and the [Optics Commons](#)
Find similar works at: <https://stars.library.ucf.edu/etd>
University of Central Florida Libraries <http://library.ucf.edu>

This Doctoral Dissertation (Open Access) is brought to you for free and open access by STARS. It has been accepted for inclusion in Electronic Theses and Dissertations, 2004-2019 by an authorized administrator of STARS. For more information, please contact STARS@ucf.edu.

STARS Citation

Xu, Daming, "Advanced Blue Phase Liquid Crystal Displays" (2016). *Electronic Theses and Dissertations, 2004-2019*. 4926.
<https://stars.library.ucf.edu/etd/4926>

ADVANCED BLUE PHASE LIQUID CRYSTAL DISPLAYS

by

DAMING XU

B.S. Southeast University, 2011

M.S. University of Central Florida, 2015

A dissertation submitted in partial fulfillment of the requirements
for the degree of Doctor of Philosophy
in the College of Optics and Photonics
at the University of Central Florida
Orlando, Florida

Spring Term
2016

Major Professor: Shin-Tson Wu

©2016 Daming Xu

ABSTRACT

Thin-film transistor (TFT) liquid crystal displays (LCDs) have become indispensable in our daily lives. Their widespread applications range from smartphones, laptops, TVs to navigational devices, data projectors and wearable displays. Over past decades, massive efforts have been invested in device development, material characterization and manufacturing technology. As a result, the performance of LCDs, such as viewing angle, contrast ratio, color gamut and resolution, have been improved significantly. Nonetheless, there are still urgent needs for fast response time and low power consumption. Fast response time helps reduce motion image blurs and enable color sequential displays. The latter is particularly attractive since it eliminates spatial color filters, which in turn triples optical efficiency and resolution density. The power consumption can be reduced greatly by using color sequential displays, but liquid crystals with submillisecond response time are required to minimize color breakup. The state-of-the-art gray-to-gray response time of nematic LCDs is about 5ms, which is too slow to meet this requirement.

With the urgent needs for submillisecond response time, polymer-stabilized blue phase liquid crystal is emerging as a strong candidate for achieving this goal. Compared to conventional nematic LCDs, blue phase LCDs exhibit several revolutionary features: submillisecond gray-to-gray response time, no need for alignment layer, optically isotropic voltage-off state, and large cell gap tolerance. However, some bottlenecks such as high operation voltage, low optical transmittance, noticeable hysteresis and slow TFT charging remain to be overcome before their widespread applications can be realized. This dissertation is dedicated to addressing these challenges from material development and device design viewpoints.

First, we started to investigate the device physics of blue phase LCDs. We have built a

numerical model based on the refraction effect for simulating the electro-optics of blue phase devices. The model well agrees with experimental data. Based on this model, we explored approaches from device and material viewpoints to achieve low operation voltage. On the device side, with protrusion and etched electrodes, we can reduce the operating voltage to below 10V and enhance the transmittance to over 80%. On the material side, high Kerr constant is indeed helpful for lowering the operation voltage, but we also need to pay attention to the individual Δn and $\Delta\epsilon$ values of liquid crystal host according to the device structures employed. High- $\Delta\epsilon$ LC hosts help enhance Kerr constant, leading to a reduced operation voltage; but they may be subject to serious capacitance charging issues due to the huge dielectric anisotropy. Our model provides important guidelines for future device design and material development.

To further enhance transmittance and reduce voltage, we have proposed a Z-shaped electrode structure. By optimizing the device structure, we have successfully reduced the operating voltage to $\sim 8V$ and enhanced optical transmittance to $> 95\%$ based on a lower- $\Delta\epsilon$ LC host not subjecting to charging issues, showing comparable or even better performance than the mainstream LCDs. This is the first approach to achieve such a high transmittance in blue phase devices without using a directional backlight. By using zigzag structure, the color shift and gray inversion are in unnoticeable range.

In addition, hysteresis affects the accuracy of grayscale control and should be suppressed. We have proposed a double exponential model to analyze the electric field effects of blue phase, and found that electrostriction effect is the root cause for hysteresis under strong electric field. To suppress the electrostriction effect in blue phase, a method to stabilize the blue phase lattice via linear photo-polymerization is demonstrated for the first time. By illuminating the mono-functional and the di-functional monomers with a linearly polarized UV beam, we can form

anisotropic polymer networks, which in turn lead to anisotropic electrostrictions. In experiments, we found that when the polarization of UV light is perpendicular to the stripe electrodes, the electrostriction effect can be strongly suppressed. The resulting hysteresis is reduced from 6.95% to 0.36% and response time is improved by a factor of two. We foresee this approach will guide future manufacturing process.

The approaches and studies presented in this dissertation are expected to advance the blue phase LCDs to a new level and accelerate their emergence as next-generation display technology. It is foreseeable that the widespread application of blue phase LCDs is around the corner.

To my beloved family.

ACKNOWLEDGMENTS

This dissertation means much more than the typed words to me – it is a milestone achieved after years of dedication. I would like to acknowledge those who took their time to help me in my journey. Without their support and help, my graduate studies wouldn't have been so smooth.

First and foremost, I would like to offer my sincerest gratitude to my Ph.D. advisor, Dr. Shin-Tson Wu, for everything he taught me. It has been such a great honor for me to work under his direct supervision during these fruitful years since he is one of the most eminent experts in the field. I have benefited tremendously from his insightful teachings, visionary suggestions, continuous supports and invaluable inspirations. He also uplifted me by nominating me to win several prestigious society awards, which greatly enhanced my self-esteem. Working with Dr. Wu has not only advanced me in knowledge but has also taught me how to be a better person. In this regard, I believe that the advisor-student relation in our group is like that between family members. I also would like to give my special thanks to Dr. Wu's better half Cho-Yan Hiseh for her care and help during past years. I would like to express my utmost gratitude for everything they have done for me.

I would like to thank Dr. Martin Schadt for his time, insightful discussion and strong support. It's great honor for me to know him and learn from him closely. His wisdom, humbleness and enthusiasm give me a lot of motivations in research and life.

I'm also very grateful to Dr. Qing Li from Southeast University for her tremendous help and support. Without her strong recommendation, I wouldn't have been able to join the current group.

I feel very fortunate to have interacted with all the LCD group members. I would like to

thank Dr. Linghui Rao and Dr. Yuan Chen for teaching me the simulations and experimental skills of liquid crystals. Their dedications to research set a good role model for me to learn from. I want to thank the present and former members of our group, particularly Yifan Liu, Fenglin Peng, Jiamin Yuan, Jing Yan, Haiwei Chen, Guanjun Tan for their support and help. It has been such a great pleasure and privilege for me to work with all of them.

I also want to acknowledge my committee members, Dr. M. G. Moharam, Dr. Patrick LiKamWa and Dr. Jiyu Fang for their delightful conversations and guidance.

Besides, I like to thank my mentors Mr. Tim Large, Dr. Neil Emerton and Dr. John Lutian in Microsoft Applied Sciences Group for their support and inspirations during my internship. They taught me a lot of knowledge beyond my liquid crystal expertise and gave me a chance to achieve the goals in my internship project there.

Lastly I would like to thank my parents, my parents-in-law, and sister, for all their tremendous support and encouragement. My parents have raised me up, educated me well and supported me in all my pursuits. And most of all, I want to thank my loving, supportive and cheerful better half Dr. Siyu Guo for her eternal support and understanding of my goals and aspirations. It is her faithful love and selfless sacrifice that have always strengthened me. Her patience and support will be a treasure throughout my life.

TABLE OF CONTENTS

LIST OF FIGURES	xii
LIST OF TABLES	xvii
CHAPTER 1. INTRODUCTION.....	1
1.1 Basis of Liquid Crystal Display	1
1.2 Background and Motivations	6
CHAPTER 2. MODELING OF BLUE PHASE LIQUID CRYSTAL DISPLAYS	12
2.1 Modeling Physics	12
2.2 Numerical Modeling	16
2.3 Simulation Results.....	19
2.3.1 Simulations vs. Experiments.....	19
2.3.2 Electrode Dimension Effect	22
2.3.3 Cell Gap Effect	25
2.3.4 Saturated Birefringence and Saturation Field Effects.....	28
2.4 Summary	30
CHAPTER 3. LOW VOLTAGE BLUE PHASE LIQUID CRYSTAL DISPLAYS.....	31
3.1 Device Configurations.....	31
3.1.1 Protrusion Electrodes	31
3.1.2 Etched Electrodes.....	34
3.1.3 Blue Phase LCD with Single Gamma Curve	37
3.2 Material Development.....	38
3.3 Summary	40

CHAPTER 4. HIGH TRANSMITTANCE BLUE PHASE LIQUID CRYSTAL DISPLAYS ..	42
4.1 Device Structure.....	42
4.2 Electro-optical Performance.....	43
4.2.1 Voltage-transmittance Characteristics.....	44
4.2.2 Contrast Ratio	46
4.2.3 Color Shift.....	48
4.2.4 Grayscale Inversion	54
4.3 Analysis of Device Parameters	56
4.3.1 Protrusion Height Effect	56
4.3.2 Dimension Effect	58
4.3.3 Electrode Width Effect.....	59
4.3.4 Taper Angle Effect	60
4.4 Variations in Device Structures	62
4.4.1 L-shaped Electrodes.....	62
4.4.2 7-shaped Electrodes	64
4.4.3 I-shaped Electrodes.....	65
4.5 Summary	67
CHAPTER 5. DYNAMIC RESPONSES OF BLUE PHASE LIQUID CRYSTALS.....	68
5.1 Electric Field Effects.....	68
5.2 Experimental Setup	70
5.3 Double Exponential Model	73
5.4 Summary	82
CHAPTER 6. HYSTERESIS-FREE BLUE PHASE LIQUID CRYSTALS STABILIZED BY	

LINEAR PHOTO-POLYMERIZATION.....	83
6.1 Electric Field Effects.....	83
6.2 Polarization Effect.....	86
6.2.1. Hysteresis.....	86
6.2.2. Dynamic Responses.....	89
6.3 UV Intensity Effect.....	90
6.4 Monomer Choice.....	92
6.5 Summary.....	94
CHAPTER 7. SUMMARY.....	95
APPENDIX: STUDENT PUBLICATIONS.....	99
REFERENCES.....	104

LIST OF FIGURES

Figure 1.1. Three thermotropic liquid crystals: smectic, nematic and cholesteric phases.....	2
Figure 1.2. Display system configuration of a transmissive TFT-LCD.....	3
Figure 1.3. Blue phase LC structure at the microscopic level: (a) double-twist alignment of LC molecules; (b) and (c) cubic structures of BP-I; (d) and (e) cubic structures of BP-II. The black lines in (c) and (e) represent disclinations.	8
Figure 2.1. Principle of refraction effect in IPS BPLC.....	14
Figure 2.2. Flowchart of the IPS BPLC device modeling based on refraction effect.....	15
Figure 2.3. Refraction at the boundary between the m^{th} and $(m+1)^{th}$ layers in an IPS BPLC cell.	16
Figure 2.4. Comparison between experimental VT curve and simulated results using Ge's model and the refraction model. BPLC cell: JC-BP06 in IPS-5/5 at 23°C and $\lambda = 633$ nm.	21
Figure 2.5. Simulated transmittance profiles of JC-BP01 in (a, c) IPS-5/5 and (b, d) IPS-10/10 at $\lambda=633$ nm and 23°C. Cell gap $d=7.5$ μm . (a, b): Ge's model, and (c, d): refraction model.	22
Figure 2.6. Simulated VT curves of IPS cells with (a) $G/W = 1$ and (b) $G/W = 2$ using JC-BP01 at 23°C and $\lambda=550$ nm.	23
Figure 2.7. (a) Induced Δn profile of a 10- μm -thick IPS-5/5 cell at 31V and (b) simulated VT curves of IPS-5/5 with different cell gaps. BPLC: JC-BP01 at 23°C and $\lambda = 550$ nm.....	26
Figure 2.8. Transmittance profile of IPS-5/5 with different cell gaps: (a) 5 μm , (b) 7 μm , (c) 8 μm and (d) 10 μm . BPLC: JC-BP01 at 23°C and $\lambda = 550$ nm.	28
Figure 2.9. Simulated VT curves of IPS-2/4 using BPLCs with (a) different Δn_s ($E_s = 4.05$ V/ μm), and (b) different E_s ($\Delta n_s = 0.154$) at 23°C and $\lambda = 550$ nm. Red solid lines: JC-BP01.....	29

Figure 3.1. Cell structure of an IPS BPLC cell using protrusion electrodes.	32
Figure 3.2. Simulated VT curves IPS-2/4 with protrusion electrodes employing (b) JC-BP01 and (c) JC-BP06 ($T = 23^{\circ}\text{C}$ and $\lambda = 550\text{ nm}$).	33
Figure 3.3. Cell structure of an IPS BPLC cell using etched electrodes.	35
Figure 3.4. Simulated VT curves of etched-IPS cells with different electrode dimensions: (b) $G/W = 2$ and (c) $G/W = 3, 4$ and 5 using JC-BP06 ($T = 23^{\circ}\text{C}$ and $\lambda = 550\text{ nm}$).	36
Figure 3.5. (a) Calculated VT curves for RGB wavelengths of etched IPS-2/4 cell. (b) Calculated VT curves for IPS-2/3.6 (R), -2/4 (G), -2/5.2 (B). ($H = 2.5\mu\text{m}$ and $d = 7.5\mu\text{m}$, BPLC: JC-BP06).	38
Figure 4.1. Cross-sectional view of a BPLC cell using Z-shaped electrodes.	43
Figure 4.2. Electrode arrangement in a LCD pixel.	43
Figure 4.3. Calculated VT curves of BPLC cells using Z-shaped electrodes under different G conditions. ($\theta = 90^{\circ}$, $H = 3.5\mu\text{m}$; $W_1 = W_2 = 1.0\mu\text{m}$; $L = 4.0\mu\text{m}$, $\lambda = 550\text{nm}$).	44
Figure 4.4. A summary of the peak transmittance (T_{max}) and on-state voltage (V_{on}) of BPLC cells using Z-shaped electrodes under different G conditions ($L = 4.0\mu\text{m}$, $\lambda = 550\text{nm}$).	45
Figure 4.5. On-state transmittance profile (upper) and the electric potential distribution diagram (lower) of the Z-shaped electrode structure ($L = 4.0\mu\text{m}$, $G = 4.8\mu\text{m}$, $\lambda = 550\text{nm}$).	46
Figure 4.6. Calculated iso-contrast contour of Z-shaped structure (a) without and (b) with biaxial compensation film. ($L = 4.0\mu\text{m}$, $G = 4.8\mu\text{m}$, $\lambda = 550\text{nm}$).	47
Figure 4.7. Normalized emission spectra of a white LED light source (black dashed lines) and transmission spectra of RGB color filters (color curves).	49
Figure 4.8. Top view of (a) stripe shaped electrodes and (b) zigzag shaped electrodes.	52
Figure 4.9. Color shift of RGB primaries film-compensated Z-shaped structure: (a) stripe	

electrodes, (b) zigzag electrodes. The backlight is white LED.....	53
Figure 4.10. Viewing angle dependence of gamma curves for film-compensated Z-shaped BPLC: (a) stripe electrode and (b) zigzag electrode along the diagonal direction ($\varphi = 45^\circ$).	55
Figure 4.11. Calculated VT curves of BPLC cells using Z-shaped electrodes under various heights H conditions ($\theta = 90^\circ$, $W_1 = W_2 = 1.0\mu\text{m}$; $L = 4.0\mu\text{m}$; $G = 4.8\mu\text{m}$, $\lambda = 550\text{nm}$).	56
Figure 4.12. A summary of the peak transmittance (T_{max}) and on-state voltage (V_{on}) of BPLC using Z-shaped electrodes under various heights H conditions ($\lambda = 550\text{nm}$).	57
Figure 4.13. Calculated VT curves of BPLC cells using Z-shaped electrodes under different H conditions. (a) $H = 3.5\mu\text{m}$, (b) $H = 4.5\mu\text{m}$, (c) $H = 2.5\mu\text{m}$ and (d) $H = 1.5\mu\text{m}$ ($\lambda = 550\text{nm}$).	58
Figure 4.14. Calculated VT curves of BPLC cells using Z-shaped electrodes under various electrode width conditions. ($\theta = 90^\circ$, $H = 3.5\mu\text{m}$; $L = 5.0\mu\text{m}$; $G = 6.0\mu\text{m}$, $\lambda = 550\text{nm}$).	60
Figure 4.15. Calculated VT curves of BPLC cells using Z-shaped electrodes under various taper angle conditions. ($H = 3.5\mu\text{m}$, $W_1 = W_2 = 1.0\mu\text{m}$; $L = 4.0\mu\text{m}$; $G = 4.8\mu\text{m}$, $\lambda = 550\text{nm}$).	61
Figure 4.16. A summary of the peak transmittance (T_{max}) and on-state voltage (V_{on}) of BPLC using Z-shaped electrodes under various taper angle conditions ($\lambda = 550\text{nm}$).	61
Figure 4.17. Cross-sectional view of a BPLC cell using L-shaped electrodes.	63
Figure 4.18. Calculated VT curves of BPLC cells using L-shaped electrodes. ($H = 3.5\mu\text{m}$, $\theta = 90^\circ$; $\lambda = 550\text{nm}$).	63
Figure 4.19. Cross-sectional view of a BPLC cell using 7-shaped electrodes.	64
Figure 4.20. Calculated VT curves of BPLC cells using 7-shaped electrodes. ($H = 3.5\mu\text{m}$, $\theta = 90^\circ$; $\lambda = 550\text{nm}$).	65
Figure 4.21. Cross-sectional view of a BPLC cell using I-shaped electrodes.	66

Figure 4.22. Calculated VT curves of BPLC cells using I-shaped electrodes. ($H = 3.5\mu\text{m}$, $\theta = 90^\circ$; $\lambda = 550\text{nm}$).....	66
Figure 5.1. Electric field effects in blue phase liquid crystals.....	70
Figure 5.2. Experimental setup for characterizing the dynamic response of a VFS cell.....	72
Figure 5.3. Transient (a) rise and (b) decay processes of induced birefringence for Sample B at $E = 3\text{V}/\mu\text{m}$	74
Figure 5.4. Fitted rise time constants of (a) Kerr effect t_{r1} and (b) electrostriction effect t_{r2} for samples with different monomer concentrations.....	76
Figure 5.5. Contribution of Kerr effect when different electric fields are applied to samples with different monomer concentrations.....	77
Figure 5.6. Hysteresis loops of Sample A under different electric fields (Solid lines: forward driving, dashed lines: backward driving; $\lambda = 633\text{nm}$).....	78
Figure 5.7. Fitted decay time constants of (a) Kerr effect t_{d1} and (b) electrostriction effect t_{d2} for samples with different monomer concentrations.....	79
Figure 5.8. Contribution of Kerr effect when different electric fields are applied to samples with different monomer concentrations.....	81
Figure 6.1. Chemical structures of monomers employed in our PS-BPLC.....	84
Figure 6.2. Experimental setup of curing process for LPP-stabilized blue phases.....	86
Figure 6.3. Measured hysteresis loops of Samples 1-3 (Solid lines: forward driving, dashed lines: backward driving; $\lambda = 633\text{nm}$).....	87
Figure 6.4. LPP-induced polymer network in (a) Sample 1 and (b) Sample 2.....	88
Figure 6.5. Transient decay process of Sample 2 at 56.2V.....	90
Figure 6.6. Hysteresis loops of IPS cells under different UV illumination intensities (Solid lines:	

forward driving, dashed lines: backward driving; $\lambda = 633\text{nm}$). 91

Figure 6.7. Measured hysteresis loops of Samples 4-6 (Solid lines: forward driving, dashed lines:
backward driving; $\lambda = 633\text{nm}$). 93

LIST OF TABLES

Table 2.1. Comparison between refraction and Ge's models for IPS BPLC cells with $G/W = 1$. BPLC: JC-BP01 at 23°C and $\lambda = 550 \text{ nm}$	24
Table 2.2. Comparison between refraction model and Ge's model for IPS BPLC with $G/W = 2, 3$ and 4 structures. BPLC: JC-BP01 at 23°C and $\lambda = 550 \text{ nm}$	25
Table 5.1. Material recipes and cell gap of three samples.	71
Table 6.1. Measured operation voltage, hysteresis and response time of Samples 1-3.	88
Table 6.2. Fitted time constants and contribution of electrostriction effect for Samples 1-3.	90
Table 6.3. Measured operation voltage, hysteresis and response times of IPS cells under different UV illumination intensities.	92
Table 6.4. Measured operation voltage, hysteresis, and response time of Samples 4-6.	94

CHAPTER 1. INTRODUCTION

1.1 Basis of Liquid Crystal Display

The explosive growth of personal electronic devices has nourished rapid development of display technologies. Display is the most directly perceived feature of electronic devices and therefore has become a key factor for consumers when choosing electronic devices. Nowadays, various display technologies, such as liquid crystal display (LCD), organic light-emitting diode (OLED), LED, electronic ink (e-ink) and plasma display panel (PDP) co-exist in the consumer market [1]. Among these technologies, active matrix LCD is the prevalent one owing to its high resolution, full color, excellent contrast ratio, wide viewing angle, low price, and long lifetime. As a matter of fact, LCDs have become indispensable in our daily lives, and their widespread applications range from smartphones, tablets and laptops to desktop monitors, navigational devices, TVs, and data projectors.

In LCDs, the core and most distinctive component is liquid crystal (LC). Liquid crystals have a history of over 100 years. In 1888, an Austrian botanist Friedrich Reinitzer discovered liquid crystals [2]. Liquid crystal is an intermediate state of matter between isotropic fluids and crystalline solids. It can also be viewed as a liquid in which an ordered arrangement of molecules exists [3, 4]. Based on different orderings of molecules and their optical properties, thermotropic liquid crystals can be categorized into smectic, nematic, and cholesteric phases [4], as illustrated in [Figure 1.1](#). Among them, nematic phase has been widely used in displays owing to its advantages of simple alignment, low viscosity, low driving voltage, etc. Nematic liquid crystals exhibit a variety of states as temperature increases: from solid to anisotropic liquid crystal, to

isotropic liquid when thermal energy deteriorates the delicate cooperative ordering of the LCs, and finally to vapor phase [3, 5].

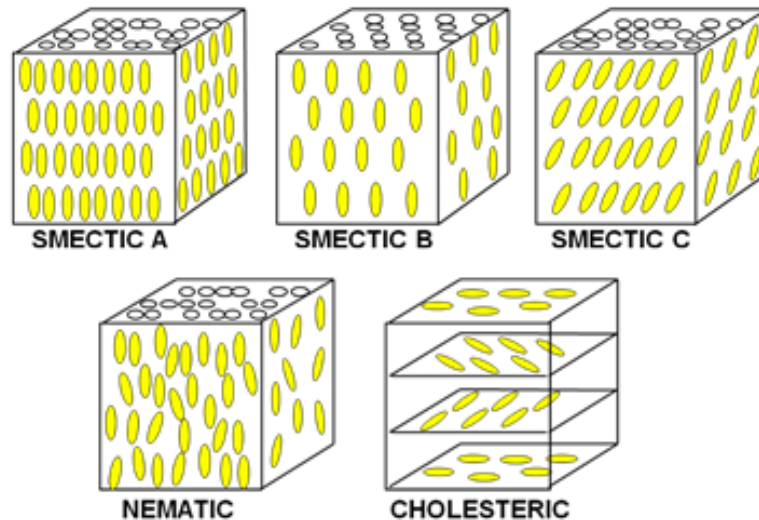


Figure 1.1. Three thermotropic liquid crystals: smectic, nematic and cholesteric phases.

Although liquid crystals were discovered a long time ago, their display applications hadn't been realized until G. H. Heilmeyer developed the first liquid crystal display using dynamic scattering mode (DSM) in the mid-1960s [6]. However, the DSM didn't reach a commercial success due to some technical issues (e.g. high driving voltage, short lifetime, etc.). To address the stability issue of the DSM, the twisted nematic (TN) mode was invented in the 1970s [7]. This is a milestone for display technologies as it changed the development direction and opened the gateway for widespread applications of LCDs. In the following decades, with massive efforts invested in device development, material characterization and manufacturing technology, the LCD industry has boomed tremendously. To improve resolution, the super-twisted-nematic LCDs [8, 9] were invented; to widen the viewing angle and increase the contrast ratio, in-plane switching (IPS) mode [10] and vertical alignment (VA) mode [11] were developed; to achieve high optical efficiency and enable touch panel applications, the fringe field switching (FFS) mode [12, 13] was

developed in the 1990s and then implemented in the 2000s. The LCD industry has been continually advanced by technology innovations.

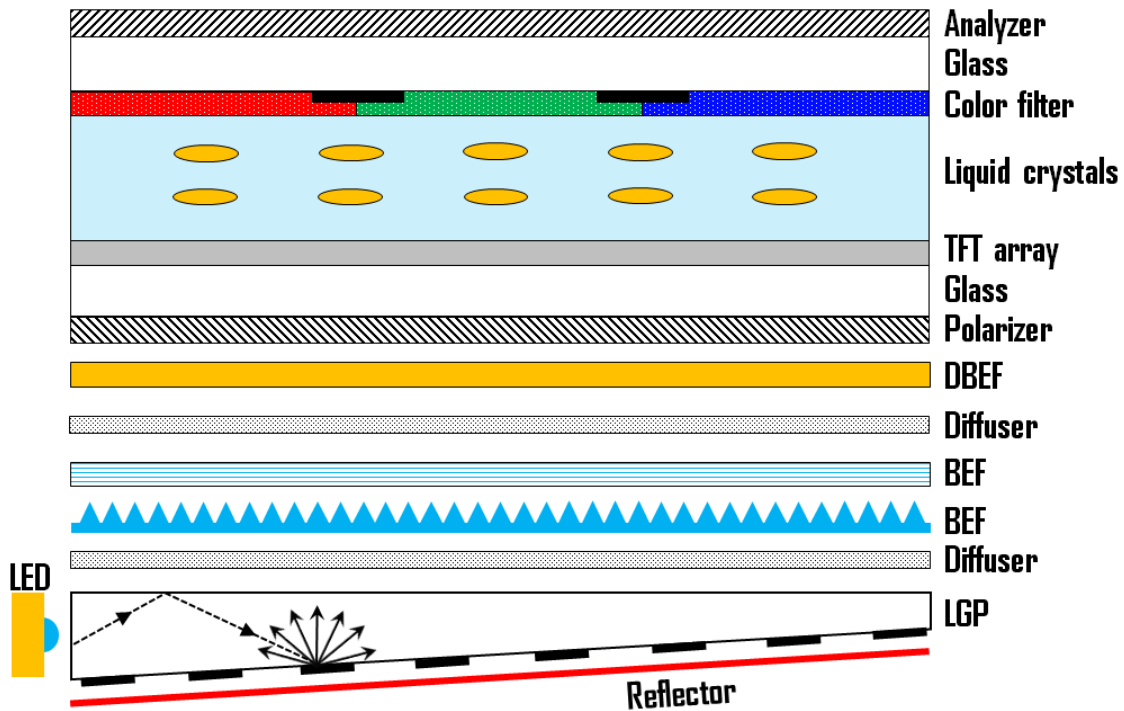


Figure 1.2. Display system configuration of a transmissive TFT-LCD.

Figure 1.2 illustrates the typical system configuration of a transmissive LCD. Since LCD is non-emissive and liquid crystals only work as a light valve to tune the transmission, a light source is required to illuminate the LCD panel so that viewers can see the image displayed on the panel. The backlight is therefore a critical element of the display system, and in fact it directly determines many key optical properties of the panel, such as color rendition, viewing angle, contrast, and brightness. At early stage of LCD development, cold-cathode fluorescent lamp (CCFL) was a commonly used light source in LCD laptops and monitors. As technology advances, light-emitting diode (LED) has become increasingly prevalent since it offers tremendous performance advantages over CCFL in larger color gamut, higher brightness, smaller volume, real-

time color management and lower power consumption [14-16].

Regarding the backlight configuration, two commonly used backlight methods are direct-lit and edge-lit types. As its name implies, the direct-lit backlight consists of an array of light-sources directly placed behind the LCD panel. In order to obtain acceptable brightness uniformity, the light sources should not be too widespread and their positions should not be too close to the LCD panel. As a result, the volume of the backlight unit is fairly bulky. In contrast, the edge-lit backlight consists of several light sources placed along the edge of display, as depicted in [Figure 1.2](#). The light-guide plate (LGP) distributes the light from the light sources uniformly over the surface, typically by using a dot-pattern or microstructure extractor array. By using LGP, the total thickness of the edge-lit backlight unit can be reduced dramatically, and the output light has a very high uniformity. Thus, the edge-lit backlight has become the prevalent backlight technology in high-end and portable LCD devices.

Behind the LGP placed a back reflector to redirect the backward-travelling light towards the panel. A diffusive reflector helps scramble the polarization state of the light, which can boost efficiency in system incorporating linear reflective polarizers. It also randomizes the direction of reflected light, which can improve the uniformity of the output light. Meanwhile, multiple reflections off the back reflector necessitate high reflectivity for optimal performance. An example is 3M's enhanced specular reflector, which has a typical reflectivity $> 98\%$ [17].

Light exiting the LGP usually exhibits following features: large angle, unpolarized, and may be both spatially and angularly non-uniform. Hence, a stack of optical films is required to mitigate these issues. These may include diffuser sheets, micro-prismatic films and a reflective polarizer. A diffuser with high haze is directly placed above the LGP in order to hide light guide extraction features and further enhance the light uniformity. Then, the light goes through brightness

enhancement film (BEF) so that the on-axis transmittance is enhanced. The BEF utilizes a unique random prismatic structure to recycle the diffused light into the backlight and directs the light through the LCD, thereby providing enhanced brightness toward the on-axis viewers [18, 19]. Depending on applications, one or two BEFs may be used. For instance, a single sheet of BEF is ideal for LCD panels in monitors and TVs, while crossed BEF sheets are widely used in mobile displays and laptops. Then, a low-haze diffuser is placed above the BEF(s) in order to hide prism film features as well as moiré caused by interference between the periodicity of crossed BEFs. Since the light exiting the diffuser is unpolarized, more than 50% of the light will be absorbed by the crossed sheet polarizers. In order to reduce the loss, a reflective polarizer is usually used [20, 21]. When the unpolarized backlight hits the reflective polarizer, one linear polarization (say, p -wave) will pass through while the other component (s -wave) will be reflected back to the backlight unit for recycling. After hitting the rough surface of the diffuser, the s -wave is depolarized. Upon reflection from the diffusive reflector, the p -wave is transmitted and s -wave is reflected again for recycling on the return trip. A reflective polarizer widely implemented in commercial LCDs is dual brightness enhancement film (DBEF, 3M Company) [22, 23], which can improve the brightness by ~60%.

After passing through a stack of optical sheets, the light enters the LCD panel. In the panel, the liquid crystal layer is interposed between two glass substrates, which can be further sandwiched between two crossed polarizers. On the rear substrate, a thin-film-transistor (TFT) array is formed to provide an independent switch for each pixel. In each refresh frame, signals from the gate lines turn on the TFTs in a scanning sequence, and the voltages from the data lines are applied to drive each individual liquid crystal pixel to the targeted gray level. On the front substrate, a color filter layer is formed and aligned with the rear TFT pixels for achieving a full-color display. Under such

a spatial RGB subpixel configuration, different colors are achieved by combining the separate colors from RGB subpixels at assigned gray level.

In the LCD system, due to the loss of optical sheets, polarizer, color filters, TFT aperture ratio, only ~6% of light emitted by the light sources can be perceived by human eye. For example, two open polarizers only transmit ~45% of the light. The transmission of the color filter layer is even lower (~30%) since each RGB color filter only transmits one color and absorbs the other two.

1.2 Background and Motivations

Over the past decades, the performance of LCDs has been improved dramatically by continuous development of new technologies. The most critical issue on viewing angle has been addressed by using multi-domain structures [24] and optical film compensation [25, 26]. The contrast ratio has exceeded one million-to-1 through local dimming of the LED backlight [27, 28]. The color gamut would reach over 90% of Rec. 2020, if quantum-dot backlight are implemented [29, 30]. The resolution has been improved significantly by using high-mobility TFT materials such as low-temperature polycrystalline silicon (LTPS) and indium gallium zinc oxide (IGZO) [31-34]. Besides these technological advances, the cost has also been reduced dramatically owing to the improvement of manufacturing lines. Nonetheless, there are still urgent needs for fast response time and low power consumption.

Fast response time helps reduce motion image blurs [35-37] and enable color sequential displays using RGB LED backlights [38, 39]. It is well known that motion images are blurred when they are displayed on TFT LCDs. Such blurring is an artifact on image quality and is a serious issue affecting the performance of LCD TVs. The causes of the motion blur are twofold: 1) sample-and-hold effect of TFTs, and 2) slow response time of liquid crystal. On the other hand,

the color sequential displays are particularly attractive since it eliminates spatial color filters, which in turn triples the optical efficiency and resolution density. Higher optical efficiency leads to lower power consumption, which has been emphasized in all electronic devices. In particular, for portable devices, low power consumption is highly desirable for extending the battery life. In spite of these attractive features, color sequential displays require the response time of liquid crystals to be less than one millisecond in order to minimize color breakup. This imposes a big challenge to nematic liquid crystals. To reduce liquid crystal response time, various approaches have been developed, such as thin cell gap [40, 41], overdrive and undershoot voltage [42, 43], bend cell [44, 45], low viscosity LC materials [46, 47], etc. However, the state-of-the-art response time of nematic LCDs is around 2-3ms. Hence, developing LCDs with submillisecond response time is still in need and the emerging blue-phase liquid crystal (BPLC) is a strong candidate for achieving this goal.

Blue phase (BP) is a mesophase between chiral nematic (N^*) and isotropic phases. Although BP was first discovered by in 1888 [2], due to the narrow temperature range (0.5-2K) it was not until 1970s when BP gained popularity. Tremendous progress has been made to understand the underlying physics of BP since then. It was found that BP is optically isotropic while exhibiting unusually strong optical activity. Based on this phenomenon, Saupe proposed that BP has cubic superstructures [48]. Afterwards, many efforts were devoted to explore the BP structures, both experimentally and theoretically [49-51]. [Figure 1.3\(a\)](#) illustrates how the LC molecules are arranged in BP structures: the LC directors form a double-twist alignment in a cylinder and all the helical axes formed by LC directors are perpendicular to the center line. Although in reality there is an unlimited number of such helical axes, here we just use two of them to illustrate the molecular orientation in the double-twist structure. This structure only extends a small distance (usually ~ 100

nm, depending on the pitch length of the chiral dopant) with the boundary molecules aligned at 45° to the middle line. As temperature increases, up to three phases: BP-I, BP-II, and BP-III may exist. While BP-III possesses amorphous structure [52], BP-I and BP-II are comprised of cubic lattices fitted by the double-twist cylinders [3], as shown in Figures 1.3(b) and 1.3(d). However, these cylinders cannot fill the full space without defects. Thus, BP is a coexistence of double-twist cylinders and disclinations. Defects occur at the points where the cylinders are in contact, as Figures 1.3(c) and 1.3(e) depict. These defects tend to make the structure less stable, resulting in a narrow temperature range.

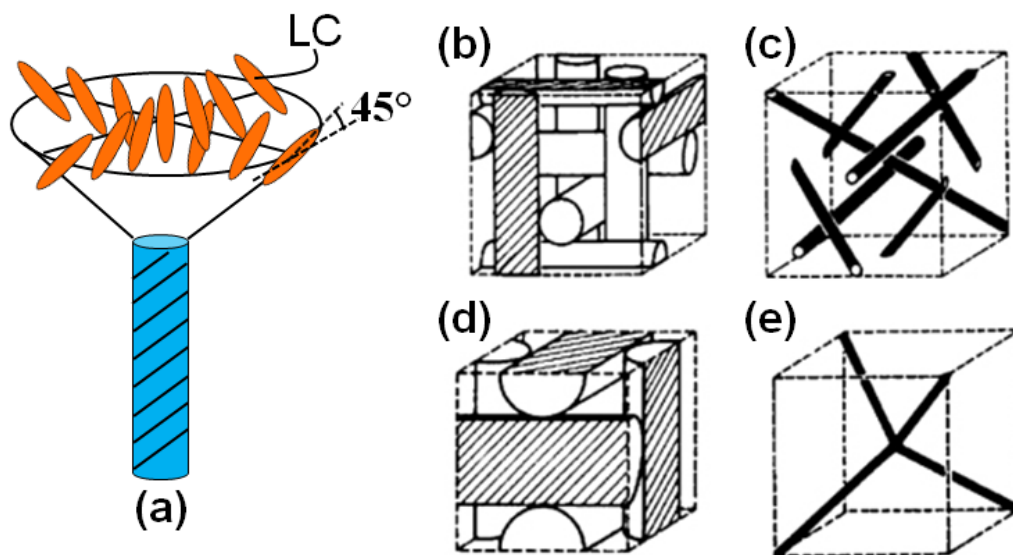


Figure 1.3. Blue phase LC structure at the microscopic level: (a) double-twist alignment of LC molecules; (b) and (c) cubic structures of BP-I; (d) and (e) cubic structures of BP-II. The black lines in (c) and (e) represent disclinations.

The most distinctive feature of BP is selective reflection of incident light. In early investigations, BP exhibited blue color, and this is why it was termed blue phase liquid crystal since then. However, BP liquid crystals are not always blue; they may reflect other colors, depending on the pitch length of the periodical structure. Different from chiral nematic phase, the

Bragg reflection wavelength of BP is expressed as [50]:

$$\lambda = \frac{2na}{\sqrt{h^2 + k^2 + l^2}}, \quad (1.1)$$

where n and a denote average refractive index and lattice constant of blue phases, and h , k , and l are the Miller indices. In BP-I, the lattice constant corresponds to one pitch length and diffraction peaks appear at (110), (200), and (211), etc. The summation of Miller indices $h + k + l$ is an even number. In BP-II, the lattice constant corresponds to one half of a pitch length and diffraction peaks appear at (100), (110), etc. [50] The BP pitch length is slightly different from that of chiral nematic phase. The reflection bandwidth is also much narrower than that of cholesteric liquid crystals.

At voltage-off state, BP appears optically isotropic if its Bragg reflection is in the UV region. Hence, when the device is sandwiched between two crossed polarizers, an excellent dark state can be obtained. Upon application of an electric field, the isotropic medium becomes anisotropic, and the induced birefringence can be characterized by the Kerr effect [53]. This isotropic-to-anisotropic switching can be completed in submillisecond range owing to the nanoscale double-twist cylinder diameter and short coherence length of BP. As the applied voltage increases, the induced birefringence increases, and consequently the transmittance gradually increases.

BP has been explored for several decades; however, the BP temperature range (1-2 °C) was too narrow for practical applications. To widen BP temperature range, Kikuchi *et al.* [54] proposed an approach to cross-link polymer networks in the disclination lines to stabilize the BPLC lattice structure. This method can extend the BP temperature range to more than 60K (260-326K), including room temperature. This paved the way for the widespread applications of BP liquid crystals [55].

In terms of device configuration, both in-plane-switching (IPS) [56, 57] and vertical field switching [58, 59] have been developed. Between these two, IPS is commonly employed because of its simpler backlight system. In an IPS cell, electric field is mainly in lateral direction and the Kerr-effect-induced birefringence is along the electric field direction if a LC host with positive dielectric anisotropy ($\Delta\epsilon > 0$) is employed. Compared to mainstream nematic LCDs, blue phase LCDs exhibit several revolutionary features:

- 1) The BP has self-assembled three-dimensional lattice structure. As a result, no surface alignment layer is required and the fabrication process can be simplified.
- 2) The BP lattice structures have nanoscale double-twist cylinder diameter and short coherence length, which result in submillisecond response time.
- 3) The dark state of a blue phase LCD is optically isotropic. This leads to an intrinsically high contrast ratio and wide viewing angle.
- 4) In IPS structures, the transmittance is insensitive to the cell gap, as long as the cell gap exceeds the penetration depth of electric field. This feature is particularly attractive for the fabrications of large-panel LCDs, in which cell-gap uniformity is a big concern. Meanwhile, the cell-gap insensitivity can enable touch functionality so that the display image quality wouldn't be deteriorated by the touch pressure.

Although IPS blue phase liquid crystals possess so many promises, some tough technical issues remain to be overcome before widespread applications can be realized. The major challenges lie in four aspects: (1) the operation voltage is still too high ($\sim 50\text{V}$); (2) the transmittance is relatively low ($\sim 65\%$); (3) slow charging issue due to the large capacitance, and (4) relatively large hysteresis as well as prolonged response times, especially in the strong electric field region.

High operation voltage originates from the fact that the electric fields are confined near the IPS electrodes and cannot penetrate deeply into the BPLC bulk [60]. Low transmittance results from the “dead zones” on the top of the electrodes since only the horizontal electric field contributes to the transmittance of the IPS BPLC cell. The hysteresis is a consequence of BP lattice deformation under strong electric field [61]. On the other hand, unlike conventional nematic LCs, blue phase demands an unusually large dielectric anisotropy ($\Delta\epsilon > 100$) to achieve low voltage operation. Such a huge $\Delta\epsilon$ produces a large capacitance (C_{LC}), leading to insufficient charging capability in conventional pixel circuit, i.e. the voltage applied to the LC capacitor cannot reach the desired value within the designated charging time. As a result, the optical efficiency is lowered [62]. In order to solve these issues, efforts from device development and material characterization sides are urgently needed.

In this dissertation, electro-optic properties of blue phase liquid crystals are studied. A computation numerical model is developed to understand the underlying device physics of blue phase LCDs. Parameters affecting the device performance, such as electrode dimension and cell gap are investigated. The device physics study provides a guideline to the optimization of blue phase liquid crystal devices. New device configurations are proposed to achieve low operation voltage as well as high transmittance, and eliminate the charging issue. Moreover, the generation mechanisms of hysteresis are investigated quantitatively. It is found that the electrostriction effect is the root cause of hysteresis and slow response time under strong electric field. To suppress the electrostriction effect, an effective approach is proposed to stabilize the blue phase lattice via linear photo-polymerization. These approaches will undoubtedly advance the blue phase LCDs to a new level and accelerate their emergence as next-generation displays.

CHAPTER 2. MODELING OF BLUE PHASE LIQUID CRYSTAL DISPLAYS

To reduce operation voltage, approaches from both device design [60, 63-66] and material development [67-70] sides have been proposed. With these combined effects, the on-state voltage can be reduced to <10V. However, the transmittance is still limited to 65-70%. Therefore, there is an urgent need to develop BPLC devices to achieve high optical transmittance and low operation voltage simultaneously.

Meanwhile, Chen, *et al.* [71] observed an interesting phenomenon during the study of electrode dimension effects on BPLC using IPS electrodes. It was reported that by reducing the width (W) and gap (G) of the IPS electrodes, the operation voltage is reduced while the transmittance is maintained at > 80%. Such a high transmittance couldn't be explained by the model developed by Ge, *et al.* [56, 57]. IPS-2/4 ($W = 2\mu\text{m}$ and $G = 4\mu\text{m}$), IPS-5/10 and IPS-5/5 are able to achieve over 80% transmittance in experiments; in contrast, in Ge's model, the peak transmittance for $G/W = 1$ and 2 device configurations are only ~50% and ~64%, respectively. More recently, Chen, *et al.* [69] reported a peak transmittance ~60% for IPS-5/5 cell in experiments. Thus, Ge's model predicts a lower transmittance than the experimental data.

In this chapter, we develop a refraction model to explain the dimension effect of IPS BPLC and obtain good agreement with experimental data. Based on this model, the electro-optical characteristics of the IPS BPLC are discussed.

2.1 Modeling Physics

In Ge's model, the incident light is assumed to travel along straight lines in an IPS cell. On

the top of interdigitated electrodes, the electric fields are mainly in the vertical direction. Thus, the transmittances in these regions are very low, known as “dead zones” [57]. Let us take IPS-5/5 cell as an example. According to this model, at the full-bright state it should have bright and dark lines with almost the same width. However, it was reported by Chen, *et al.*[71] that the effective aperture ratio for the IPS-5/5 sample is ~75% instead of ~50%. This oversized bright region indicates that the LCs near the edges of ITO electrodes also contribute to the overall transmittance. To explain this increased aperture ratio, a new model is needed.

For intensity modulation, an IPS BPLC cell is placed between two crossed linear polarizers. The electric fields generated from interdigitated pixel electrodes are used to induce phase retardation for the incident light. At the voltage-off state ($V = 0$), BPLC is optically isotropic (refractive index n_i) and thus showing to a very good dark state [72]. When an electric field E is applied, the induced birefringence is along the direction of electric field. Macroscopically speaking, such an isotropic-to-anisotropic transition is governed by the Kerr effect [53] and the induced birefringence can be characterized by the extended Kerr model [73]:

$$\Delta n = \Delta n_s \left(1 - \exp \left[- \left(\frac{E}{E_s} \right)^2 \right] \right), \quad (2.1)$$

where Δn_s stands for saturated induced birefringence and E_s the saturation electric field.

According to [Equation \(2.1\)](#), the induced birefringence depends on the electric field in an IPS BPLC cell. Consequently, at a voltage-on state the ordinary index (n_o) and extraordinary index (n_e) should be different at different positions of the cell. As a result, the BPLC in an IPS cell cannot be assumed as a uniform medium and the incident light would not propagate in a straight path. In our refraction model, we take the non-uniform BPLC profile into account so that the light propagation is changed by the refraction effect. In particular, on top of the electrodes, incident light

would be refracted toward the center of the electrodes, as illustrated in Figure 2.1. These refracted rays propagate at a larger angle with respect to the optic axis of BPLC. Meanwhile, the optical path in the BPLC layer becomes longer due to the bent propagation direction. These two factors concurrently lead to an enhanced phase retardation on top of the IPS electrodes, resulting in a higher transmittance at these regions.

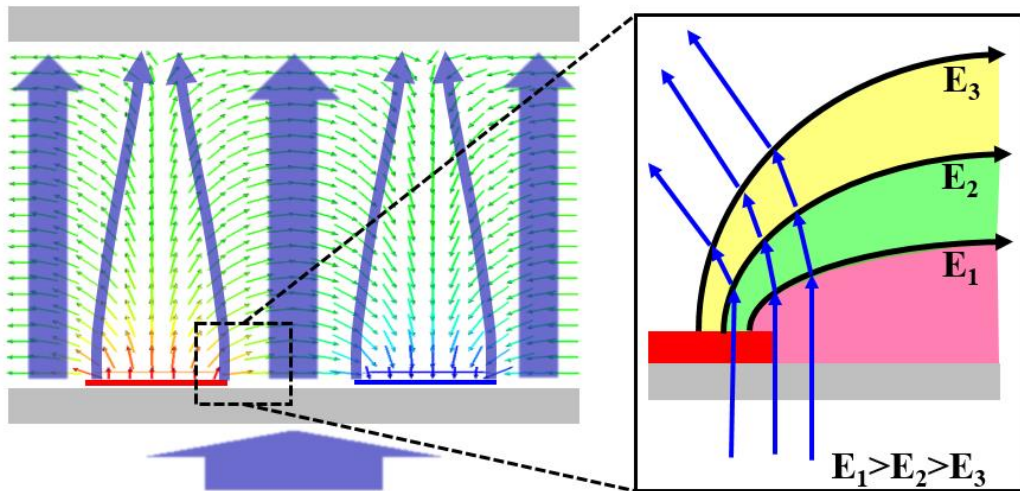


Figure 2.1. Principle of refraction effect in IPS BPLC

Based on the descriptions above, we propose the following flowchart to model the refraction effect in an IPS BPLC cell, as Figure 2.2 depicts. First, we compute the potential distribution by solving the Poisson equation and then the distribution of electric field in the media. This step can be completed with commercial software such as DIMOS.2D (Autronic-Melchers, Germany) or TechWiz LCD (Sanayi System Co., Korea). In our simulations, we use the electric potential data exported from DIMOS.2D. To simulate the refraction effect accurately, we divide the cell into multiple layers with each layer thickness of $0.1 \mu\text{m}$. The mesh size on the horizontal direction is $0.05 \mu\text{m}$. Next, we further calculate the induced birefringence distribution from Equation (2.1) and following equations [73]:

$$n_o = n_i - \frac{1}{3} \Delta n; \quad (2.2a)$$

$$n_e = n_i + \frac{2}{3} \Delta n. \quad (2.2b)$$

After obtaining \mathbf{E} , n_e and n_o , we assign the local optic axis direction of each unit along the local \mathbf{E} vector. Then we compute the ray tracings of transverse electric (known as TE) and transverse magnetic (known as TM) polarizations; calculate their phase change and then phase retardation. We add this step to Ge's model in order to take refraction effect into account, and the detailed description of this step will be explained in next section. With the phase retardation, we are able to compute the electro-optical characteristics, such as voltage-transmittance (VT) curve.

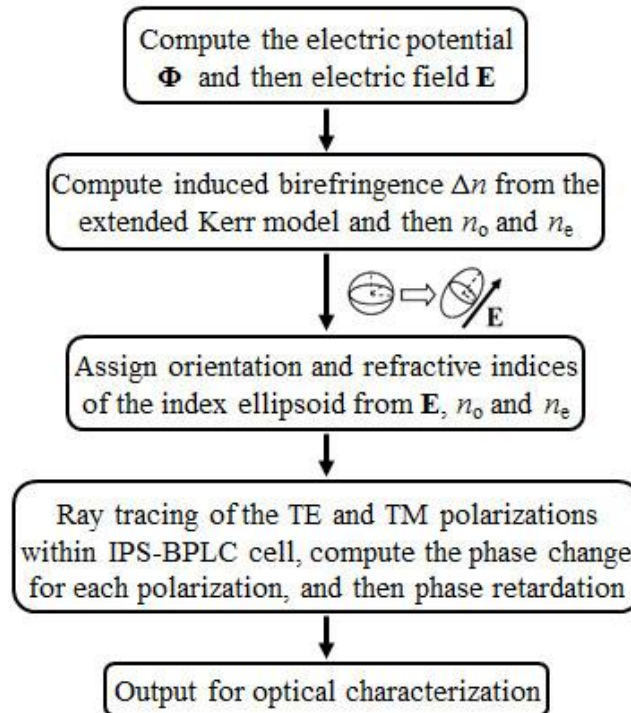


Figure 2.2. Flowchart of the IPS BPLC device modeling based on refraction effect.

2.2 Numerical Modeling

When a light ray passes through the boundary of two uniform isotropic media, the refraction effect is governed by the Snell's law. However, at a voltage-on state the incident light propagates in an anisotropic BPLC medium so that the e-ray (TM) and o-ray (TE) should be considered separately. Since the polarizer is oriented at 45° with respect to the IPS electrodes, the incident linearly polarized light can be decomposed into 50% TE and 50% TM polarizations. Let's take two arbitrary adjacent layers, the m^{th} and $(m+1)^{\text{th}}$ layers, as an example. Here, the m^{th} layer is closer to the bottom substrate, as shown in Figure 2.3.

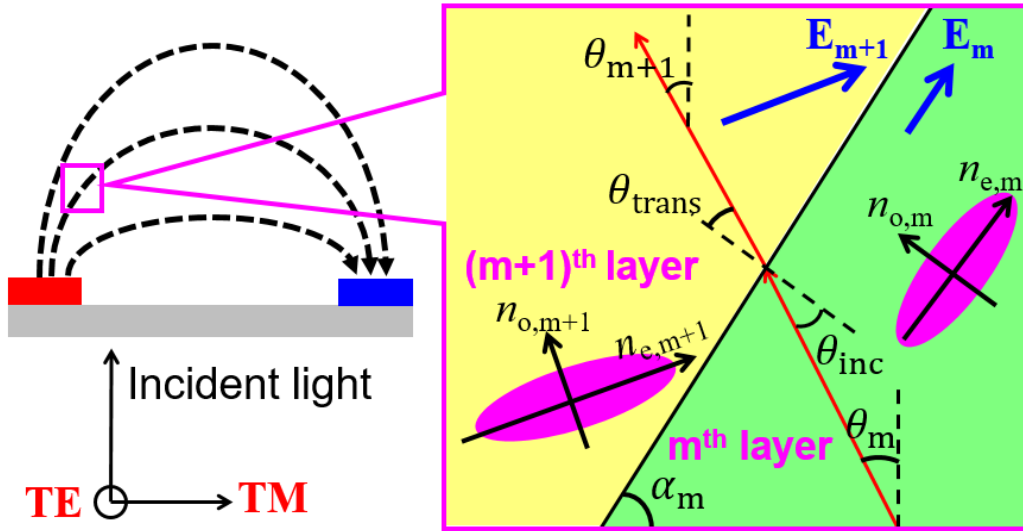


Figure 2.3. Refraction at the boundary between the m^{th} and $(m+1)^{\text{th}}$ layers in an IPS BPLC cell.

For TE polarization, it experiences an ordinary refractive index n_o . At the interface between these two layers, the incident angle is:

$$\theta_{inc} = \theta_m + \alpha_m, \quad (2.3)$$

where θ_m is the angle between incident light and vertical direction, and α_m is the inclination angle between the electric field (E_m) and the horizontal axis.

Let us assume $n_{o,m}$ and $n_{o,m+1}$ represent the ordinary refractive indices of the m^{th} and $(m+1)^{th}$ layers, respectively. Since TE polarization is an ordinary wave here [74], its refraction effect is still governed by the Snell's law:

$$n_{o,m+1} \sin \theta_{trans} = n_{o,m} \sin \theta_{inc}. \quad (2.4)$$

Meanwhile, the m^{th} layer is closer to the electrodes and consequently the electric field intensity in this layer is stronger. According to [Equations \(2.1\) and \(2.2\)](#), stronger electric field intensity leads to a higher induced birefringence and lower n_o . As a result, the angle of transmission θ_{trans} in the $(m+1)^{th}$ layer is smaller than the incident angle θ_{inc} in the m^{th} layer. In the electrode gap regions, the electric field is nearly horizontal so that θ_{inc} is very small and the refraction effect is negligible, as [Equation \(2.4\)](#) indicates. In contrast, on top of the interdigitated electrodes, electric field components along the vertical direction are pretty strong. Hence, θ_{inc} is larger and the light is bent toward the center of electrodes.

The phase change of TE polarization in the m^{th} layer can be written as:

$$\varphi_{TE,m} = 2\pi \cdot n_{o,m} \cdot t_{TE,m} / \lambda, \quad (2.5)$$

where $t_{TE,m}$ is the optical path of TE polarization in the m^{th} layer. The propagation direction of TE polarization in the $(m+1)^{th}$ layer with respect to the vertical direction is:

$$\theta_{m+1} = \theta_{trans} - \alpha_m. \quad (2.6)$$

Then, we plug [Equation \(2.6\)](#) into [Equation \(2.3\)](#) and iterate the process for computing the refraction effect of TE polarization in next two layers until the rays arrive at the top substrate.

For TM polarization, the situation is more complicated. The incident angle at the interface between these two layers can still be calculated by [Equation \(2.3\)](#). However, since the electric field of TM polarization is in the plane of incidence, it's an e-ray propagating in an anisotropic media

[74]. Hence, Snell's law is not applicable to calculate its angle of transmission. The wave vector \mathbf{k}_m in the m^{th} layer should be determined by following equations:

$$\frac{k_{\perp C_m, m}^2}{n_{e, m}^2} + \frac{k_{\parallel C_m, m}^2}{n_{o, m}^2} = k_0^2, \quad (2.7a)$$

$$\tan \theta_{inc} = k_{\parallel C_m, m} / k_{\perp C_m, m}, \quad (2.7b)$$

where $k_{\perp C_m, m}$ and $k_{\parallel C_m, m}$ are the components of wave vector \mathbf{k}_m normal and parallel to the direction of optic axis C_m , which is also the direction of electric field in the m^{th} layer. And $n_{e, m}$ and $n_{o, m}$ are the extraordinary and ordinary refractive indices of the m^{th} layer, respectively. After obtaining $k_{\perp C_m, m}$ and $k_{\parallel C_m, m}$, the normal-to- C_m component of wave vector in the $(m+1)^{\text{th}}$ layer $k_{\perp C_m, m+1}$ can be determined according to the boundary matching of tangential wave vectors [74]:

$$k_{\parallel C_m, m+1} = k_{\parallel C_m, m}. \quad (2.8)$$

To calculate the wave vector in the $(m+1)^{\text{th}}$ layer, we need to do a coordinate transformation as shown below:

$$\begin{bmatrix} k_{\perp C_{m+1}, m+1} \\ k_{\parallel C_{m+1}, m+1} \end{bmatrix} = \begin{bmatrix} \cos \beta & -\sin \beta \\ \sin \beta & \cos \beta \end{bmatrix} \cdot \begin{bmatrix} k_{\perp C_m, m+1} \\ k_{\parallel C_m, m+1} \end{bmatrix}, \quad (2.9)$$

Here, $\beta_m = \alpha_{m+1} - \alpha_m$ is the angle between optic axes in the $(m+1)^{\text{th}}$ and m^{th} layers. Then we plug Equation (2.9) into the following equation for determining the wave vector \mathbf{k}_{m+1} :

$$\frac{k_{\perp C_{m+1}, m+1}^2}{n_{e, m+1}^2} + \frac{k_{\parallel C_{m+1}, m+1}^2}{n_{o, m+1}^2} = k_0^2. \quad (2.10)$$

By solving Equations (2.9) and (2.10), we can obtain $k_{\perp C_m, m+1}$. The phase change of TM polarization in the m^{th} layer is:

$$\phi_{TM,m} = \frac{2\pi}{\lambda} n_{eff,m} t_{TM,m}, \quad (2.11)$$

where $n_{eff,m}$ is the effective refractive index and $t_{TM,m}$ is the optical path of TM polarization in the m^{th} layer, respectively.

The direction of TM polarization in the $(m+1)^{th}$ with respect to the vertical direction is:

$$\theta_{m+1} = 90^\circ - \tan^{-1} \left(\frac{k_{\perp C_m, m+1}}{k_{\parallel C_m, m+1}} \right) - \alpha_m. \quad (2.12)$$

To iterate the process, we plug Equation (2.12) into Equation (2.3) and calculate Equations (2.7) - (2.12) again for computing the refraction effect of TM polarization for the next two layers until the rays arrive at the top substrate.

After computing the phase change for TE and TM in each layer, following equations are used to calculate the phase retardation and transmittance T of light:

$$\Gamma = \sum_m \phi_{TM,m} - \sum_m \phi_{TE,m}, \quad (2.13)$$

$$T = \sin^2(\Gamma / 2). \quad (2.14)$$

2.3 Simulation Results

2.3.1 *Simulations vs. Experiments*

To compare the refraction model with experimental results, we prepared a BPLC sample using an IPS cell. The blue phase precursor consists of 88.17 wt. % liquid crystal host JC-BP06N (JNC, Japan) with 2.92 wt.% of chiral dopant R5011 (HCCH), 5.24 wt.% di-functional reactive monomer RM257 (Merck), 3.46 wt.% TMPTA (1,1,1-Trimethylolpropane Triacrylate, Sigma Aldrich) and 0.21 wt.% photo-initiator. JC-BP06N is a high- $\Delta\epsilon$ nematic LC host [69] whose

physical properties are listed as follows: $\Delta n = 0.156$ at $\lambda = 633$ nm, $\Delta\epsilon = 473.1$ at 100 Hz and 23 C, and clearing temperature $T_c = 73.8^\circ\text{C}$. Then we filled the precursor into an IPS-5/5 (electrode width $W = 5\mu\text{m}$, electrode gap $G = 5\mu\text{m}$) cell in its isotropic phase. The IPS cell was comprised of interdigitated pixel electrodes on the bottom substrate, but without polyimide alignment layer. The cell gap was $7.5\mu\text{m}$. Next, the cell was placed on a Linkam heating/freezing stage controlled by a temperature programmer (Linkam TMS94). The cell was cooled to the temperature near the transition temperature from chiral nematic phase to blue phase and then cured at BP-I phase with a UV light ($\lambda \sim 365$ nm and intensity ~ 2 mW/cm²) for 30 min.

After UV curing, nanostructured BPLC composites were self-assembled. The measured Bragg reflection wavelength was $\lambda_{\text{Bragg}} \sim 380$ nm. Afterwards, the IPS cell was sandwiched between two crossed polarizers for measurement. The transmitted light was focused with a lens so that different diffraction orders [75] can be collected by the detector. We measured the voltage-dependent transmittance (VT) curve of the sample with this lens and normalized the transmittance to that of two open polarizers.

Figure 2.4 compares the simulated VT curves using Ge's and refraction models with the experimental data. The black solid line stands for the measured VT curve. The red dashed lines represent the simulated VT curve using Ge's model. The general trend is similar, but the simulated peak transmittance from Ge's model is $\sim 10\%$ lower than the measured data. However, when we take the refraction effect into account the simulated VT curve (green solid line) well overlaps with the experimental data. Here, the parameters used in the refraction model are $\Delta n_s = 0.09$ and $E_s = 2.2$ V/ μm . Hence, our refraction model is able to describe the VT characteristics of IPS BPLC more accurately than Ge's model.

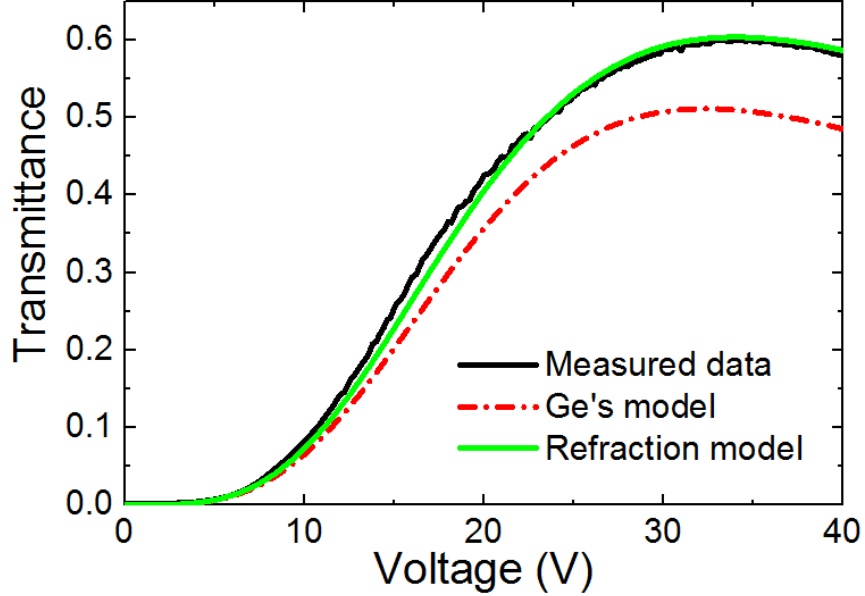


Figure 2.4. Comparison between experimental VT curve and simulated results using Ge's model and the refraction model. BPLC cell: JC-BP06 in IPS-5/5 at 23°C and $\lambda = 633$ nm.

It was reported by Chen, *et al.*[71] that the transmittance profiles of IPS-5/5 and -10/10 at their full-bright state are different under the polarizing optical microscope: the IPS-5/5 sample shows an increased aperture ratio of $\sim 75\%$ while IPS-10/10 keeps at the expected $\sim 50\%$. From Ge's model, both IPS-5/5 and IPS-10/10 cells exhibit $\sim 50\%$ aperture ratios, as shown in [Figures 2.5\(a\)](#) and [2.5\(b\)](#), because only the induced birefringence from electrode gaps contribute to the overall transmittance. In contrast, our refraction model well explains the difference in aperture ratio. [Figures 2.5\(c\)](#) and [2.5\(d\)](#) depict the position dependent transmittance profiles of these two cells at their full-bright state, respectively. Due to the refraction effect, some rays penetrate into the electrode region, especially at the edges of the electrodes. This is why the electrode edges look brighter than electrode gaps in experiments [71]. The lower aperture ratio of IPS-10/10 can be explained as follows: the light at electrode edges (where the electric fields are mostly inclined) cannot be refracted towards the center of the electrode as much as the IPS-5/5 cell because of its

larger electrode dimension and same cell gap ($d = 7.5 \mu\text{m}$). A more detailed explanation of this phenomenon will be outlined later.

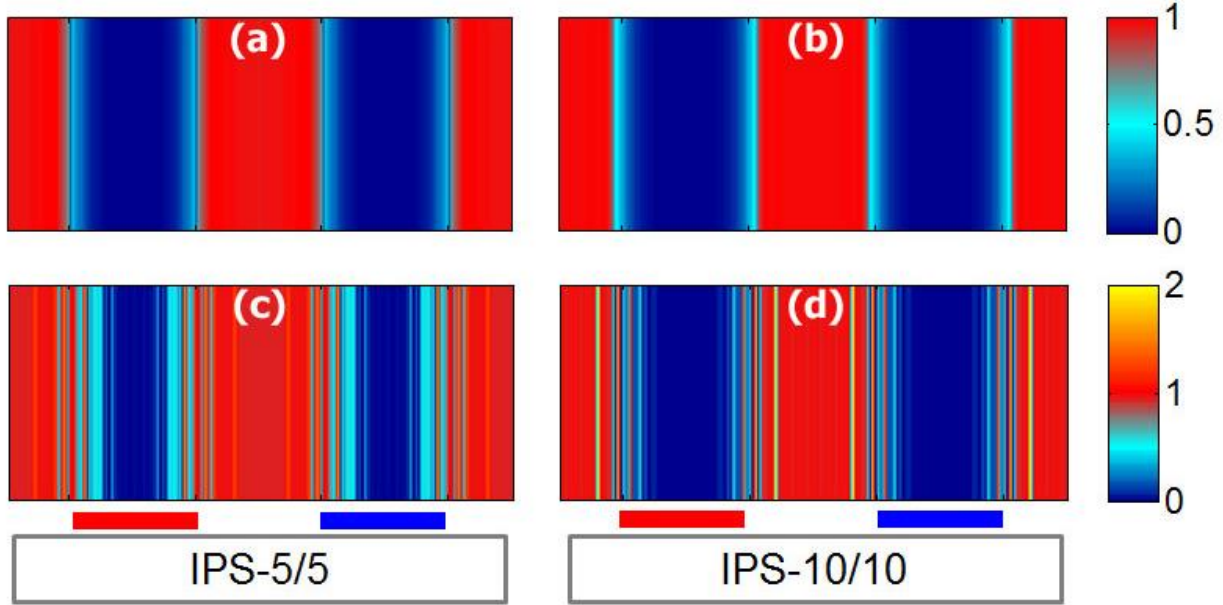


Figure 2.5. Simulated transmittance profiles of JC-BP01 in (a, c) IPS-5/5 and (b, d) IPS-10/10 at $\lambda=633 \text{ nm}$ and 23°C . Cell gap $d=7.5 \mu\text{m}$. (a, b): Ge's model, and (c, d): refraction model.

In brief, our refraction model well agrees with the experimental results. Hence, this model can be used to predict the electro-optic properties of IPS BPLC accurately.

2.3.2 Electrode Dimension Effect

The electrode dimension plays an important role in the electro-optics of IPS BPLC. [Figure 2.6\(a\)](#) shows the simulated VT curves of IPS BPLC using JC-BP01 [67] with different electrode dimensions ($G/W = 1$) using our refraction model. The fitting parameters for JC-BP01 at $\lambda = 550 \text{ nm}$ are $\Delta n_s = 0.154$ and $E_s = 4.05 \text{ V}/\mu\text{m}$. Their on-state voltage (V_{on}) and corresponding peak transmittance are listed in [Table 2.1](#). For comparison, we also included the peak transmittance calculated by Ge's model in the table.

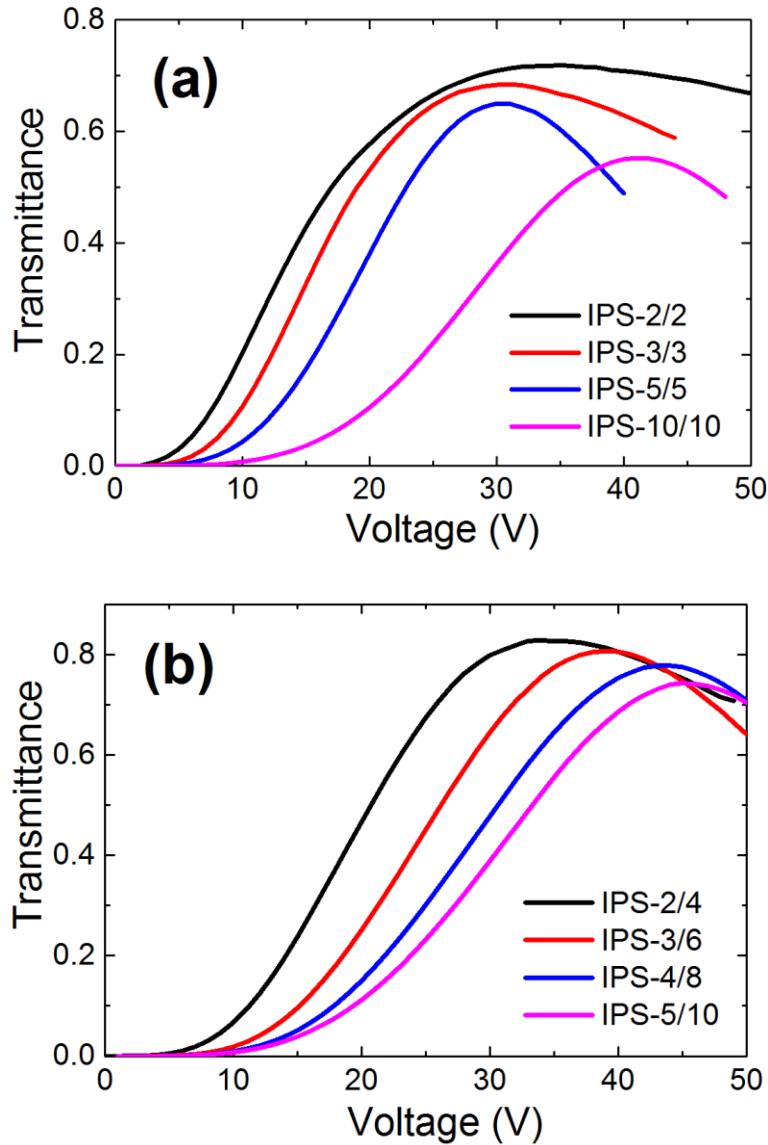


Figure 2.6. Simulated VT curves of IPS cells with (a) $G/W = 1$ and (b) $G/W = 2$ using JC-BP01 at 23°C and $\lambda = 550 \text{ nm}$.

As shown in [Figure 2.6\(a\)](#), the on-state voltage decreases as electrode dimension decreases from IPS-10/10 to -5/5 and then -3/3. However, for IPS-2/2 this trend is reversed. To explain this, we need to consider two determining factors for V_{on} : penetration depth of electric field and induced birefringence Δn . A smaller electrode dimension requires a lower voltage to achieve comparable induced birefringence, that's why IPS-3/3 shows a lower V_{on} than IPS-5/5 and -10/10 as mentioned

above. On the other hand, a smaller electrode dimension also leads to a shallower penetration depth [56], which in turn demands a higher induced birefringence in order to accumulate sufficient phase retardation for achieving high transmittance. These two factors compete with each other and result in a higher V_{on} for IPS-2/2 due to the deficiency of shallow penetration depth outweighs the merit of strong electric field. However, for IPS-3/3 and 5/5, although their electric field intensities are weaker than that of IPS-2/2, their deeper penetration helps to lower V_{on} .

Table 2.1. Comparison between refraction and Ge's models for IPS BPLC cells with $G/W = 1$.

BPLC: JC-BP01 at 23°C and $\lambda = 550$ nm.

Electrode Dimension	Refraction Model		Ge's Model
	V_{on} (V)	T_{max}	T_{max}
IPS-2/2	34.2	71.4%	50.4%
IPS-3/3	31.8	68.5%	50.2%
IPS-5/5	32.4	65.0%	50.7%
IPS-10/10	41.2	54.9%	50.6%

Another clear trend shown in [Figure 2.6\(a\)](#) is that the peak transmittance drops as the electrode dimension increases. IPS BPLCs with different electrode dimensions have different on-state voltages and electric field intensities. According to the extended Kerr model, higher electric field intensity would result in a higher induced Δn . As a result, the difference in refractive indices between neighboring layers would be larger as explained above and the light would bend more by the refraction effect. Especially on the top of electrodes, the larger angle with respect to the optical axis and higher Δn would result in a higher transmittance and reduced dead zones. This is why IPS-5/5 exhibits a larger aperture ratio than IPS-10/10 in experiments.

Next, we use the refraction model to simulate the VT curves of IPS BPLC (JC-BP01) with $G/W = 2$, as depicted in [Figure 2.6\(b\)](#). [Table 2.2](#) lists the on-state voltage and peak transmittance

with and without the refraction effect. The $G/W=2$ cells show following same trend with $G/W=1$ cells: as the electrode dimension increases the peak transmittance decreases. Although a larger G leads to a deeper penetration depth, the electric field is weaker so that the induced birefringence is lower. Moreover, a wide electrode width W leads to a larger dead-zone area, which in turn lowers the transmittance. From [Table 2.1](#) and [Table 2.2](#), we find that the cells with $G/W=2$ exhibits weaker refraction effect than the $G/W=1$ cells. This originates from that the IPS cells with a larger G/W ratio generates a flatter electric field profile so that the incident light is less bent by the refraction effect. As a result, in comparison with Ge's model, the increase in peak transmittance due to refraction effect is smaller. We also simulated the VT curves for IPS BPLC with $G/W=3$ and 4 ratios. The results are also included in [Table 2.2](#), and they show the same trend as well.

Table 2.2. Comparison between refraction model and Ge's model for IPS BPLC with $G/W=2, 3$ and 4 structures. BPLC: JC-BP01 at 23°C and $\lambda = 550 \text{ nm}$.

Electrode Dimension	Refraction Model		Ge's Model
	V_{on} (V)	T_{max}	T_{max}
IPS-2/4	34.2	82.8%	64.1%
IPS-3/6	38.4	80.7%	63.7%
IPS-4/8	42.8	77.8%	64.1%
IPS-5/10	44.6	74.3%	64.3%
IPS-2/6	41.8	84.6%	73.3%
IPS-3/9	44.2	83.6%	73.7%
IPS-2/8	48.2	86.6%	78.5%
IPS-3/12	49.6	83.2%	78.3%

2.3.3 Cell Gap Effect

In a nematic IPS cell, both transmittance and response time are affected by the cell gap.

However, the transmittance of IPS cells is insensitive to the cell gap as long as the cell gap exceeds the penetration depth of electric field [56]. This feature is particularly desirable for fabricating large-size LCD panels, in which uniform cell gap control is a big concern. Here we revisit this important feature by including the refraction effect.

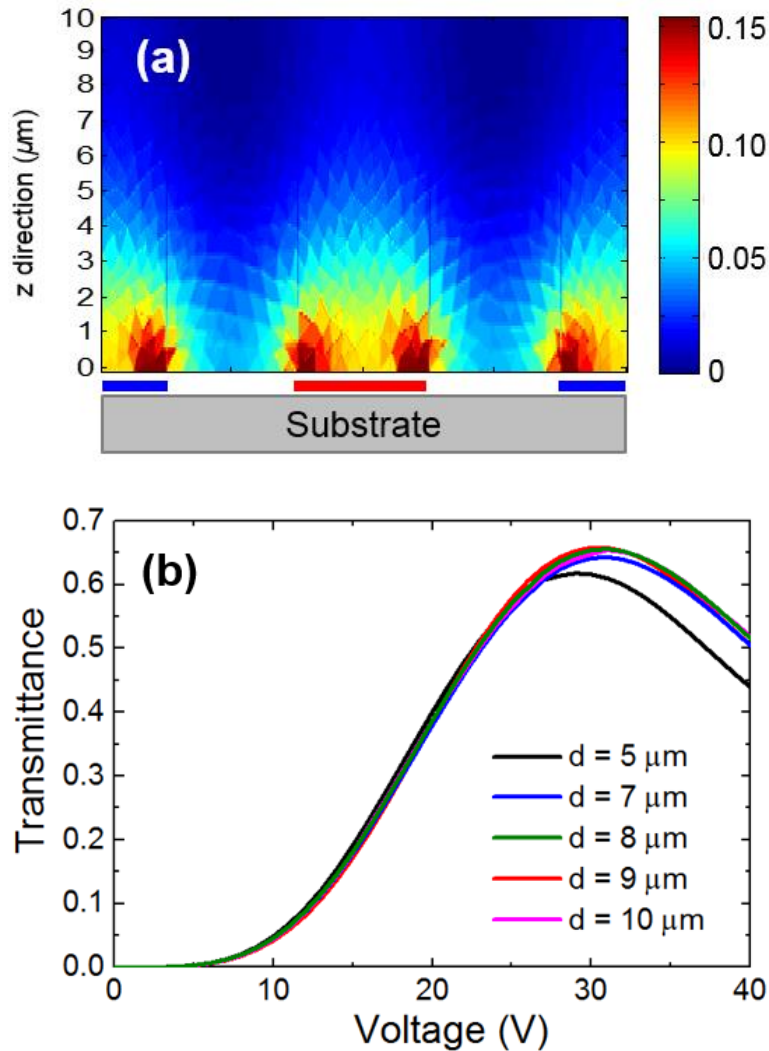


Figure 2.7. (a) Induced Δn profile of a 10- μm -thick IPS-5/5 cell at 31V and (b) simulated VT curves of IPS-5/5 with different cell gaps. BPLC: JC-BP01 at 23°C and $\lambda = 550 \text{ nm}$.

Figure 2.7(a) depicts the induced birefringence distribution of a 10- μm IPS-5/5 cell and Figure 2.7(b) shows the VT curves of the IPS-5/5 cell with different cell gaps simulated by the

refraction model. The material employed here is JC-BP01 [67]. From [Figure 2.7\(a\)](#), the induced birefringence is the highest near the electrode surface and it gradually drops as the distance increases. As shown in the figure, when the depth increases to $5.5 \mu\text{m}$ the induced birefringence drops to < 0.05 . Hence, for IPS BPLC the VT curve is insensitive to cell gap as long as the cell gap is larger than the field's penetration depth, which is governed by the electrode dimension through Poisson equation. This is verified in [Figure 2.7\(b\)](#). As the cell gap drops from $10 \mu\text{m}$ to $9 \mu\text{m}$ and then $8 \mu\text{m}$, the VT curves remains almost unchanged. When the cell gap continues to decrease to $7 \mu\text{m}$, the transmittance drops slightly due to the cell gap becomes thinner than the penetration depth. As the cell gap continues to decrease to $5 \mu\text{m}$, the transmittance becomes much lower. Thus, in order to assure that the VT characteristics is insensitive to the cell gap variation, the cell gap must be kept thicker than the field's penetration depth.

Shown in [Figures 2.8\(a\)-\(d\)](#) are the on-state spatial transmittance profiles of IPS-5/5 with cell gap $d=5, 7, 8,$ and $10 \mu\text{m}$, respectively. As the cell gap increases, the light would be bent more toward the center of electrodes by the refraction effect owing to a longer optical path. This explains why the IPS-5/5 with $d = 10 \mu\text{m}$ shows a slightly larger aperture ratio than the corresponding $7\text{-}\mu\text{m}$ cell. Notwithstanding, the electric fields beyond the penetration regions are very weak and the BPLC in that region can be nearly regarded as isotropic. Therefore, the light wouldn't accumulate additional phase retardation and transmittance wouldn't change in spite of the fact that light rays experience longer optical path. As a result, the VT curves are not critically dependent on the cell gap as long as the cell gap exceeds the penetration depth of electric field. In addition, the cell gap effect can be used to explain the aforementioned lower aperture ratio of IPS-10/10 because its larger electrode dimension.

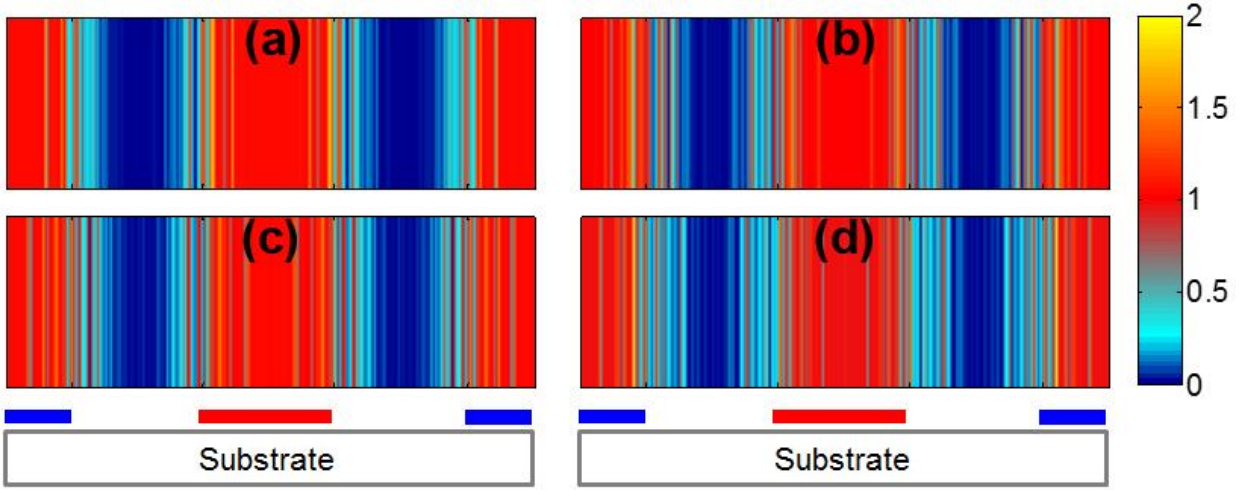


Figure 2.8. Transmittance profile of IPS-5/5 with different cell gaps: (a) 5 μm , (b) 7 μm , (c) 8 μm and (d) 10 μm . BPLC: JC-BP01 at 23°C and $\lambda = 550 \text{ nm}$.

2.3.4 Saturated Birefringence and Saturation Field Effects

A higher saturated birefringence Δn_s not only helps boost the Kerr constant [76] but also affects the electro-optical characteristics directly due to the refraction effect. Based on JC-BP01, [Figure 2.9\(a\)](#) shows the simulated VT curves of IPS-2/4 with different Δn_s while keeping E_s of JC-BP01 unchanged ($E_s = 4.05 \text{ V}/\mu\text{m}$). The red solid line represents the IPS BPLC employing JC-BP01. As Δn_s increases, the peak transmittance increases while on-state voltage decreases. For a BPLC with higher Δn_s , according to [Equation \(2.2\)](#), the refractive index difference between neighboring layers would increase and the light would bend more significantly by the refraction effect. Thus, the light would propagate at a larger angle with respect to the optical axis. Moreover, a higher Δn_s directly leads to an enhanced phase retardation. These two factors concurrently contribute to a higher transmittance and reduced dead zone area.

[Figure 2.9\(b\)](#) shows how E_s affects the VT curves of IPS-2/4 based on JC-BP01. It's clearly shown that as E_s increases the on-state voltage also increases while peak transmittance remains

unchanged. This indicates that E_s only determines the voltage where the BPLC reaches its Δn_s , but the maximum induced birefringence still remains unchanged at the on-state voltage.

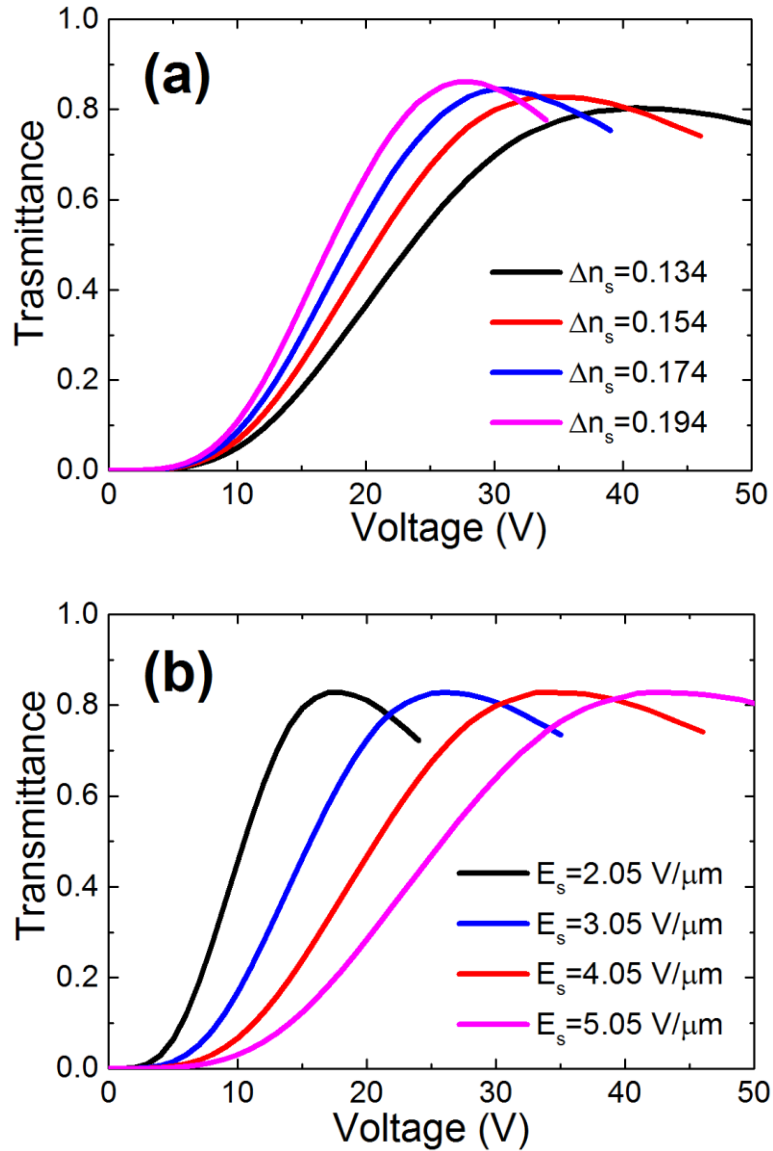


Figure 2.9. Simulated VT curves of IPS-2/4 using BPLCs with (a) different Δn_s ($E_s = 4.05 \text{ V}/\mu\text{m}$), and (b) different E_s ($\Delta n_s = 0.154$) at 23°C and $\lambda = 550 \text{ nm}$. Red solid lines: JC-BP01.

Hence, in IPS BPLC cells, a higher Δn_s helps reduce the operation voltage and enhance the transmittance, not only by increasing the Kerr constant on material side but also by enhancing the

refraction effect. A lower E_s is effective in lowering operation voltage while maintaining the same peak transmittance. In order to achieve low voltage while keeping high transmittance, an effective strategy is to boost Δn_s while keeping E_s low.

2.4 Summary

In this chapter, we have developed a numerical model to compute the electro-optical characteristics of IPS BPLC cells while taking the refraction effect into account. The refraction model well agrees with the experimental results, and is more accurate than conventional model in predicting the electro-optics of IPS BPLC. With this numerical calculation model, parameters affecting the electro-optics of BPLCDs in IPS structures, such as electrode dimension effect, cell gap effect, saturated induced birefringence as well as saturation electric field effects have been investigated. The study of the device physics provides important guidelines for future device development and optimizations.

CHAPTER 3. LOW VOLTAGE BLUE PHASE LIQUID CRYSTAL DISPLAYS

In a conventional planar IPS electrode configuration, the electric field is confined near the bottom substrate, and only the blue phase liquid crystals in this shallow region contribute to the induced birefringence. As a result, the driving voltage is high and optical transmittance is low. In order to lower the operation voltage, various device configurations have been proposed to generate strong electric fields with enhanced penetration depth [63, 65]. However, their fabrication processes are rather challenging. In this chapter, we will discuss possible approaches to achieve low voltage blue phase LCDs from device design and material development viewpoints.

3.1 Device Configurations

3.1.1 *Protrusion Electrodes*

From Chapter Two, we can enhance the transmittance by increasing the G/W ratio of the IPS cell. However, the major tradeoff is higher driving voltage due to the wider electrode gap. An effective way to overcome this issue is to implement protrusion electrodes [60, 77]. The typical device structure using protrusion electrode structure is shown in [Figure 3.1](#). The BPLC cell is sandwiched between two crossed polarizers, and organic protrusions are formed on the bottom substrate. Then, the pixel and common protrusion electrodes are deposited onto the organic protrusions. Their dimension is defined as follows: W is the bottom width of organic protrusions, H is the height, and G is the space between adjacent protrusions. In this design, strong electric fields are generated between the pixel and common electrodes, and more importantly, the field is able to penetrate deeply into the LC bulk region. These two factors concurrently lead to a lower operation voltage. The detailed performance depends on the protrusion height and the G/W ratio.

To investigate the influence of refraction effect on the transmittance of protrusion IPS cell, we used rectangular protrusion electrodes in our simulations. Nonetheless, the electrodes can be fabricated in other shapes, such as elliptical, trapezoid, etc. [78]

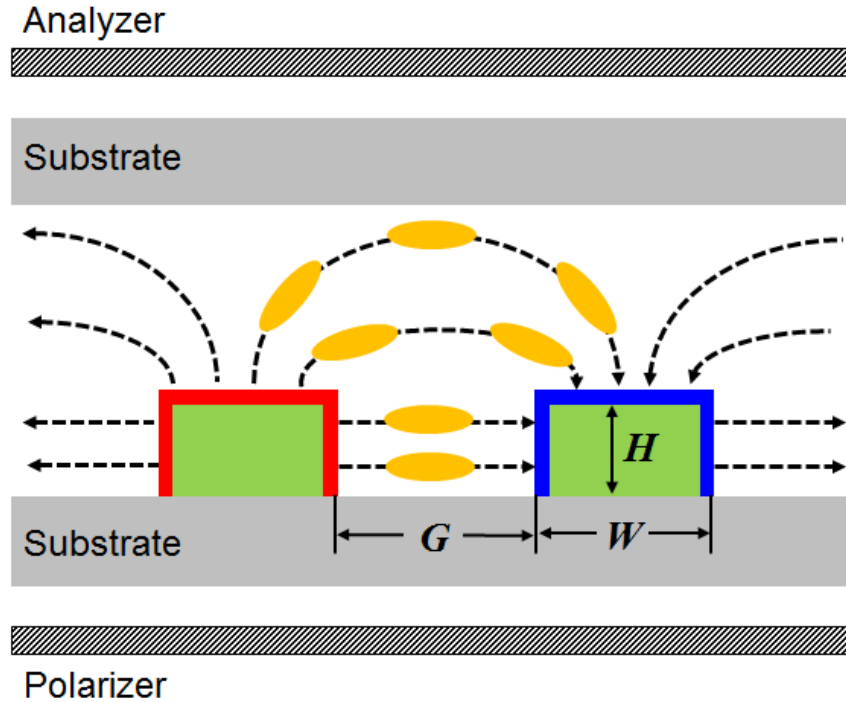


Figure 3.1. Cell structure of an IPS BPLC cell using protrusion electrodes.

Shown in Figures 3.2(a) and (b) are the simulated VT curves of planar and protrusion IPS cells with protrusion height $H = 1\mu\text{m}$ and $2\mu\text{m}$ for IPS-2/4 employing two different BPLC materials: JC-BP01 ($\Delta n_s = 0.154$, $E_s = 4.05\text{V}/\mu\text{m}$) and JC-BP06 ($\Delta n_s = 0.09$, $E_s = 2.2\text{V}/\mu\text{m}$). Compared to a planar IPS, the protrusion IPS exhibits nearly the same transmittance since the protrusion electrodes mainly generate electric fields in the electrode gaps and don't change the field distribution above the electrodes. Nonetheless, the operation voltage drops dramatically as the protrusion height increases due to the penetration depth of electric field is significantly enhanced by the protrusion electrodes.

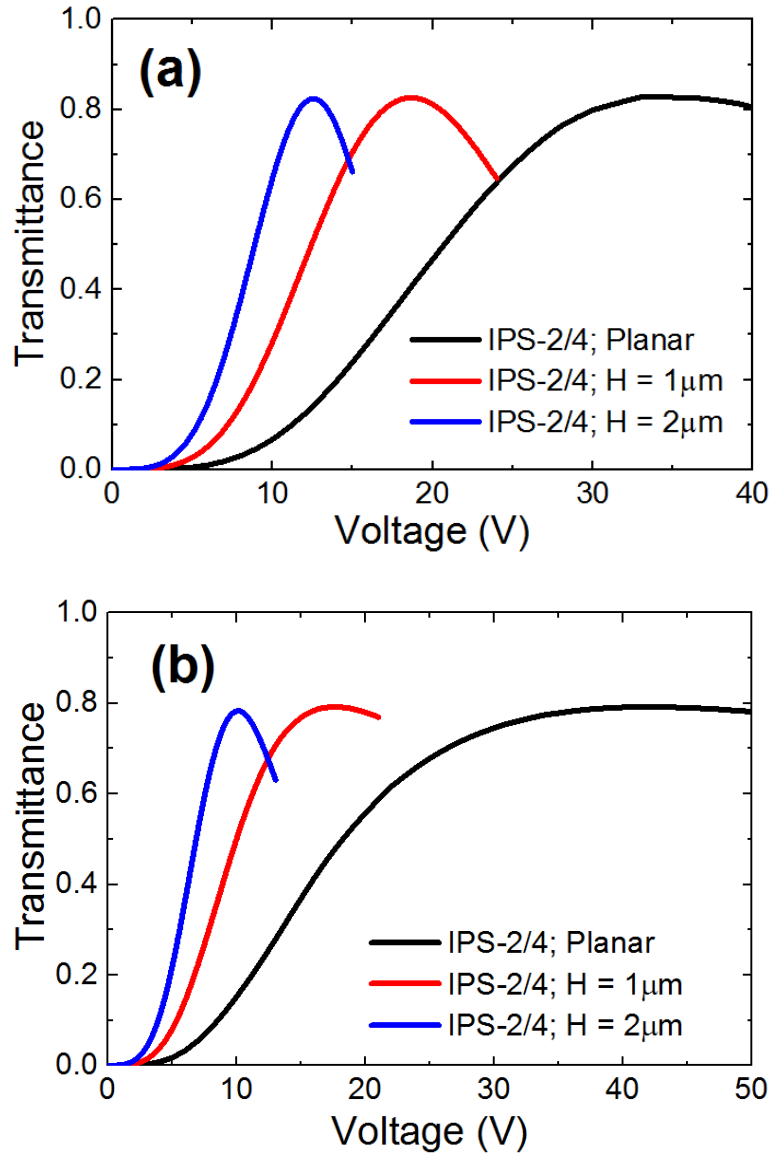


Figure 3.2. Simulated VT curves IPS-2/4 with protrusion electrodes employing (b) JC-BP01 and (c) JC-BP06 ($T = 23^{\circ}\text{C}$ and $\lambda = 550 \text{ nm}$).

On the other hand, JC-BP06 exhibits a higher voltage than JC-BP01 for planar IPS-2/4 structure (40 V vs. 34 V). This is because JC-BP06 has a relatively lower saturated birefringence ($\Delta n_s = 0.09$) and IPS-2/4 has a relatively shallow penetration depth. Thus, JC-BP06 requires a higher operation voltage to reach the peak transmittance. However, when we use protrusion electrodes, the relatively low Δn_s of JC-BP06 can be compensated by the enhanced penetration

depth of electric field. Thus, with the same device structure JC-BP06 exhibits a lower operation voltage than JC-BP01 because JC-BP06 has a higher Kerr constant. As [Figure 3.2\(b\)](#) shows, for IPS-2/4 with $h = 2 \mu\text{m}$ its operation voltage is reduced to 10V while keeping $> 80\%$ transmittance. Such a protrusion height is easy to obtain in fabrications, as recent progresses on fabrication has already achieved a protrusion height of $3.5 \mu\text{m}$ [77]. Lowering the operation voltage to $< 10\text{V}$ is an important milestone to enable BPLC to be addressed by a-Si TFT technology. To further boost transmittance, we can increase the birefringence of the BPLC material. For example, as [Figure 3.2\(a\)](#) shows, JC-BP01 has a higher induced birefringence so that its peak transmittance can reach 83%, slightly higher than that of JC-BP06.

3.1.2 Etched Electrodes

In addition to protrusion electrodes, etching is another effective approach to lower the operation voltage [64, 66]. [Figure 3.3](#) shows the device structure of a BPLC cell using etched electrodes. In an etched-IPS structure, say IPS-2/4, the etching takes place along the $4\text{-}\mu\text{m}$ electrode gaps with an etching depth of H' . As a result, the fringe field is able to penetrate above and below the $2\text{-}\mu\text{m}$ ITO electrodes, as shown in [Figure 3.3](#). The BPLC molecules filled in the etched part of the substrate also contribute to phase retardation so that the driving voltage would be reduced. Similar to protrusion IPS, etched-IPS using JC-BP06 also shows lower operation voltage than that using JC-BP01 since the bottom fringe fields provide an extra phase retardation to compensate the relatively low Δn_s of JC-BP06. Hence, in simulations we focus on JC-BP06 to demonstrate the effectiveness of the etched-electrode approach.

[Figure 3.4\(a\)](#) compares the simulated VT curves of IPS-2/4 structure with etching depth H' increasing from 0, 1, 2 to $4 \mu\text{m}$. As the etching depth increases, the operation voltage drops rapidly

and then gradually saturates. With $H' = 2\mu\text{m}$, the operation voltage is reduced to $\sim 10\text{V}$. This saturation phenomenon originates from the finite penetration depth of electric field below in the etched regions. Hence, when the etching depth is larger than the penetration depth, the operation voltage does not decrease further. This feature provides a high fabrication tolerance for the etched-IPS since we don't need to control the etching depth very precisely as long as it's deeper than the penetration depth.

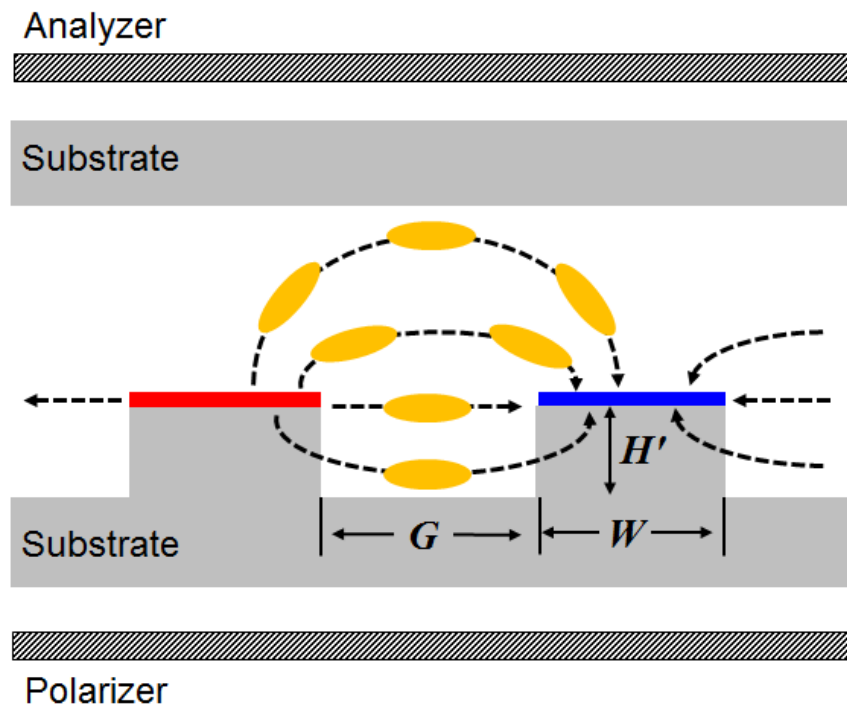


Figure 3.3. Cell structure of an IPS BPLC cell using etched electrodes.

To improve transmittance, we can increase the G/W ratio, such as IPS-2/6 or -2/8, while still using the etched electrodes. Same with etched IPS-2/4, both etched IPS-2/6 and -2/8 show the saturation effect, but at a deeper etching depth ($\sim 4\mu\text{m}$ for IPS-2/6 and $\sim 6\mu\text{m}$ for IPS-2/8), due to the larger penetration depths of electric fields. Figure 3.4(b) includes the simulated VT curves of etched IPS-2/6 and IPS-2/8 cells with 4- μm and 6- μm etching depths, respectively. Compared to IPS-2/4, their transmittance can exceed 80% due to higher G/W ratios; however, a tradeoff is

increased voltage. As nanotechnology advances, smaller electrode dimension could be fabricated [79]. If we can reduce the electrode width to $1\ \mu\text{m}$, then the operation voltage can be reduced to $\sim 8\text{V}$ while maintaining a high transmittance of $>80\%$, as Figure 3.4(b) depicts.

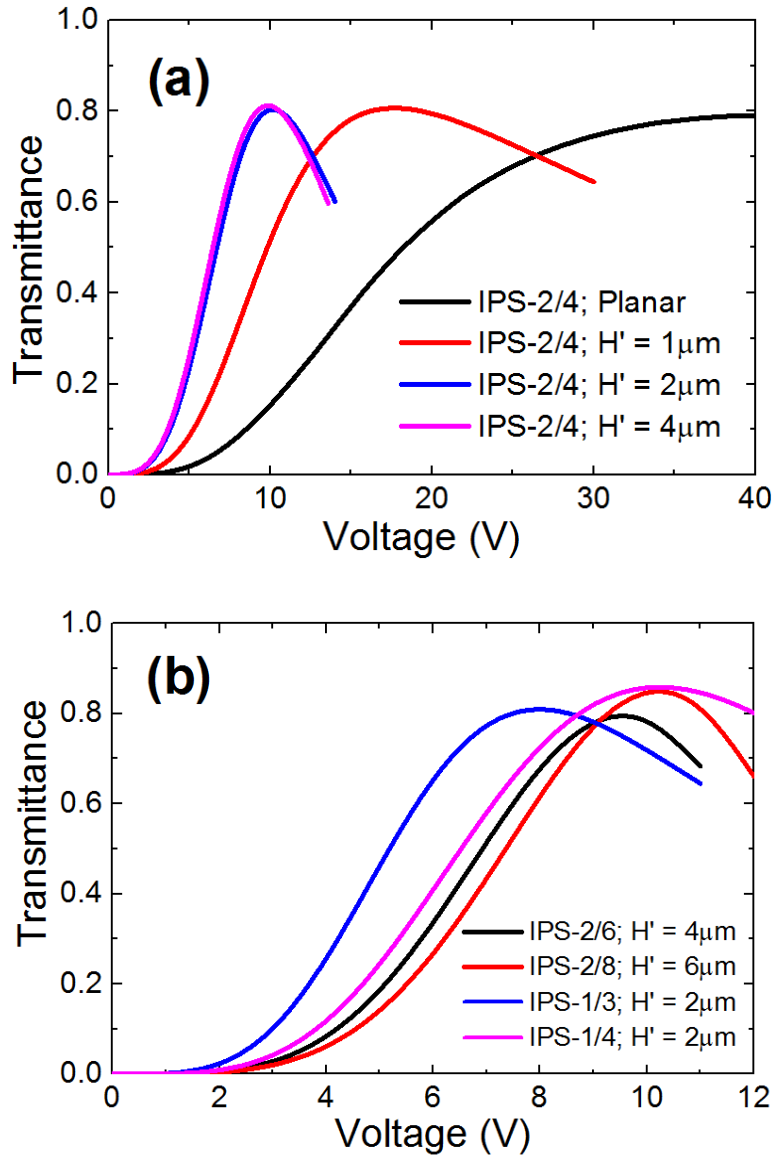


Figure 3.4. Simulated VT curves of etched-IPS cells with different electrode dimensions: (b)

$G/W = 2$ and (c) $G/W = 3, 4$ and 5 using JC-BP06 ($T = 23^\circ\text{C}$ and $\lambda = 550\ \text{nm}$).

3.1.3 Blue Phase LCD with Single Gamma Curve

In an IPS BPLC cell, the phase retardation depends on the wavelength and induced birefringence. The latter one in turn depends on the Kerr constant, which decreases as the wavelength increases [80]. Accordingly, the VT curves of an IPS BPLC depend on the wavelength, as shown in [Figure 3.5\(a\)](#). Three gamma curves are required to drive the red (R: $\lambda = 650$ nm), green (G: $\lambda = 550$ nm) and blue (B: $\lambda = 450$ nm) sub-pixels, which in turn increases the complexity of driving electronics.

To simplify the driving circuits, we propose following method to achieve single gamma curve for IPS BPLC. Based on the discussions above, we know that the on-state voltage of an IPS BPLC can be adjusted by changing the G/W ratio. Accordingly, in order to achieve overlapped gamma curves for RGB colors, we can simply adjust the electrode gap G for RGB sub-pixels while maintaining the same electrode width and etching depth. Similar approach of adjusting the electrode gap has been used to balance the optical phase retardation between transmissive and reflective regions for transfective displays [81].

Here, we use IPS-2/4 with $H' = 2.5\mu\text{m}$ and $d = 7.5\mu\text{m}$ for the green wavelength as a benchmark to illustrate the design principles. From [Figure 3.5\(a\)](#), we need to lower the on-state voltage for the red color. Thus, we choose a narrow electrode gap, say $G = 3.6\mu\text{m}$, while still keeping $H' = 2.5\mu\text{m}$ and $d = 7.5\mu\text{m}$. On the other hand, we increase G to $5.2\mu\text{m}$ for the blue wavelength. [Figure 3.5\(b\)](#) shows the normalized VT curves for RGB sub-pixels with different electrode gaps. Indeed, the RGB gamma curves overlap fairly well, and consequently, the complexity of driving circuit can be greatly reduced.

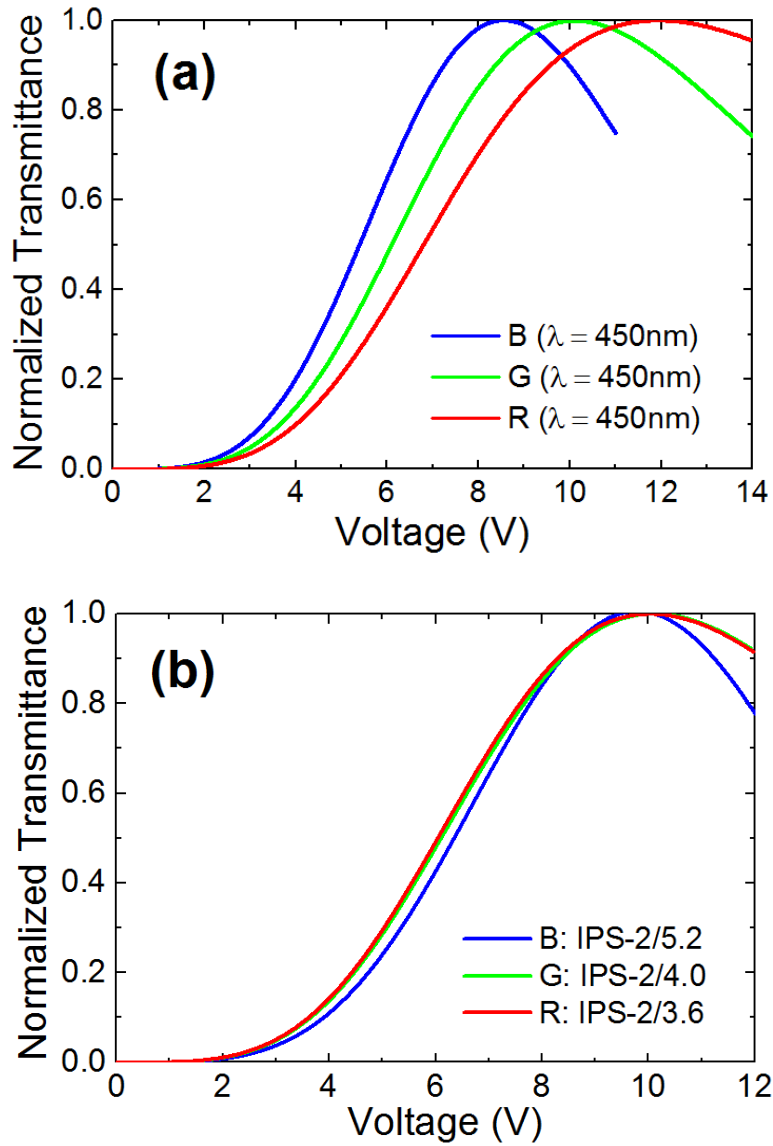


Figure 3.5. (a) Calculated VT curves for RGB wavelengths of etched IPS-2/4 cell. (b) Calculated VT curves for IPS-2/3.6 (R), -2/4 (G), -2/5.2 (B). ($H = 2.5\mu\text{m}$ and $d = 7.5\mu\text{m}$, BPLC: JC-BP06).

3.2 Material Development

In addition to device designs, continuous development of large Kerr constant materials [68, 70] would help further reduce the operation voltage. From Gerber's model, Kerr constant is related

to the properties of LC host through following equation [82]:

$$K \sim \Delta n \cdot \Delta \varepsilon \cdot \frac{\varepsilon_0 \cdot P^2}{k\lambda \cdot (2\pi)^2}; \quad (3.1)$$

where Δn and $\Delta \varepsilon$ are the birefringence and dielectric anisotropy of the LC host, respectively; P is the pitch length, and k is the average elastic constant. Hence, in order to enhance the Kerr constant, a straightforward approach is to enhance the $\Delta \varepsilon$ or Δn of the LC host.

In addition, the aforementioned comparison between JC-BP01 and JC-BP06 using different device structures implies the operation voltage is also determined by the electrode dimension. JC-BP01 has a higher Δn_s than JC-BP06, but its $\Delta \varepsilon$ is lower (~ 94), resulting in a lower Kerr constant. In contrast, although JC-BP06 has a high Kerr constant because of its huge $\Delta \varepsilon$ (~ 473), its Δn_s is too low (0.09). Hence, when JC-BP06 is employed in small-dimension electrode structures like IPS-2/2 and IPS-2/4, the operation voltage is usually very high. In order to reduce the operation voltage, device structures as well as material properties must be considered together. For small electrode dimension structures, high birefringence is preferred due to its shallow electric field penetration depth. For large electrode dimension structures, high dielectric anisotropy is preferred because of its weaker electric field.

Since there is limited room for further enhancing Δn , extensive efforts have been devoted to enhance the $\Delta \varepsilon$ significantly ($\Delta \varepsilon \sim 300$) [68, 69, 83], but the downsides of using such high- $\Delta \varepsilon$ LC hosts are apparent. On one hand, these compounds have long molecular conjugation and large dipole moment so that their viscosity is very high. This slows down the device fabrication process and increases device response time. On the other hand, the huge $\Delta \varepsilon$ produces a large capacitance (C_{LC}), leading to insufficient charging capability in conventional pixel circuit, i.e. the voltage applied to the LC capacitor cannot reach the desired value within the designated charging time. As

a result, the optical efficiency is sacrificed. In particular, when the driving frequency is tripled in color sequential displays, the charging issue becomes more severe. Meanwhile, the Debye relaxation frequency of such bulky liquid crystal molecule is rather low. The frequency dependency of parallel dielectric constant $\varepsilon_{//}'$ is governed by the Debye model [84]:

$$\varepsilon_{//}' = \varepsilon_{\infty} + \frac{\varepsilon_0 - \varepsilon_{\infty}}{1 + (f / f_r)^2}; \quad (3.2)$$

where ε_0 is the static permittivity along the long molecular axis at the low frequency limit, ε_{∞} is the permittivity at the high frequency limit, and f_r is the Debye relaxation frequency, which is related to the molecule properties through following equation [85]:

$$f_r \sim \frac{1}{\gamma \cdot l^3}. \quad (3.3)$$

Here, γ is the rotational viscosity and l is the molecule length of LC host. Compared to conventional nematic LCs, the molecule length of high- $\Delta\varepsilon$ LC host is much longer and the viscosity is much higher. As a result, the relaxation frequency of high- $\Delta\varepsilon$ LC host is much lower. For instance, the relaxation frequency f_r of JC-BP06N is only 1.07 kHz. Such a low relaxation frequency cannot meet the charging requirement of high-resolution displays due to the huge number of pixels. In contrast, the relaxation frequency of conventional nematic LCs are in the magnitude of several MHz. Therefore, the $\Delta\varepsilon$ of LC host shouldn't be too high in order to mitigate the charging issue. For instance, by employing a LC host with $\Delta\varepsilon \sim 80$, the charging issues have been well resolved in blue phase LCD prototypes [77].

3.3 Summary

In this chapter, we have discussed possible approaches from device design and material

development viewpoints to achieve low-voltage blue phase devices. On the device side, by using protrusion and etched electrodes, the operation voltage can be reduced to $< 10\text{V}$ and transmittance is enhanced to $> 80\%$. On the material side, we should not only emphasize on enhancing the Kerr constant, but also need to pay attention to the individual Δn and $\Delta\epsilon$ values according to the device structures employed. High $\Delta\epsilon$ is helpful in reducing the operation voltage, but it would incur charging issues as a tradeoff. In order to mitigate this issue, we should focus on LC host with $\Delta\epsilon \sim 80$ or even lower. These efforts will provide guidelines for future blue phase device optimizations and material characterizations.

CHAPTER 4. HIGH TRANSMITTANCE BLUE PHASE LIQUID CRYSTAL DISPLAYS

Compared to the planar IPS structures, the protrusion and etched electrode structures in Chapter Three can reduce operation voltage significantly. However, the transmittance is still rather low compared to nematic LCDs. In order to reduce power consumption, most commercial LCDs, including twisted nematic [7, 9], vertical alignment [11], and fringe field switching [12, 13] modes, exhibit ~90% or higher transmittance. Thus, in order to compete with mainstream nematic LCDs, there is an urgent need to develop a blue phase LCD with comparable or even higher transmittance. In this chapter, we will introduce a blue phase LCD using Z-shaped electrode to achieve high transmittance and low operation voltage simultaneously.

4.1 Device Structure

The cross-sectional view of the Z-shaped electrode configuration is shown in [Figure 4.1](#). The LC layer is interposed between two glass substrates. A thin layer of passivation material (e.g. SiO₂, SiN_x, etc.) with a height of H is first formed on the substrate. The bottom width of the passivation protrusion is defined as L and the space between adjacent passivation protrusions is defined as G . The taper angle of passivation protrusions is denoted as θ . Then, the indium tin oxide (ITO) electrodes are coated near the edge of passivation protrusions to form pixel and common electrodes. The common and pixel electrodes cover the top surface passivation protrusions with a length of W_1 and bottom substrate with a length of W_2 . W_1 and W_2 may have the same or different widths, as will be outlined later. In each RGB sub-pixel, multiple electrodes can be formed. The BPLC layer is further sandwiched between crossed polarizers, as shown in [Figure 4.2](#). For the

purpose of expanding viewing angle and reducing color shift, retardation films, which can be either a biaxial film or a set of uniaxial films, are laminated between bottom polarizer and the top analyzer [29].

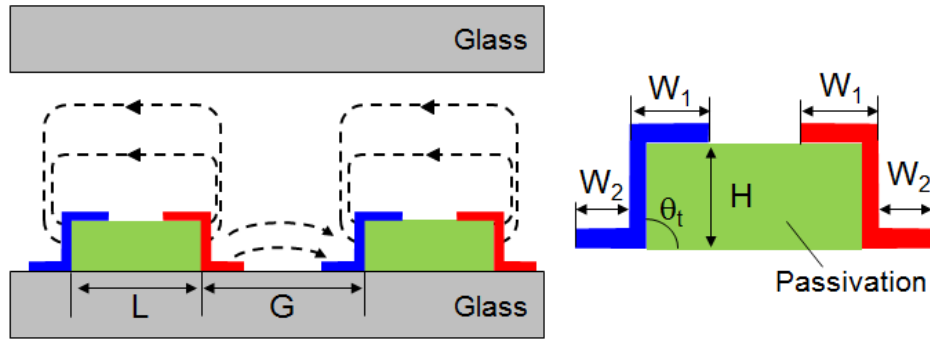


Figure 4.1. Cross-sectional view of a BPLC cell using Z-shaped electrodes.

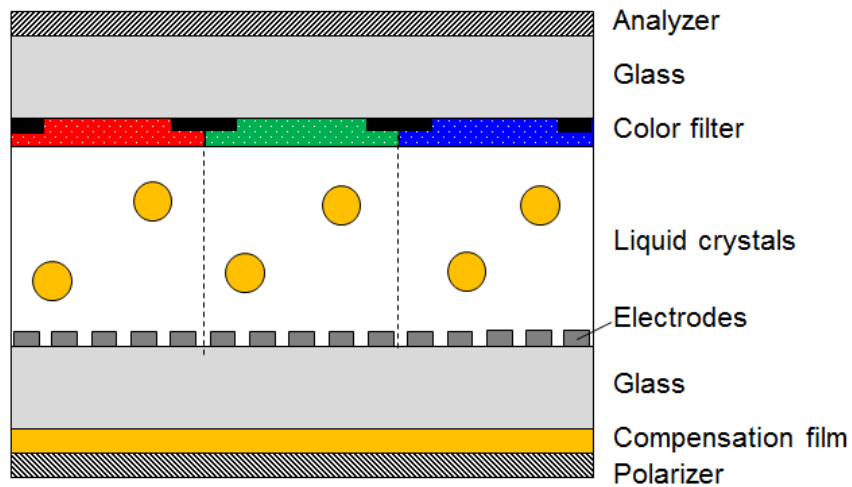


Figure 4.2. Electrode arrangement in a LCD pixel.

4.2 Electro-optical Performance

As discussed in Chapter Three, high- $\Delta\epsilon$ LC hosts such as JC-BP06N ($\Delta\epsilon \sim 473$) are subject to serious charging issues. Therefore, hereinafter we will focus on a LC host with much lower $\Delta\epsilon$, which has already been proven with good performance in resolving the charging issue in blue

phase LCD prototypes [77]. The parameters of the blue phase material are: $\Delta\epsilon \sim 80$ at $f = 100\text{Hz}$, $E_s = 4.8 \text{ V}/\mu\text{m}$ and $\Delta n_s = 0.15$ at $\lambda = 550\text{nm}$.

4.2.1 Voltage-transmittance Characteristics

Due to the optical isotropy of BPLCs at the voltage-off state, the linearly polarized light after the polarizer would be blocked by the analyzer. When the display is turned on, a driving voltage is applied to the pixel electrodes to generate an electric field in the BPLC layer with a main vector along horizontal direction, except the regions near the edge of passivation protrusions, as illustrated in Figure 4.1.

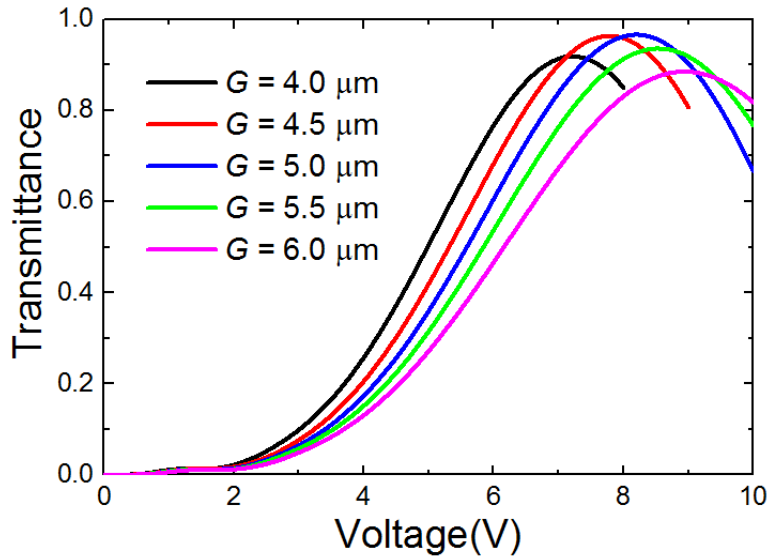


Figure 4.3. Calculated VT curves of BPLC cells using Z-shaped electrodes under different G conditions. ($\theta = 90^\circ$, $H = 3.5\mu\text{m}$; $W_1 = W_2 = 1.0\mu\text{m}$; $L = 4.0\mu\text{m}$, $\lambda = 550\text{nm}$).

Figure 4.3 shows the calculated VT curve using the Z-shaped electrodes. Here, the taper angle of the passivation layer is set at $\theta = 90^\circ$ and the height of the passivation layer is $H = 3.5\mu\text{m}$; the electrode width $W_1 = W_2 = 1.0\mu\text{m}$. The bottom width of the passivation protrusion $L = 4.0\mu\text{m}$, and the gap between adjacent passivation protrusion G varies between $4.0\mu\text{m}$ and $6.0\mu\text{m}$. The

BPLC parameters are as follows: $\Delta n_s = 0.15$ and $E_s = 4.8 \text{ V}/\mu\text{m}$ at $\lambda = 550\text{nm}$. The black solid curve stands for the VT curve using the Z-shaped electrode with $G = 4.0 \mu\text{m}$, where the required driving voltage is only 7.2V, and the peak transmittance is 91.9%. When G increases, the operation voltage increases, while peak transmittance gradually increases and then decreases when G exceeds 5.0 μm . At $G = 5.0 \mu\text{m}$, the driving voltage is 8.2V and the peak transmittance reaches 96.6% (shown as the blue solid curve).

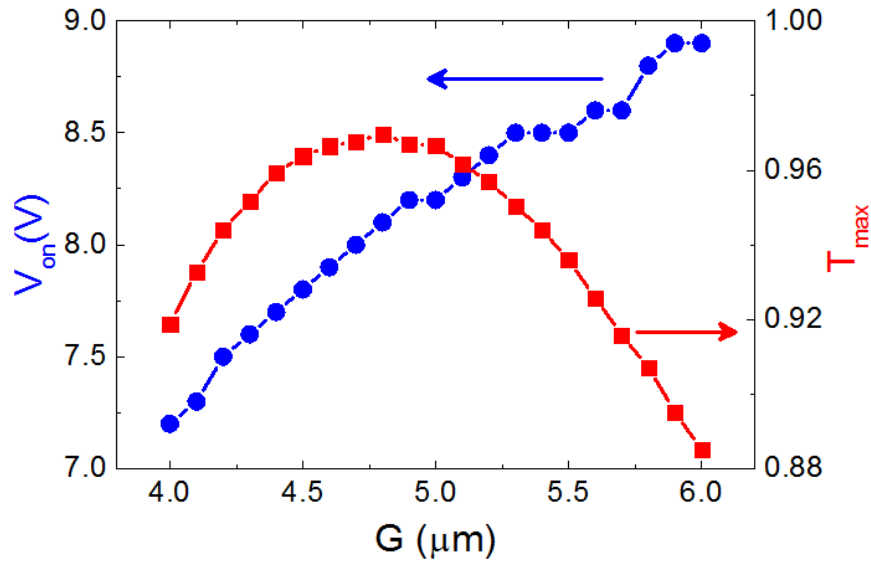


Figure 4.4. A summary of the peak transmittance (T_{\max}) and on-state voltage (V_{on}) of BPLC cells using Z-shaped electrodes under different G conditions ($L = 4.0\mu\text{m}$, $\lambda = 550\text{nm}$).

In order to find out the optimal device dimension to achieve high transmittance, we varied G between 4.0 μm and 6.0 μm with a step of 0.1 μm and simulated their VT curves. Figure 4.4 summarizes the peak transmittance (T_{\max}) and corresponding on-state voltage (V_{on}) under different G conditions. The highest peak transmittance 97.1% occurs at $G = 4.8 \mu\text{m}$, which is equivalent to $G/L = 1.2$. A more detailed discussion of this optimal G/L ratio to achieve high transmittance will be explained later. Figure 4.5 schematically plots the transmittance profile at the on-state voltage

(upper) and the electric potential distribution (lower) for the scenario of $G = 4.8 \mu\text{m}$. It clearly shows that the horizontal electric fields penetrate deeply into the LC layer. As a result, the Z-shaped structure is able to achieve very high transmittance throughout the whole period, except the regions near the edge of the passivation layer, which are negligibly small.

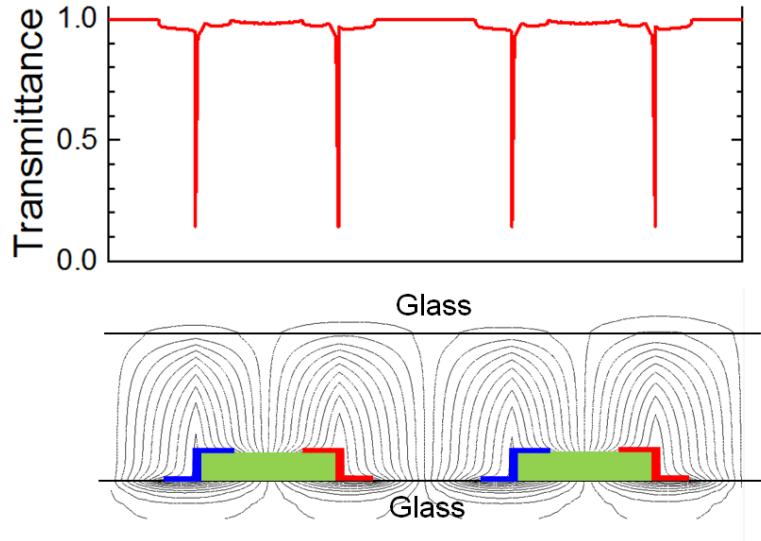


Figure 4.5. On-state transmittance profile (upper) and the electric potential distribution diagram (lower) of the Z-shaped electrode structure ($L = 4.0 \mu\text{m}$, $G = 4.8 \mu\text{m}$, $\lambda = 550\text{nm}$).

4.2.2 Contrast Ratio

Blue phase liquid crystal behaves like an optically isotropic medium when no voltage is applied. As a result, the dark-state light leakage only occurs at an off-axis incidence that comes from the effective angle deviation between two crossed linear polarizers, i.e., two crossed linear polarizers at normal incidence is no longer perpendicular to each other at an oblique incidence. This light leakage deteriorates the viewing angle performance unfavorably. At the voltage-on state, although electric field induces birefringence and the LC index ellipsoid is elongated, the overall cubic symmetry of blue phase does not change. This leads to a symmetric view angle performance.

Figure 4.6(a) plots the contrast ratio contour of Z-shaped electrodes. As we can see, the contrast ratio drops to $< 10:1$ when the polar angle exceeds 40° . Hence, in order to reduce off-axis light leakage of blue phase LCDs, compensation films are required. In terms of film configurations, a biaxial film [57] or a pair of positive A and positive C uniaxial films [26] are often used, while a biaxial film is preferred for high-end LCDs. In our simulations, the BPLC using Z-shaped electrodes are compensated by adding a half-wave biaxial film before the analyzer in order to reduce the off-axis light leakage at dark state. The parameters of the biaxial film are as follows: $n_x = 1.521$, $n_y = 1.519$, $n_z = 1.520$ and the biaxial film thickness is $137.5\mu\text{m}$. For the compensation of viewing angle, the n_x axis is placed parallel to the absorption axis of the top linear polarizer. The viewing angle of the Z-shaped structure using stripe electrodes is shown as the iso-contrast plot in Figure 4.6(b), where the viewing angle with contrast ratio higher than $100:1$ covers over 80° for all viewing directions.

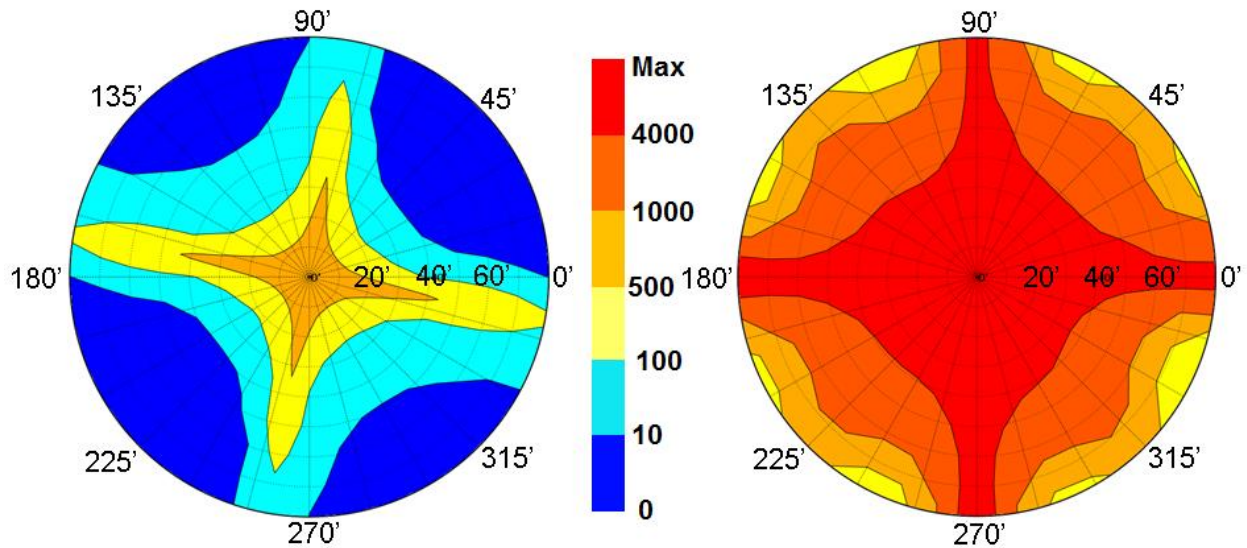


Figure 4.6. Calculated iso-contrast contour of Z-shaped structure (a) without and (b) with biaxial compensation film. ($L = 4.0\mu\text{m}$, $G = 4.8\mu\text{m}$, $\lambda = 550\text{nm}$).

4.2.3 Color Shift

Color shift is an important parameter describing the angular dependent color uniformity of a LCD panel. For high-end LCD devices, negligible color shift has always been a pursuit. In this section, the modeling of color shift will be introduced and we will investigate the color shift of blue phase LCDs using Z-shaped structure.

In our model, we compute the color performance of the LCD panel including light source, polarizer, LC cell, color filters, and analyzer. For simplicity but without losing generality, here we do not consider other optical elements such as diffusers or brightness enhancement films. These films are commonly used for improving viewing angle and contrast ratio, but they make little effect on the colors. Starting from the backlight unit, let us assume the emitted light from the backlight has a spectral power distribution (SPD) $S_{in}(\lambda)$. The black dashed lines in [Figure 4.7\(a\)](#) shows the SPD of a commonly employed white LED backlight using a yellow phosphor. After passing through the first polarizer, the linearly polarized light transmits through the TFT substrate, LC cell, color filters, and finally reaches the crossed analyzer, as illustrated in [Figure 1.2](#). To analyze the system color performance, we spatially divided the incident light into three channels: red (R), green (G) and blue (B). Here, we define $R(\lambda)$, $G(\lambda)$ and $B(\lambda)$ as the transmission spectra of each color filter, which are plotted [Figure 4.7\(a\)](#). Meanwhile, the transmission spectra of polarizers $P(\lambda)$ is also wavelength-dependent. Here, we take the dispersion of polarizer's absorption into consideration by using following complex refractive indices at RGB wavelengths: $n_e = 1.5 + i \cdot 1.38 \times 10^{-3}$ and $n_o = 1.5 + i \cdot 4.27 \times 10^{-5}$ at $\lambda = 450$ nm, $n_e = 1.5 + i \cdot 2.21 \times 10^{-3}$ and $n_o = 1.5 + i \cdot 3.22 \times 10^{-5}$ at $\lambda = 550$ nm, $n_e = 1.5 + i \cdot 2.42 \times 10^{-3}$ and $n_o = 1.5 + i \cdot 3.36 \times 10^{-5}$ at $\lambda = 650$ nm. The thickness of the polarizer is $200 \mu\text{m}$.

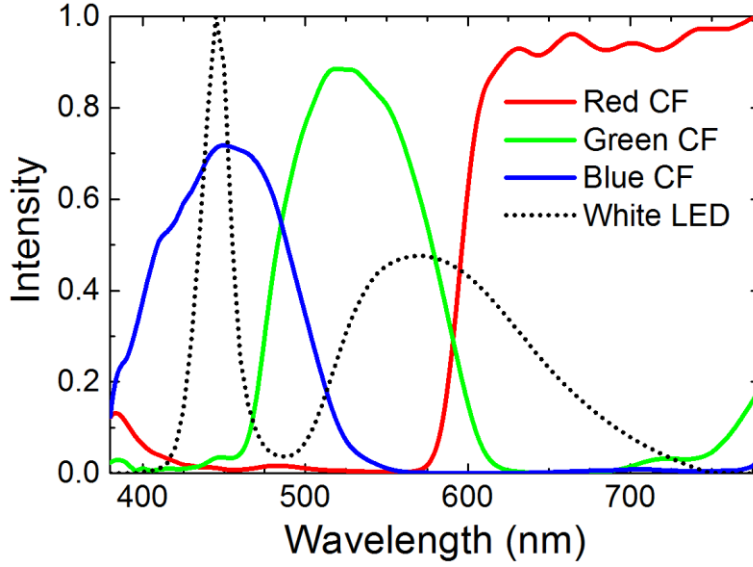


Figure 4.7. Normalized emission spectra of a white LED light source (black dashed lines) and transmission spectra of RGB color filters (color curves).

In addition, the wavelength dependent Kerr constant is also taken into consideration by the following single-band model [80]:

$$\lambda K = G \cdot \frac{\lambda^2 \cdot \lambda^{*2}}{\lambda^2 - \lambda^{*2}}, \quad (4.1)$$

where λ^* is the mean resonance wavelength and G is a proportionality constant. The transmittance of blue phase layer $LC(V, \lambda)$ depends on voltage and wavelength. To generate color hues and different gray levels, we apply different voltages to RGB sub-pixels to control their transmittance. By integrating the impacts of polarizers, TFT aperture ratio, LC cell and color filters, the SPD of output light in each channel and total SPD $S_{total}(\lambda)$ can be written as:

$$S_R(\lambda) = S_{in}(\lambda) \cdot LC(V, \lambda) \cdot P(\lambda) \cdot R(\lambda); \quad (4.2a)$$

$$S_G(\lambda) = S_{in}(\lambda) \cdot LC(V, \lambda) \cdot P(\lambda) \cdot G(\lambda); \quad (4.2b)$$

$$S_B(\lambda) = S_{in}(\lambda) \cdot LC(V, \lambda) \cdot P(\lambda) \cdot B(\lambda); \quad (4.2c)$$

$$S_{total}(\lambda) = S_R(\lambda) + S_G(\lambda) + S_B(\lambda). \quad (4.2d)$$

Here, $S_R(\lambda)$, $S_G(\lambda)$, and $S_B(\lambda)$ refer to the output SPD for the R, G, and B channels, respectively.

To quantitatively characterize the color performance of LCD system, here we choose the most commonly used tristimulus method which was established and developed by the International Commission on Illumination (CIE) [86]. Based on the human visual system, the CIE XYZ color space defines all the colors in terms of three imaginary primaries X , Y and Z , the values of which represent the luminance or brightness of the colors and can be expressed as [87]:

$$X = k \int S(\lambda) \cdot \bar{x}(\lambda) d\lambda; \quad (4.3a)$$

$$Y = k \int S(\lambda) \cdot \bar{y}(\lambda) d\lambda; \quad (4.3b)$$

$$Z = k \int S(\lambda) \cdot \bar{z}(\lambda) d\lambda; \quad (4.3c)$$

where $\bar{x}(\lambda)$, $\bar{y}(\lambda)$ and $\bar{z}(\lambda)$ represent three color matching functions and k is a constant. $S(\lambda)$ equals to output SPD for each color filter in [Equations \(4.2a\) to \(4.2c\)](#) when calculating the X , Y and Z tristimulus values for light from RGB channels. To specify which colors do X , Y and Z represent, CIE 1931 color space introduced the chromaticity coordinates x , y and z in following terms:

$$x = \frac{X}{X + Y + Z}; \quad (4.4a)$$

$$y = \frac{Y}{X + Y + Z}; \quad (4.4b)$$

$$z = \frac{Z}{X + Y + Z}; \quad (4.4c)$$

while the chromaticity in CIE 1976 uniform chromaticity scale diagram, which is also called (u' , v') diagram, is related to the (x , y) coordinates by the following equations:

$$u' = \frac{4x}{-2x + 12y + 3}; \quad (4.5a)$$

$$v' = \frac{9y}{-2x + 12y + 3}. \quad (4.5b)$$

The color shift of a LCD panel is usually measured by a spectro-radiometer with capacity of presenting u' and v' coordinates when the panel is set at the full-bright state. The chromaticity coordinates u' and v' are measured in the visually most color deviating areas such as the horizontal, vertical or diagonal directions of a LCD panel. Based on Equations (4.5a) to (4.5b), $\Delta u'v'$ at any two positions (1 and 2) can be calculated using following equation:

$$\Delta u'v' = \sqrt{(u'_2 - u'_1)^2 + (v'_2 - v'_1)^2}. \quad (4.5)$$

where (u'_2 , v'_2) and (u'_1 , v'_1) represent the (u' , v') values at an oblique viewing angle and the normal viewing angle, respectively.

In simulations, the incident angle is defined as the angle between the light incident direction and the normal of the LCD panel, which is referred as the theta angle θ thereafter. In our simulations, we varied θ from -80° to 80° , and scan the backlight across the whole 360° azimuthal angle (φ) at 10° step for every chosen θ . First, we study the color shift of film-compensated Z-shaped structures using stripe electrode, as depicted in Figure 4.8(a). Figure 4.9(a) plots the calculated color shift in CIE 1976 diagram from different azimuthal incident angles at the full-bright gray level G255. As the incident angle increases, color shift becomes more severe. To quantitatively evaluate angular color uniformity, we use Equation (4.5) to calculate the $\Delta u'v'$

values at different azimuthal and polar angles. The color shift of the stripe electrode structure is $\Delta u'v' = (0.007, 0.011, 0.090)$ for RGB primaries, respectively. Blue primary has most severe color shift: $\Delta u'v' = 0.090$ at $\theta = 80^\circ$. The accuracy of the colors is usually characterized by human eye sensitivity, where one JNCD (Just Noticeable Color Difference) = $\Delta u'v' = 0.004$ [88]. JNCD offers an accurate and objective way to evaluate the color accuracy of a display in terms of the eye's sensitivity to color. Typically, color errors less than three JNCDs are considered visually indistinguishable from perfect.

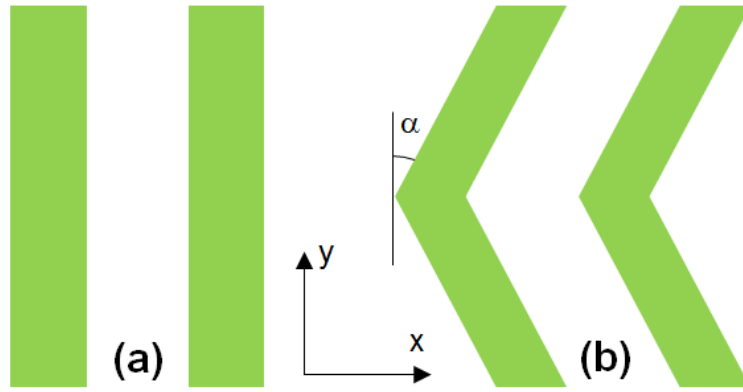


Figure 4.8. Top view of (a) stripe shaped electrodes and (b) zigzag shaped electrodes.

Since the stripe electrodes exhibits a severe color shift at large viewing angle, zigzag multi-domain electrodes have been proposed to overcome this drawback [89]. In zigzag structure, the electrode arms are bent at an angle α with respect to the y axis in the x - y plane, as [Figure 4.8\(b\)](#) shows. As a result, the Kerr effect-induced birefringence is in the complementary directions between each subdomain, resulting in a better and more uniformly compensated bright state. In order to achieve optimal viewing angle performance, we set α at 45° [89] and simulated the color shift of film-compensated zigzag electrodes, as shown in [Figure 4.9\(b\)](#). We can see the color shift is significantly reduced in zigzag structure. Quantitatively, the $\Delta u'v'$ values are reduced to (0.0016,

0.0018, 0.0055) for RGB primaries at $\theta = 80^\circ$, respectively. Compared to stripe electrodes, zigzag electrodes have reduced color shift by $> 15X$, and thus exhibiting unnoticeable color shift.

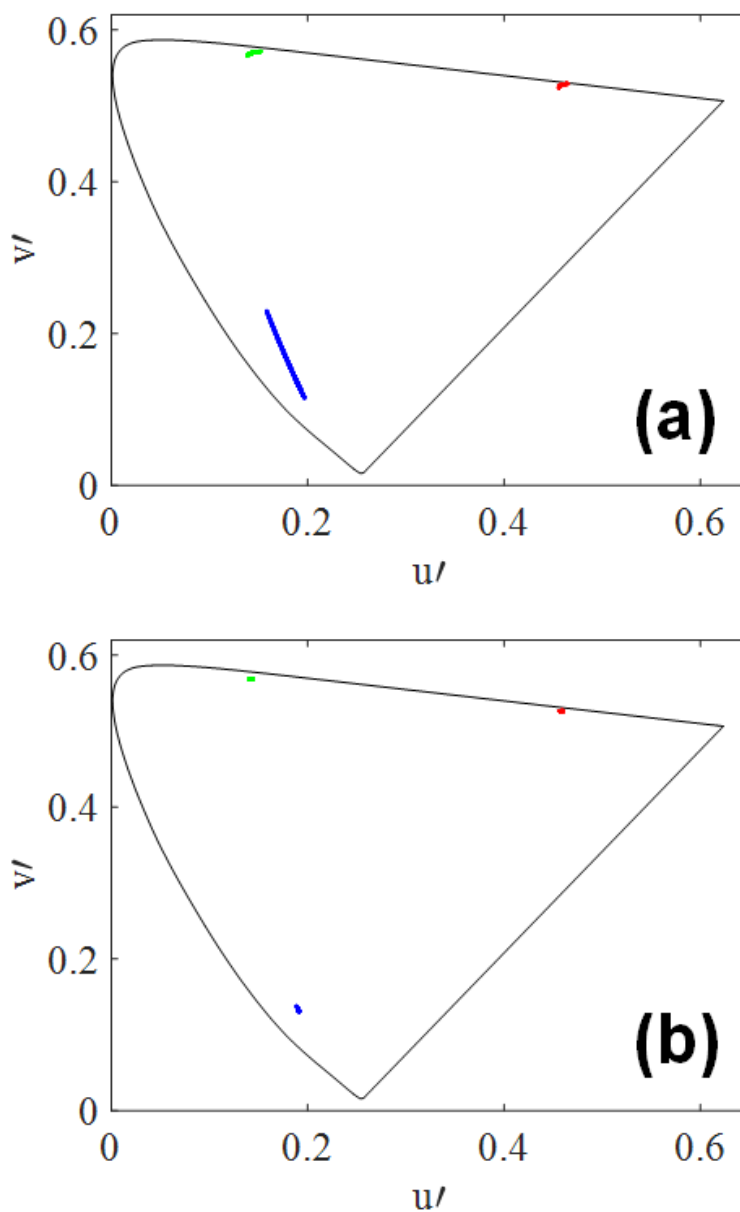


Figure 4.9. Color shift of RGB primaries film-compensated Z-shaped structure: (a) stripe electrodes, (b) zigzag electrodes. The backlight is white LED.

4.2.4 Grayscale Inversion

At the voltage-on state, blue phase is a birefringent material. Its phase retardation depends on the applied voltage, wavelength, and viewing angle. Hence, the image at off-axis viewing direction may be distorted. As a matter of fact, it is widely known that LCD panels usually have one viewing side in which color of the image change suddenly after exceeding specified view angle. This phenomenon is called *grayscale inversion*, which is also an important factor evaluating the off-axis image quality.

In simulations, we evaluated the gray inversion of Z-shaped BPLC using stripe and zigzag electrodes. To compare the gray inversion, we transform the transmittance into gamma curves based on the equation of $T = (GL/255)^{2.2}$, where GL stands for gray level. All the gray levels were considered (G0 - G255) and the gamma curves of stripe and zigzag electrodes are plotted in [Figure 4.10\(a\)](#) and [4.10\(b\)](#), respectively. Here, the azimuthal viewing angle is along the diagonal direction, where the gray inversion is the most severe.

For stripe electrodes, we can see that gray inversion appears at high gray levels. The most severe gray inversion occurs at G243, with 109.39% transmittance at polar angle $\theta = 60^\circ$. Although human eyes are more sensitive to the gray inversion at lower gray levels than higher ones, such a severe gray inversion would still affect the image qualities, thus causing aforementioned color shift. In contrast, for zigzag electrodes, gray inversion is reduced significantly, as shown in [Figure 4.10\(b\)](#). At viewing angle $\theta = 60^\circ$, gray inversion barely appears. To quantitatively compare the gray inversion, we used the off-axis image distortion index $D(\theta, \phi)$, which can be defined as [90]:

$$D(\theta, \phi) = \left\langle \left| \frac{\Delta T_{i,j(\text{on-axis})} - \Delta T_{i,j(\text{off-axis},\theta,\phi)}}{\Delta T_{i,j(\text{on-axis})}} \right| \right\rangle_{i,j=0-255} \quad (4.6)$$

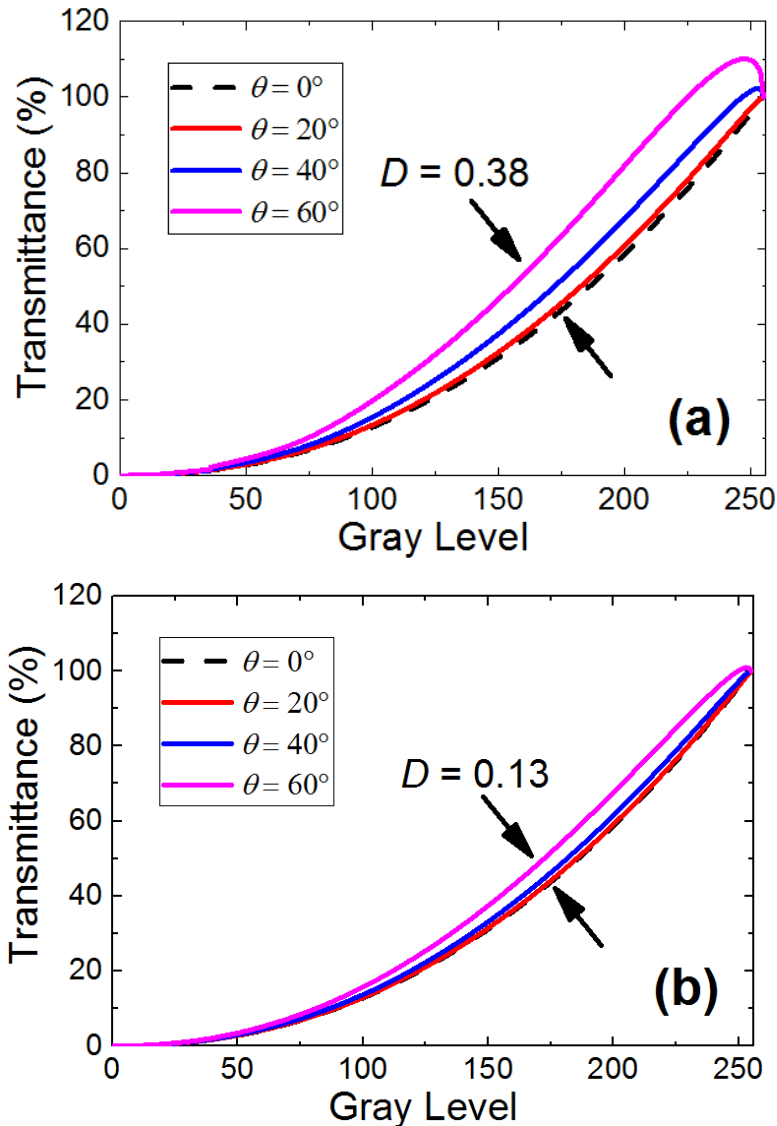


Figure 4.10. Viewing angle dependence of gamma curves for film-compensated Z-shaped BPLC:

(a) stripe electrode and (b) zigzag electrode along the diagonal direction.

where ΔT_{ij} means transmittance difference between i^{th} and j^{th} gray levels, and $\langle \rangle$ denotes the average for all cases of arbitrary grays. The $D(\theta, \phi)$ value ranges from 0 to 1. If $D < 0.2$, then the image distortion is indistinguishable by the human eye. Our simulations show that stripe and zigzag structures D values of 0.38 and 0.13, respectively. This implies the zigzag electrodes have reduced the image distortion to unnoticeable extent and improved off-axis image quality

significantly. This is due to the fact that induce birefringence is in the complementary directions between each subdomain.

4.3 Analysis of Device Parameters

4.3.1 *Protrusion Height Effect*

In protrusion electrode structures [60, 91], the protrusion height is crucial in lowering the operation voltage. Higher protrusion enables the electric field to penetrate deeper into the BPLC bulk, and thus reducing the operation voltage significantly. This trend applies to the Z-shape electrode structures as well.

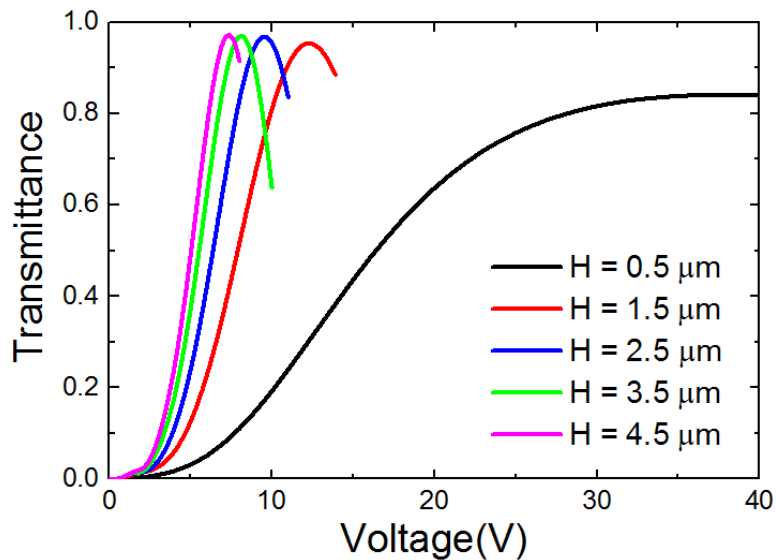


Figure 4.11. Calculated VT curves of BPLC cells using Z-shaped electrodes under various heights H conditions ($\theta = 90^\circ$, $W_1 = W_2 = 1.0\mu\text{m}$; $L = 4.0\mu\text{m}$; $G = 4.8\mu\text{m}$, $\lambda = 550\text{nm}$).

Figure 4.11 plots the calculated VT curves using the Z-shaped electrode structure with various protrusion heights of the passivation layer. Here, the VT curve for the aforementioned scenario of $H = 3.5\mu\text{m}$ is plotted as the green solid curve. When H increases to $4.5\mu\text{m}$, the driving

voltage is reduced to 7.3V, while the peak transmittance is maintained at 97.1%, as plotted by the magenta solid curve. This is due to the fact that the penetration depth of electric field is enhanced [60]. On the other hand, when H drops to $2.5 \mu\text{m}$, the penetration depth of the electric field becomes shallower. As a result, the operation voltage increases to 9.5V, as plotted by the blue solid curve. When H continues to decrease, the driving voltage increases accordingly.

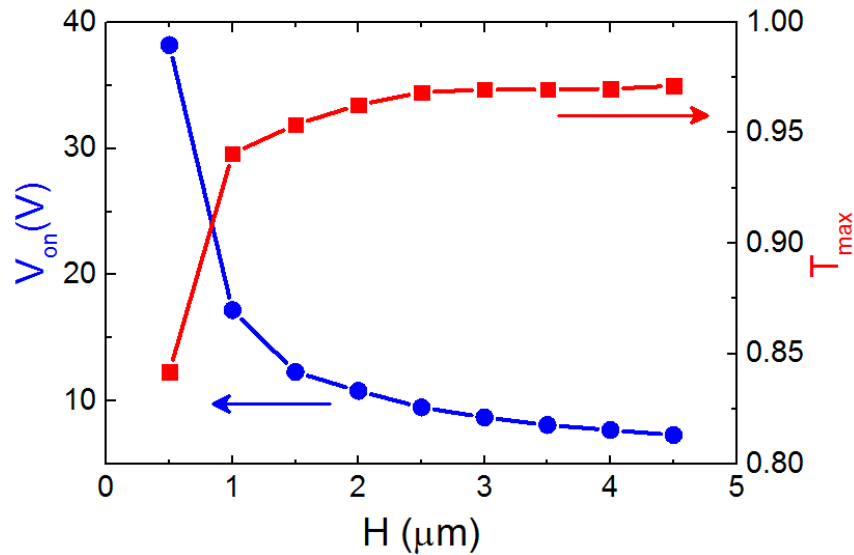


Figure 4.12. A summary of the peak transmittance (T_{max}) and on-state voltage (V_{on}) of BPLC using Z-shaped electrodes under various heights H conditions ($\lambda = 550\text{nm}$).

In order to investigate the protrusion height effect more thoroughly, we varied H in the range between $0.5 \mu\text{m}$ and $4.5 \mu\text{m}$ with a step of $0.5 \mu\text{m}$ and simulated their VT curves. Figure 4.12 summarizes the peak transmittance (T_{max}) and on-state voltage (V_{on}) under different H conditions. The trend is clear: as H decreases, the driving voltage increases dramatically and the peak transmittance also decreases. When $H = 0.5 \mu\text{m}$, the driving voltage is as high as 38.2V and peak transmittance is reduced to 84.2%. Therefore, a high H is very helpful in achieving high transmittance and low driving voltage simultaneously.

4.3.2 Dimension Effect

The electrode dimension plays an important role in determining the electro-optical properties of IPS BPLC cells. When L increases or decreases, in order to maintain a high transmittance, G needs to increase or decrease accordingly.

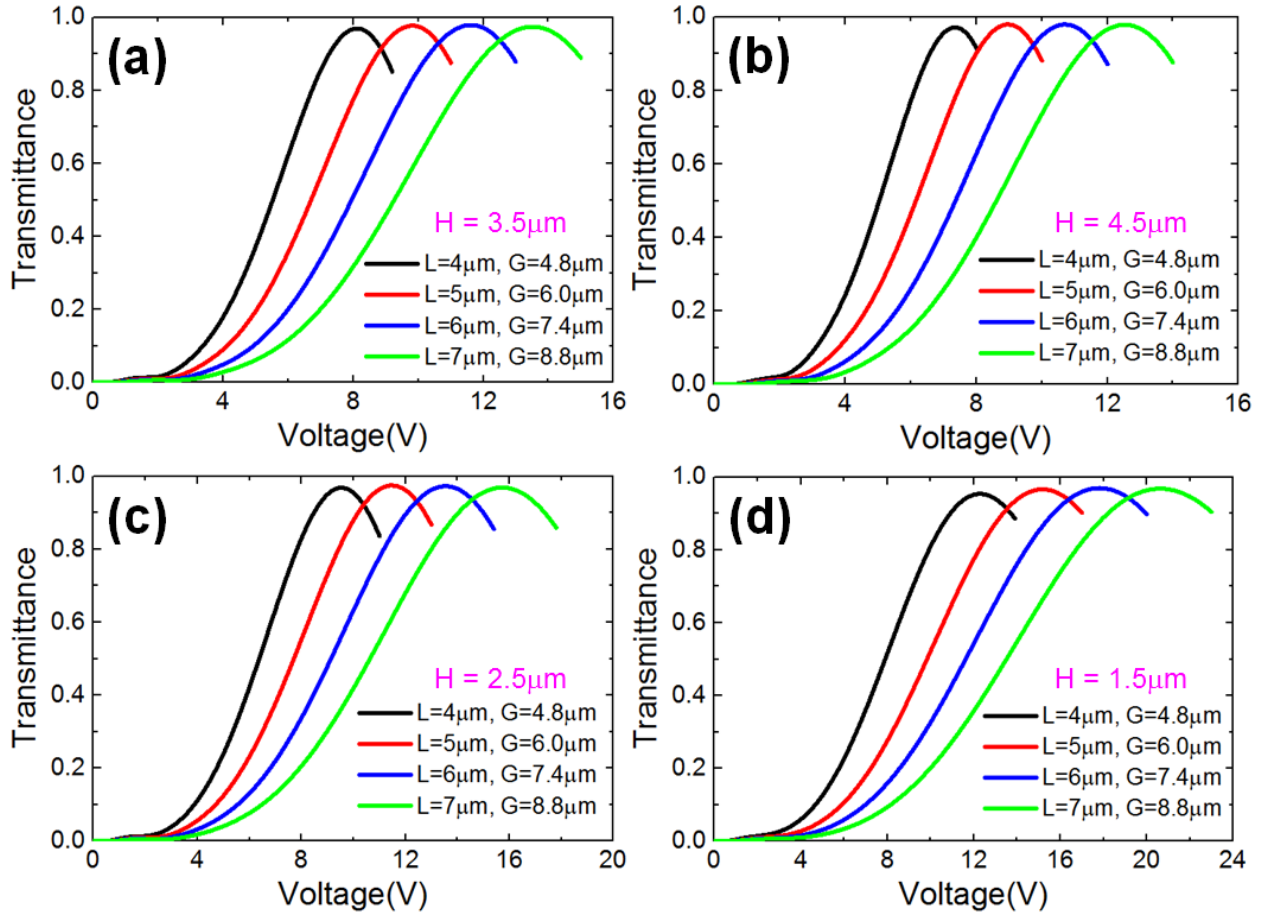


Figure 4.13. Calculated VT curves of BPLC cells using Z-shaped electrodes under different H conditions. (a) $H = 3.5 \mu\text{m}$, (b) $H = 4.5 \mu\text{m}$, (c) $H = 2.5 \mu\text{m}$ and (d) $H = 1.5 \mu\text{m}$ ($\lambda = 550 \text{nm}$).

Figure 4.13(a) plots the calculated VT curve using the Z-shaped electrode structure with various L and G conditions at $H = 3.5 \mu\text{m}$. Here, the VT curve for the aforementioned scenario of $L = 4.0 \mu\text{m}$, $G = 4.8 \mu\text{m}$ is plotted as black solid curve. When L increases to $5.0 \mu\text{m}$, G should

increase to $6.0 \mu\text{m}$ in order to maintain a high transmittance, as shown by the red solid curve, where the driving voltage is 9.8V and peak transmittance is 97.7% . When (L, G) further increases to $(6.0 \mu\text{m}, 7.4 \mu\text{m})$, the driving voltage increases to 11.6V while the transmittance is maintained at 97.9% (blue solid curve). The general trend is as L and G increase, the driving voltage increases. In order to maintain high transmittance, the ratio of G/L of the Z-shaped electrodes should be kept at around 1.2. This optimal G/L ratio of 1.2 to achieve high transmittance not only applies to the scenario of $H = 3.5 \mu\text{m}$, but also applies to other scenarios with different passivation thickness. Figures 4.13 (b)-(d) plot the calculated VT curve using the Z-shaped electrode structure with various L and G conditions at $H = 4.5, 2.5$ and $1.5 \mu\text{m}$, respectively. It shows that the optimal G/L ratio to achieve high transmittance is also around 1.2 for other protrusion heights.

4.3.3 Electrode Width Effect

In the descriptions above, $W_1 = W_2 = 1.0 \mu\text{m}$ is used to explain the physical principles. Notwithstanding, in this design, W_1 and W_2 can be same or different, and can vary in a wide range depending on the fabrication technique. The scenarios of $W_1 \neq W_2$ will be discussed in Section 4.4. In this section, we focus on the scenario of $W_1 = W_2$ and investigate the electrode width effect.

Figure 4.14 shows the calculated VT curve using Z-shaped electrodes with various electrode width conditions while $L = 5.0 \mu\text{m}$ and $G = 6.0 \mu\text{m}$. When the electrode width $W_1 = W_2$ increases from $1.0 \mu\text{m}$ to $1.5 \mu\text{m}$ and $2.0 \mu\text{m}$, the driving voltage remains the same, but the peak transmittance decreases from 97.2% to 95.3% , and then to 93.8% . This is due to the slightly lower transmittance on the top of the ITO electrodes, as shown in Figure 4.5. Hence, a larger ITO electrode width leads to a lower transmittance. In order to achieve high transmittance, the electrode width W should be as narrow as possible.

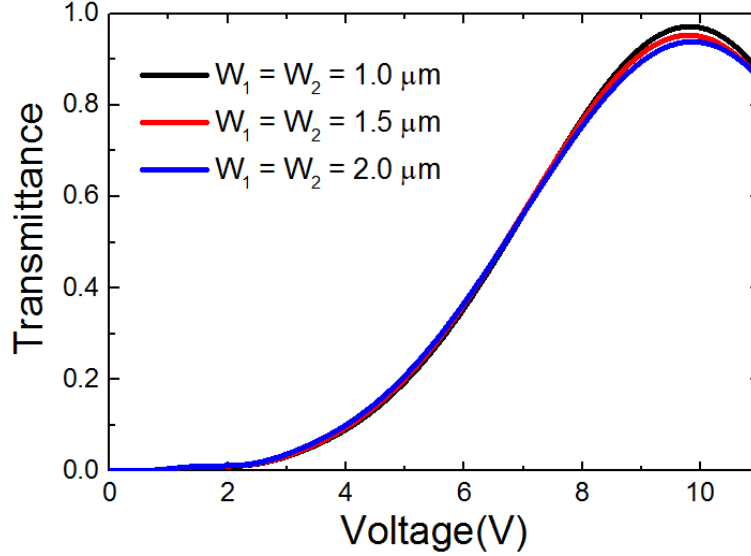


Figure 4.14. Calculated VT curves of BPLC cells using Z-shaped electrodes under various electrode width conditions. ($\theta_t = 90^\circ$, $H = 3.5\mu\text{m}$; $L = 5.0\mu\text{m}$; $G = 6.0\mu\text{m}$, $\lambda = 550\text{nm}$).

4.3.4 Taper Angle Effect

The taper angle plays a critical role in determining the electro-optical performance of the Z-shaped electrode structures. In aforementioned discussions, θ_t was set at 90° in order to achieve high transmittance and low voltage simultaneously. When θ_t deviates from 90° , both transmittance and voltage would be deteriorated. Figure 4.15 shows the calculated VT curve using the Z-shaped electrode structure when the taper angle drops from 90° to 85° . Here, the VT curve for the scenario of $\theta_t = 90^\circ$ is plotted as the black solid curve. It clearly shows that as taper angle decreases, the driving voltage increases and the peak transmittance decreases dramatically. For example, when the taper angle decreases from 90° to 89° , the driving voltage increases from 8.1V to 14.2V, and the transmittance drops from 97.7% to 89.9%. Hence, in order to maintain the transmittance higher than 90%, the taper angle should be steeper than 89° .

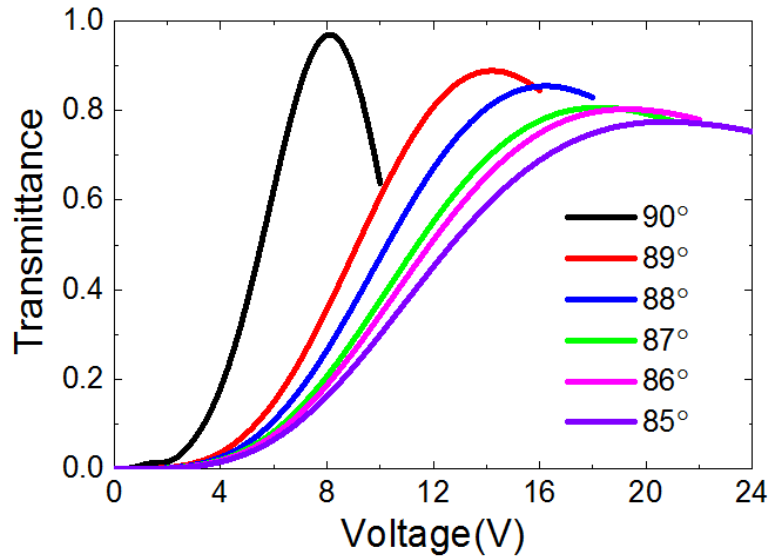


Figure 4.15. Calculated VT curves of BPLC cells using Z-shaped electrodes under various taper angle conditions. ($H = 3.5\mu\text{m}$, $W_1 = W_2 = 1.0\mu\text{m}$; $L = 4.0\mu\text{m}$; $G = 4.8\mu\text{m}$, $\lambda = 550\text{nm}$).

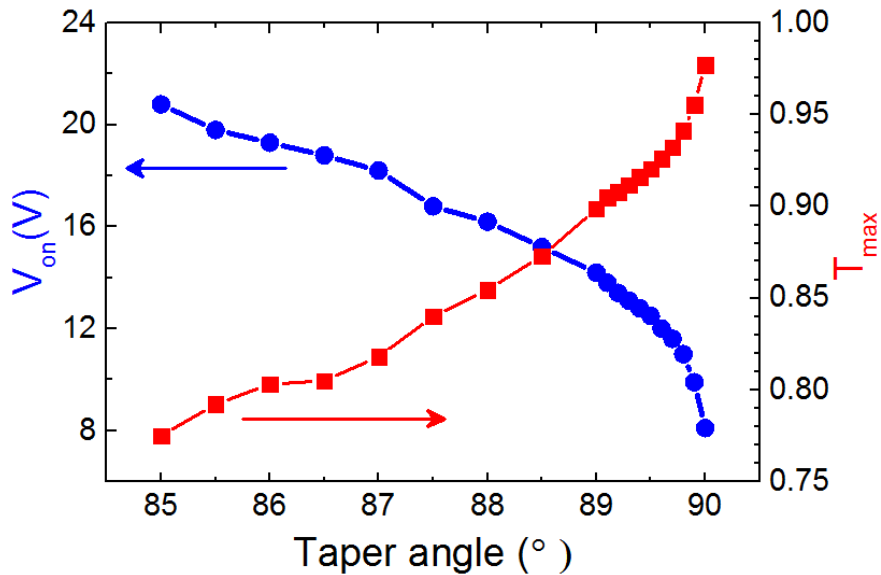


Figure 4.16. A summary of the peak transmittance (T_{max}) and on-state voltage (V_{on}) of BPLC using Z-shaped electrodes under various taper angle conditions ($\lambda = 550\text{nm}$).

Figure 4.16 summarizes the peak transmittance (T_{max}) and its corresponding driving voltage (V_{on}) under different θ_t conditions. The general trend is that driving voltage increases and

the peak transmittance decreases dramatically as θ_t decreases from 90° . When $\theta_t = 85.5^\circ$, the driving voltage increases to 19.8V, while the peak transmittance decreases to below 80%. Hence, θ_t should be as close to 90° as possible in order to achieve high transmittance and low driving voltage simultaneously.

4.4 Variations in Device Structures

The Z-shaped electrode structure is able to achieve high transmittance and low operation voltage simultaneously. In addition, there is a wide freedom in device fabrication. Some possible variations in device structures are discussed below.

4.4.1 *L-shaped Electrodes*

In the Z-shaped electrode structure, the ITO electrodes cover the surfaces of the passivation protrusions and bottom substrates. In contrast, in the L-shaped electrode structure, the common and pixel electrodes only cover the sidewall of passivation protrusions and bottom substrate with electrode width of W_2 , but don't cover the top surface of passivation layer, as illustrated in [Figure 4.17](#). Same with the Z-shaped electrode structure, the LC layer is interposed between two substrates, which can be further sandwiched between two crossed polarizers.

[Figure 4.18](#) shows the calculated VT curves using the L-shaped electrode structure with different electrode dimensions. Here, the taper angle of the passivation protrusions is set at $\theta = 90^\circ$ and the height is $H = 3.5\mu\text{m}$. The black and red solid curves stand for the VT curves of the L-shaped electrodes structures with different L and G conditions while the electrode width is kept at $W_2 = 1.0\mu\text{m}$. Both structures are able to achieve $> 98\%$ transmittance, while the driving voltage

is below 10V. When the electrode width increases to $W_2 = 2.0 \mu\text{m}$, the driving voltage keeps almost the same, while the peak transmittance drops slightly, but still keeps at $> 97\%$, as shown by black and red dashed curves. Same with the Z-shaped electrode structure, in order to maintain the high transmittance, the optimal G/L of the L-shaped structure should be around 1.2.

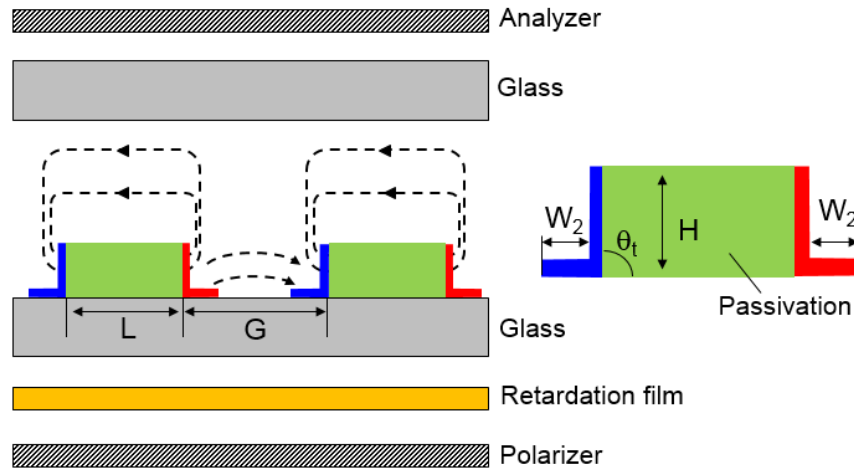


Figure 4.17. Cross-sectional view of a BPLC cell using L-shaped electrodes.

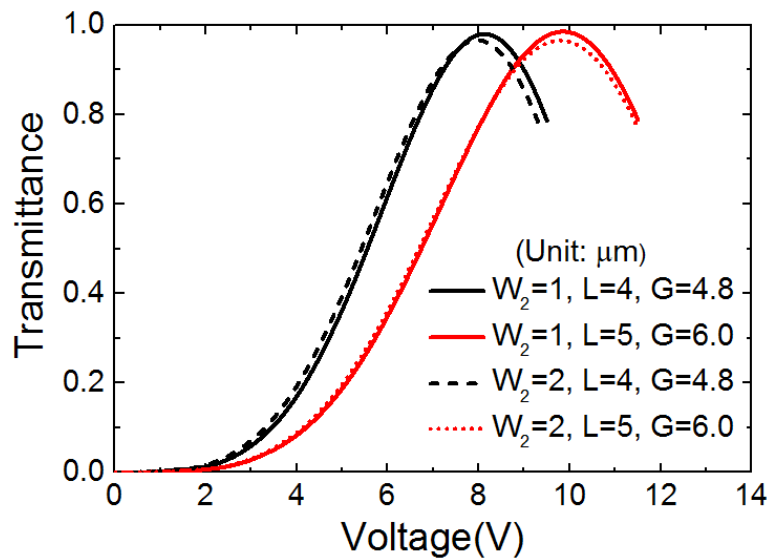


Figure 4.18. Calculated VT curves of BPLC cells using L-shaped electrodes. ($H = 3.5 \mu\text{m}$, $\theta_t = 90^\circ$; $\lambda = 550\text{nm}$).

4.4.2 7-shaped Electrodes

Another possible variation in the structure is the 7-shaped electrodes. Different from Z- and L-shaped electrodes, the common and pixel electrodes only cover the sidewall and the top surface of passivation layer with electrode width of W_1 , but don't cover the bottom substrate, as illustrated in Figure 4.19.

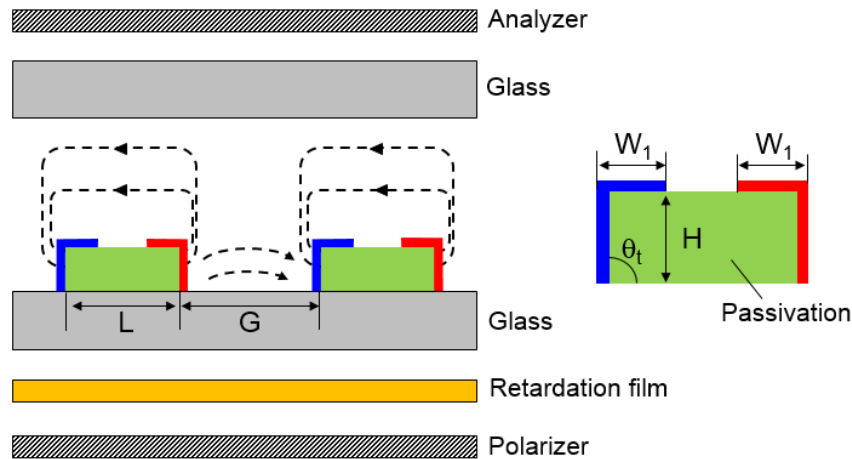


Figure 4.19. Cross-sectional view of a BPLC cell using 7-shaped electrodes.

Figure 4.20 shows the calculated VT curves using the 7-shaped electrode structure with different electrode dimensions. Here, the taper angle of the passivation protrusions is set at $\theta = 90^\circ$ and the height is $H = 3.5 \mu\text{m}$. The black and red solid curves stand for the VT curves using the 7-shaped electrode with different L and G conditions while the electrode width is kept at $W_1 = 1.0 \mu\text{m}$. Both structures are able to achieve $>98\%$ transmittance, and their driving voltages are 9.2V and 11.1V, respectively. When the electrode width increases to $W_1 = 2.0 \mu\text{m}$, the peak transmittance keeps almost the same, while the driving voltage increases to 12.9V and 14.2V, respectively; as depicted by blue and green solid curves. Same with aforementioned structures, in order to maintain high transmittance, the optimal G/L ratio of the L-shaped structure is around ~ 1.2 .

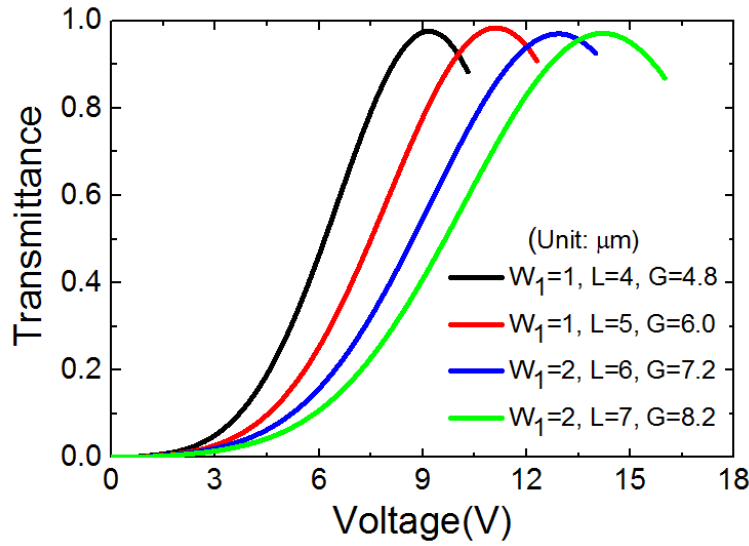


Figure 4.20. Calculated VT curves of BPLC cells using 7-shaped electrodes. ($H = 3.5\mu\text{m}$, $\theta = 90^\circ$; $\lambda = 550\text{nm}$).

4.4.3 I-shaped Electrodes

From the discussions above, the vertical electrodes deposited on the sidewalls of passivation protrusions play a crucial role in enhancing the penetration depth of horizontal electric field and consequently lowering the operation voltage. Thus, a possible variation in structure is that the common and pixel electrodes only cover the sidewall of passivation layer, but don't cover the top surface of the passivation layer or bottom substrate, as depicted in Figure 4.21. Therefore, both common and pixel electrodes appear to be I-shaped.

Figure 4.22 shows the calculated VT curves using the I-shaped electrode structure with different electrode dimensions. Here, the taper angle of the passivation protrusions is set at $\theta = 90^\circ$ and the height is $H = 3.5\mu\text{m}$. The black solid curve stands for the VT curves using the I-shaped electrode with $L = 4.0\mu\text{m}$ and $G = 4.8\mu\text{m}$, where the peak transmittance is 98.7% at a driving voltage of 9.1V. When device dimension increases to $L = 5.0\mu\text{m}$ and $G = 6.0\mu\text{m}$, the driving

voltage increases to 11.1V while the peak transmittance remains very high (98.9%), as shown by red solid curve. Same with aforementioned structures, the optimal G/L ratio of the L-shaped structure is ~ 1.2 for achieving high transmittance.

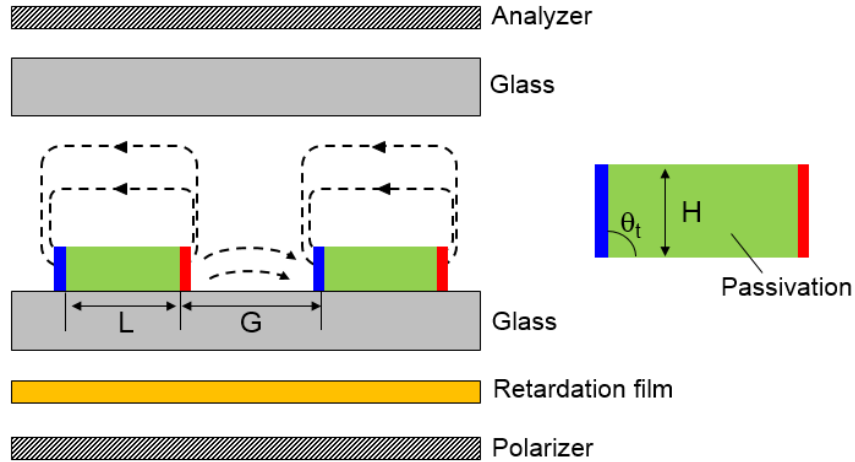


Figure 4.21. Cross-sectional view of a BPLC cell using I-shaped electrodes.

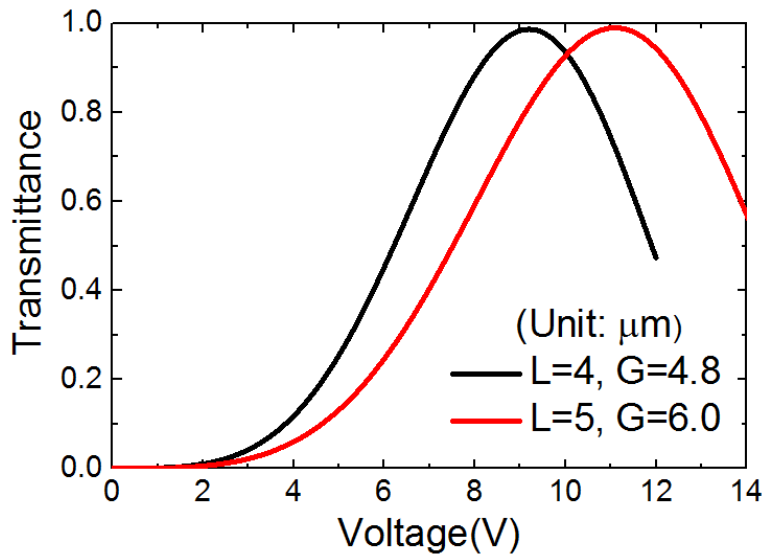


Figure 4.22. Calculated VT curves of BPLC cells using I-shaped electrodes. ($H = 3.5\mu\text{m}$, $\theta = 90^\circ$; $\lambda = 550\text{nm}$).

4.5 Summary

In this chapter, we have proposed a new device structure for dramatically reducing the operating voltage and enhancing the transmittance of blue phase LCDs. The device shows high tolerance in fabrications. By optimizing the device structure, we have successfully reduced the operating voltage to lower than 10V and improved optical transmittance to $> 95\%$, showing comparable or even better performance than the mainstream nematic LCDs. More attractively, this is the first time to achieve such a high transmittance in BPLC devices without implementing a collimated oblique incident backlight. By using zigzag structure, the color shift and grayscale inversion are in unnoticeable range. With continuous development in LC materials, the voltage of Z-shaped structure can be further reduced and widespread applications of blue phase LCDs is foreseeable.

CHAPTER 5. DYNAMIC RESPONSES OF BLUE PHASE LIQUID CRYSTALS

The fast response time of blue phase liquid crystal renders it as an excellent candidate for reducing motion blurs in LCDs and enabling color sequential displays [92, 93]. The elimination of spatial color filters triples optical efficiency and resolution density. However, it was recently found that the response time of polymer-stabilized blue phase liquid crystals could vary from microseconds to several milliseconds [59, 94], depending on the liquid crystal viscosity, pitch length, polymer network, and electric field strength. If the response time of blue phase liquid crystals increases to several milliseconds, then one of their major advantages over nematic liquid crystals would be lost, as the color sequential displays demand the response time of LCDs to be within submillisecond range. Hence, there is an urgent need to understand the dynamic response behaviors of blue phase liquid crystals in order to improve the response time. In this chapter, we will investigate the dynamic response behaviors of blue phase liquid crystals under different electric fields. We find that electrostriction effect is the root cause for the observed slow response time and severe hysteresis under strong electric field.

5.1 Electric Field Effects

Regarding the electric field effects, three distinct transformations in blue phase liquid crystals would occur as the field intensity increases: local liquid crystal reorientation (manifested by the induced birefringence from Kerr effect), lattice distortion (known as electrostriction effect) and eventually phase transition to lower symmetry phases (e.g. chiral nematic phase).

Microscopically speaking, the blue phase lattice consists of cylinders in which the liquid crystal molecules have a double-twist alignment, as illustrated in [Figure 5.1\(a\)](#). Although the

structure is named as “double-twist”; in fact, there is an unlimited number of helical axes within each cylinder. As a result, from the macroscopic viewpoint, blue phase appears optically isotropic at the voltage-off state. Upon application of an electric field, the liquid crystal directors within the shortly correlated nematic domains existing in the double-twist cylinders are reoriented locally, as shown in [Figure 5.1\(b\)](#). Consequently, the order parameter of LC directors increases under electric fields and the isotropic medium becomes anisotropic, as manifested by the change in birefringence, which is governed by the Kerr effect [53, 73]. As a matter of fact, the helical pitch of BPLC is usually very short ($\sim 100\text{nm}$). Thus, the response time of this effect is extraordinarily faster, usually less than 1ms [95] or even shorter in the microsecond range [94], which is much faster than the Fréedericksz transitions in nematic LCs [96]. When the applied field becomes stronger, polymer networks are deformed and accordingly, the three-dimensional blue phase lattices are distorted, leading to electrostriction [97-101], as shown in [Figure 5.1\(c\)](#). The term “electrostriction” is widely used in solid-state physics for describing a property of all electrical non-conductors or dielectrics that causes them to change their shape under the application of an electric field. Since the distortion of blue phase lattice usually involves as many as $\sim 10^7$ LC molecules, it has a characteristic time much longer than that of the Kerr effect, usually around several milliseconds or even longer [99]. When electric field becomes even stronger, diverse changes such as extension of the chiral pitch and phase transition to the chiral nematic phase occur, as shown in [Figure 5.1\(d\)](#). The helical structures of blue phase lattice are unwound, leading to irreversible structural changes. Thus, the electrostriction and phase transition are main reasons causing hysteresis and slowing the response time. In order to understand the dynamic response behaviors of blue phase liquid crystals, we need to differentiate three electric field effects quantitatively, as will be discussed below.

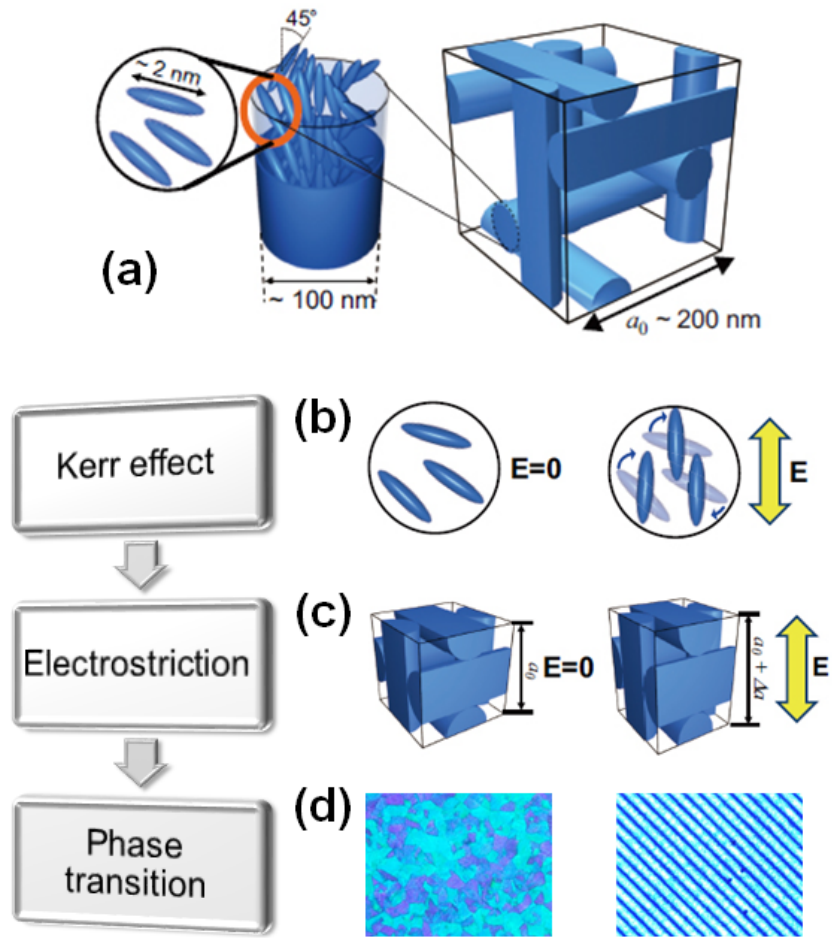


Figure 5.1. Electric field effects in blue phase liquid crystals.

5.2 Experimental Setup

In experiments, we employed a large $\Delta\varepsilon$ nematic LC host JC-BP06N (JNC, Japan) [69] whose physical properties are listed as follows: $\Delta n = 0.156$ at $\lambda = 633$ nm, $\Delta\varepsilon = 473.1$ at 100 Hz and 23°C, and clearing temperature $T_c = 73.8^\circ\text{C}$. The BPLC host was then mixed with chiral dopant R5011 (HCCH, China) and two photocurable monomers: TMPTA (1,1,1-Trimethylolpropane Triacrylate, Sigma Aldrich) and RM257 (Merck). To investigate how polymer networks affect the electro-optic response of blue phase liquid crystals, we adjusted the monomer concentration while keeping the weight ratio between LC host

and chiral dopant unchanged (96.8: 3.2), as listed in [Table 5.1](#).

Table 5.1. Material recipes and cell gap of three samples.

	Sample A	Sample B	Sample C
RM257	5.26%	6.75%	7.01%
TMPTA	3.46%	4.17%	4.60%
JC-BP06N	88.33%	85.21%	85.54%
R5011	2.95%	2.87%	2.85%
Cell gap	7.84 μm	7.83 μm	7.77 μm

The weight ratio between RM257 and TMPTA was kept at $\sim 1.5:1$. To rule out the influence of non-uniform electric field in a commonly employed in-plane switching (IPS) cell [91], we injected the blue phase precursor into a vertical field switching (VFS) cell [59, 102]. The VFS cell consists of two planar ITO (indium tin oxide) glass substrates without surface alignment layer, and the electric field is along the longitudinal direction. [Table 5.1](#) lists the compositions of three samples studied and their cell gaps. Next, we placed the VFS cell on a Linkam temperature controllable stage, let it cool to a temperature near the chiral nematic and blue phase transition temperature, and then cured it at BP-I phase with a UV light ($\lambda \sim 365$ nm, intensity 2 mW/cm^2) for 30 min. After UV exposure, the nanostructured blue phase composite was self-assembled.

[Figure 5.2](#) depicts the experimental setup for characterizing the dynamic response of a VFS cell. The transmission axes of polarizer and analyzer are set at 45° and -45° azimuthal angles with respect to the incident plane. For intensity modulation, the incident light should infringe the VFS cell at an oblique angle. Hence, we immersed the VFS cell in a glass container filled with glycerol ($n = 1.47$) for index matching purpose. This enabled the incident light to pass through the VFS cell at a large angle in order to obtain more phase retardation. In our experiments, θ was set at 45° and a 100 Hz square-wave AC signal

was applied to drive the VFS cell.

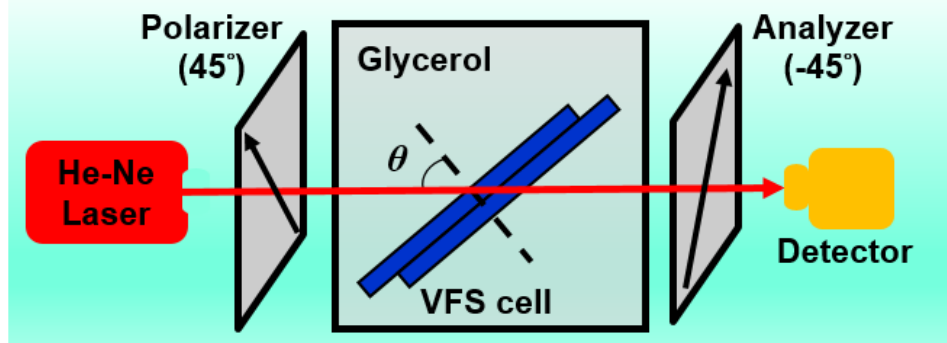


Figure 5.2. Experimental setup for characterizing the dynamic response of a VFS cell.

To measure the rise time, we applied a voltage to the VFS cell and recorded the transmittance change by a digital oscilloscope. Similarly, to measure decay time we removed the on-state voltage applied on the VFS cell instantaneously and recorded the transient transmittance change. In our experiments, the analyzer was rotated by a small angle ($\sim 2^\circ$) to compensate the polarization rotation effect from blue phase liquid crystals [103]. As a result, the measured contrast ratio was over 2000:1.

The measured change in transmittance T is related to the phase retardation δ as:

$$T = \sin^2(\delta / 2). \quad (5.1)$$

To rule out the cell gap effect and only focus on the intrinsic electro-optic properties of blue phase liquid crystals, here we convert the phase retardation to induced birefringence ($\Delta n = n_e - n_o$) using following equations [59]:

$$\delta = \frac{2\pi}{\lambda} n_o d \left[\sqrt{1 - \frac{n_g^2 \sin^2 \theta}{n_e^2}} - \sqrt{1 - \frac{n_g^2 \sin^2 \theta}{n_o^2}} \right], \quad (5.2)$$

$$n_o = n_i - \Delta n / 3, \quad (5.3)$$

$$n_e = n_i + 2\Delta n / 3. \quad (5.4)$$

where λ is the laser wavelength, n_g is the refractive index of glycerol, θ is the incident angle in the glycerol, n_i is the refractive index of blue phase liquid crystals at the voltage-off state, and n_e and n_o represent the extraordinary and ordinary refractive indices, respectively.

5.3 Double Exponential Model

The black solid lines in [Figures 5.3\(a\)](#) and [\(b\)](#) represent the measured transient Δn change during rise and decay processes using Sample B as an example when an electric field $E = 3\text{V}/\mu\text{m}$ was applied and then removed. It clearly shows that both rise and decay curves involve two distinct processes: a fast one followed by a slower one. To further understand the electric field effects in the transient Δn change process, we use exponential equations to fit the measured data. First, we use following exponential equations with single exponent to fit the rise and decay curves:

$$\Delta n(t) = \Delta n_0 \cdot (1 - e^{-t/t_r}), \quad (5.5)$$

$$\Delta n(t) = \Delta n_0 \cdot e^{-t/t_d}. \quad (5.6)$$

Here, t_r and t_d are the rise and decay time constants, while Δn_0 is the steady-state induced birefringence under an applied voltage. The fitting curves are shown by the blue dashed lines in [Figures 5.3\(a\)](#) and [\(b\)](#). We can see that Equations (5.5) and (5.6) don't fit the experimental results very well (Coefficient of determination $R^2 = 91.6\%$ and 92.6% for rise and decay, respectively). This is because the single exponential equation only accounts for the Kerr effect, and fails to take the electrostriction effect into consideration due to the difference in time constants. Thereby, we need to modify the model and include the electrostriction effect, although its contribution is relatively small. The following double exponential growth equation is introduced to describe the dynamic rise processes involving these two effects:

$$\Delta n(t) = A \times (1 - e^{-t/t_{r1}}) + B \times (1 - e^{-t/t_{r2}}), \quad (5.7)$$

where t_{r1} and t_{r2} are the rise time constants, while A and B represent the induced birefringence from Kerr effect and electrostriction effect, respectively.

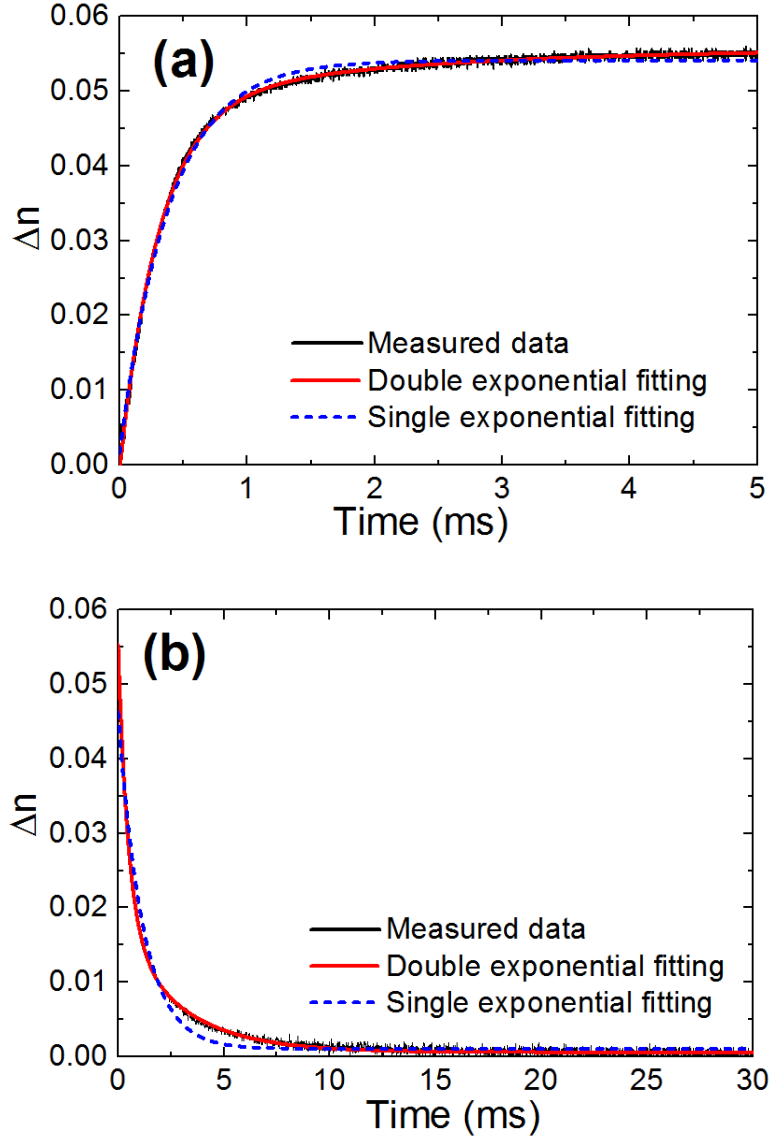


Figure 5.3. Transient (a) rise and (b) decay processes of induced birefringence for Sample B at $E = 3\text{V}/\mu\text{m}$.

For decay process, we fit the transient induced birefringence change curves with double exponential relaxation equation below [104]:

$$\Delta n(t) = C \times e^{-t/t_{d1}} + D \times e^{-t/t_{d2}}, \quad (5.8)$$

where t_{d1} and t_{d2} are the decay time constants, whereas C and D are birefringence induced by the Kerr effect and electrostriction, respectively. The fitting curves (red solid lines) in Figure 5.3 show that Equations (5.7) and (5.8) well characterize the transient rise and decay processes of induced birefringence (Coefficient of determination $R^2 > 99.7\%$ for the fittings both rise and decay curves).

In experiments, we measured the rise time behaviors of all three samples under different electric fields ascending from $1 \text{ V}/\mu\text{m}$ to $11 \text{ V}/\mu\text{m}$, and fit the experimental data with Equation (5.7). The values of t_{r1} and t_{r2} under different electric fields are plotted in Figures 5.4(a) and (b). All the values of t_{r1} shown in Figure 5.4(a) are shorter than 1ms, which well correlate with the response time of Kerr effect. In addition, Figure 5.4(a) shows a clear trend: t_{r1} decreases as E increases. This is because the liquid crystal directors within double-twist cylinders experience a stronger torque and react faster when the electric field intensity becomes stronger [95]. More interestingly, in spite of the difference in monomer concentration, t_{r1} of these three samples almost overlaps with each other. This indicates that t_{r1} is mainly determined by the LC host and chiral dopant and it is insensitive to the monomer weight ratio. The reason is that all the monomers are polymerized to form polymer networks during UV curing process and the properties (e.g. rotational viscosity γ_1 , average elastic constant k , pitch length P_0 , etc.) of the double-twist blue phase cylinders are determined by the liquid crystal host and chiral dopant. As a result, in the samples with same ratio between LC host and chiral dopant, the formed blue phase lattices are almost same and the local reorientations of LC directors within double-twist cylinders exhibit same response time. For the electrostriction effect, the magnitude of t_{r2} is around several milliseconds, much longer than t_{r1} . Notwithstanding, t_{r2} exhibits similar dependency on electric field as t_{r1} : as E increases, t_{r2} decreases. This is because a strong electric field expedites the electrostriction effect. Moreover, the value of t_{r2} depends on the monomer concentration; or more specifically, the rigidness of polymer network. In blue phase liquid crystals with a higher monomer concentration, polymer networks are more robust to prevent lattice from being distorted by the electric field,

thus helping suppress the electrostriction effect. Consequently, it takes a shorter time for the electric field to complete the stretching process of the blue phase lattices, as Figure 5.4(b) plots.

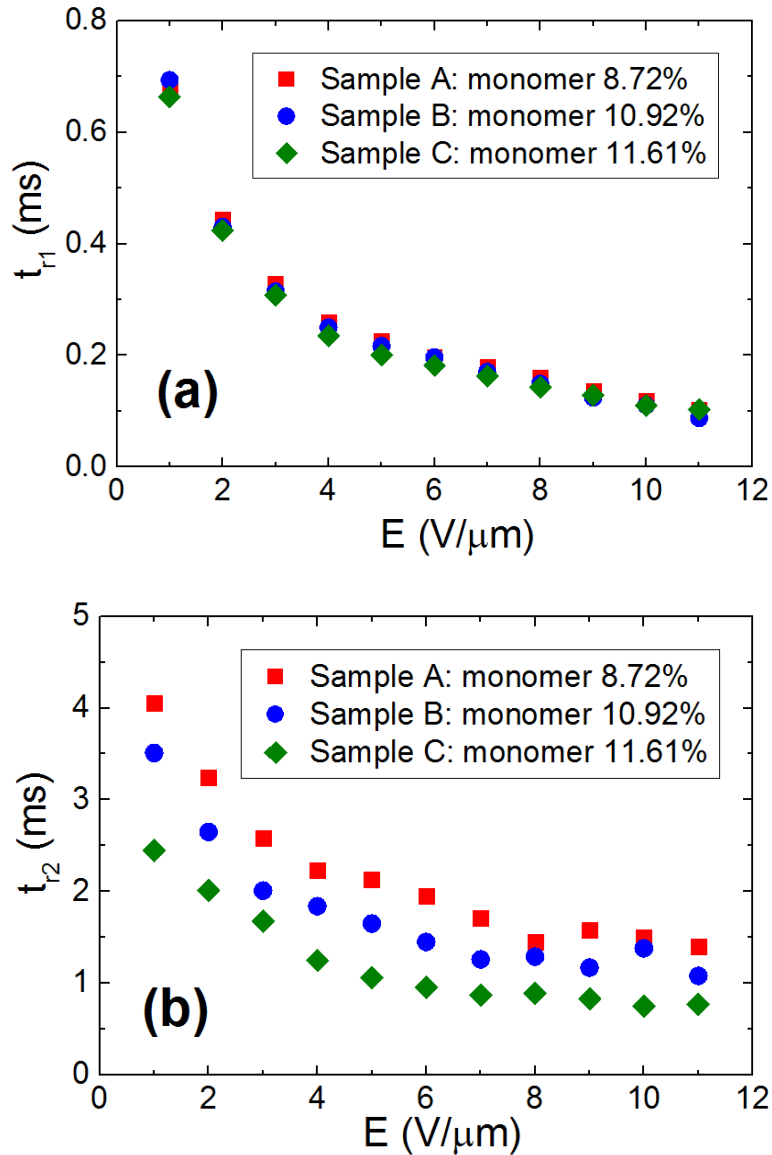


Figure 5.4. Fitted rise time constants of (a) Kerr effect t_{r1} and (b) electrostriction effect t_{r2} for samples with different monomer concentrations.

In Equation (5.7), A and B represent the induced birefringence from Kerr effect and electrostriction effect, respectively. Accordingly, $A/(A+B)$ stands for the contribution of the Kerr effect. To understand the

dependency of the contribution from Kerr effect on the electric field, we plot $A/(A+B)$ as a function of the applied electric field intensity in Figure 5.5. The ratio of $A/(A+B)$ remains almost unchanged at the weak field region. Interestingly, for each sample there is a critical electric field E_c , beyond which $A/(A+B)$ drops dramatically. Take Sample A (red solid squares) as an example, $A/(A+B)$ lies between 0.8 and 0.9 and it remains constant when $E < E_c = 4\text{V}/\mu\text{m}$. This implies that in the weak field region the LC local reorientation caused by Kerr effect plays a dominant role while electrostriction effect is relatively weak. However, when E exceeds E_c , the ratio of $A/(A+B)$ starts to drop, indicating the electrostriction effect starts making more significant contributions. This is due to the polymer networks and blue phase lattices are gradually deformed by strong electric field. This. For the sample with a higher polymer concentration, polymer networks are more rigid so that the electrostriction effect manifests beyond a higher critical field.

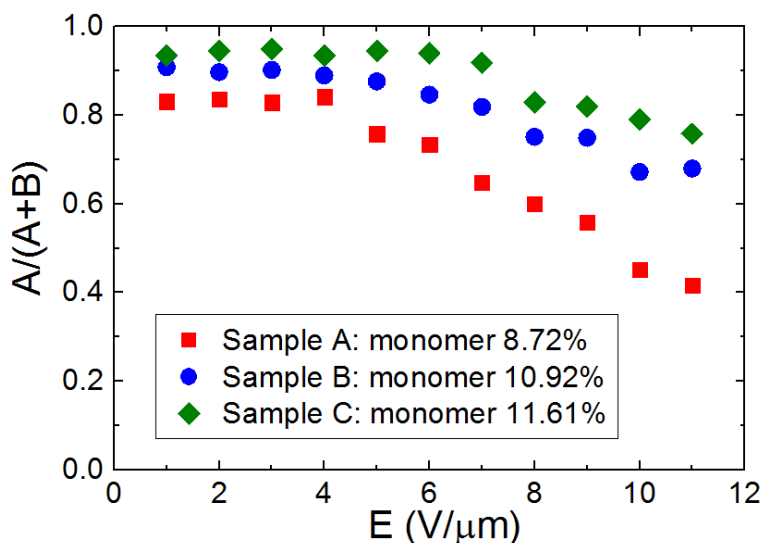


Figure 5.5. Contribution of Kerr effect when different electric fields are applied to samples with different monomer concentrations.

The critical field is not only the starting point of electrostriction effect, but also an onset for the phenomenon of hysteresis. We measured the hysteresis loops of each sample under different electric fields by ascending the voltage to a certain level and then descended it to zero. Due to the limitation of space, here

we only show the hysteresis curves of Sample A, but the other two samples exhibit the same trend. The measured hysteresis loops of Sample A under different electric fields of 3, 5 and 7 V/ μm are plotted in Figure 5.6. The solid and dashed lines represent the VT curves under forward and backward driving, respectively. From Figure 5.5, the critical field E_c is 4 V/ μm for Sample A. When E is lower than E_c , the forward and backward VT curves overlap well with each other and the hysteresis is unnoticeable. This means there is no deformation in polymer network and the electrostriction effect is negligible. However, when the electric field is increased to 5 V/ μm , which is higher than E_c , a small hysteresis is observed, indicating the polymer networks are deformed and electrostriction effect starts to manifest. As E continues to increase to 7V/ μm , the polymer networks are further deformed and lattice distortion becomes more severe, thus the hysteresis becomes even larger. An effective approach to suppress electrostriction and reduce hysteresis is to increase monomer concentration [105, 106]; however, the tradeoff is increased operation voltage.

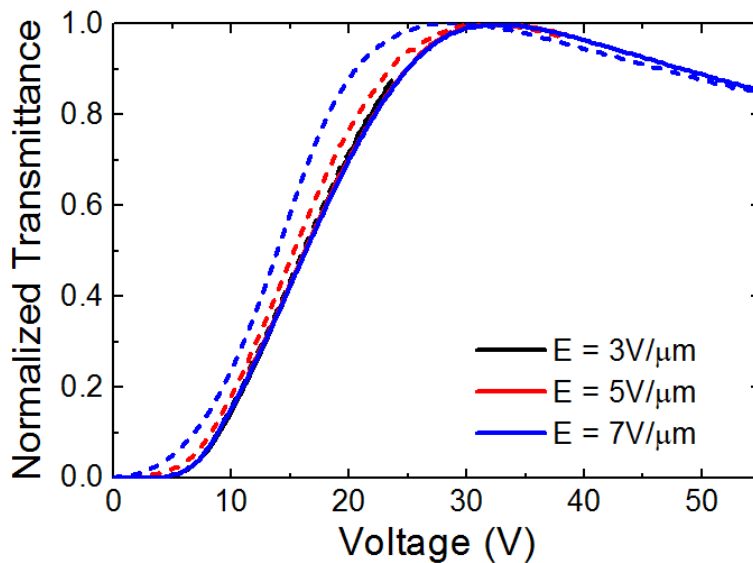


Figure 5.6. Hysteresis loops of Sample A under different electric fields (Solid lines: forward driving, dashed lines: backward driving; $\lambda = 633\text{nm}$).

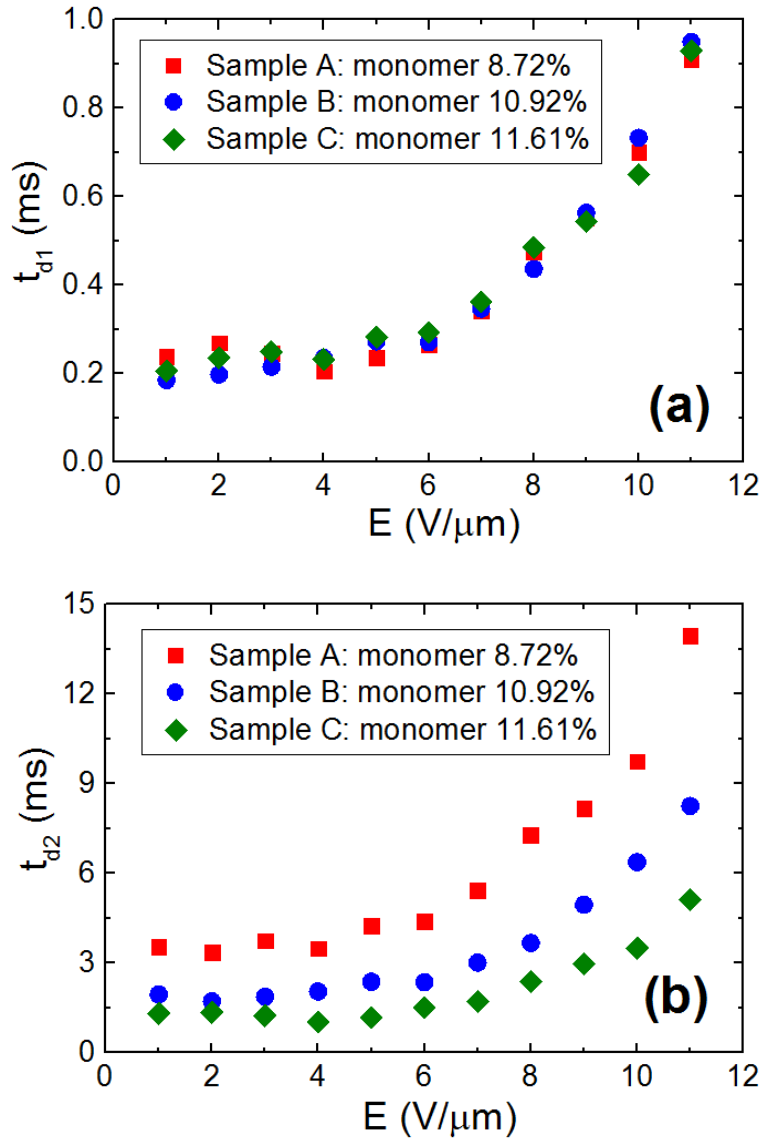


Figure 5.7. Fitted decay time constants of (a) Kerr effect t_{d1} and (b) electrostriction effect t_{d2} for samples with different monomer concentrations.

We also measure the transient decay process of all three samples under different electric fields, and fit the experimental data with Equation (5.8). Figures 5.7(a) and (b) plot the extracted decay time constants t_{d1} and t_{d2} under different electric fields. Similar to the rise time constant t_{r1} of Kerr effect, the decay time constant t_{d1} is also insensitive to the monomer concentration and only depends on the weight ratio between LC host and chiral dopant. According to Gerber's model [82], the characteristic response time of Kerr effect

is governed by rotational viscosity γ_1 , average elastic constant k , and pitch length P_0 as follows:

$$t_{d1} \sim \tau_0 = \frac{\gamma_1 P_0^2}{4\pi^2 k}. \quad (5.9)$$

Hence, t_{d1} remains almost the same for blue phase composites under same electric field as long as the ratio between LC host and chiral dopant does not change. However, in contrast to t_{r1} , t_{d1} increases as the electric field gets stronger. This is because the LC directors within double-twist cylinders are unwound more severely under a stronger electric field. Thereby, upon removal of electric field, it takes longer time for those LC directors to relax back to their original double-twist alignment, resulting in a longer decay time. The same trend applies to t_{d2} as well, and this explains why the decay time becomes slower when electric field gets stronger [95]. For blue phase liquid crystals with a higher monomer concentration, their polymer networks are more rigid and lattice less likely to be distorted, thus the relaxation time is faster upon removing the electric field.

In [Equation \(5.8\)](#), C and D represent the induced birefringence from Kerr effect and electrostriction effect, respectively. Therefore, similar to the analysis of rise process above, $C/(C+D)$ stands for the contribution of the Kerr effect. To understand the dependency of the contribution from Kerr effect on the electric field during the decay process, we also plotted $C/(C+D)$ as a function of the applied electric field intensity in [Figure 5.8](#). Same with the rise process, a critical electric field E_c also exists for the decay process. When the electric field is weaker than E_c , the reorientation of local LC directors within double-twist cylinders dominates. When E exceeds E_c , the contribution of electrostriction effect gradually increases. In Sample A, it reaches $\sim 50\%$ at $E = 11 \text{ V}/\mu\text{m}$, as [Figure 5.8](#) shows. For those samples with higher monomer concentrations, their E_c is higher and lattice distortion is less likely to occur so that the electrostriction effect is less severe. However, the required operation voltage is higher.

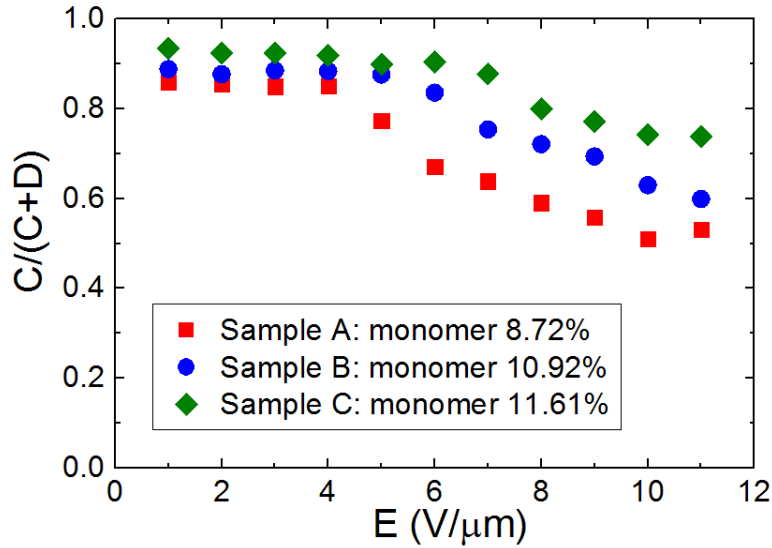


Figure 5.8. Contribution of Kerr effect when different electric fields are applied to samples with different monomer concentrations.

The double exponential model discussed above well characterize the mechanisms underlying dynamic responses of blue phase composites. From our analysis, both response time and hysteresis of blue phase liquid crystals increase as the applied field exceeds a critical point. Thus, it is essential to keep the electric field below the critical field in order to achieve fast response time and hysteresis-free performance. This serves as a useful guideline for future BPLC material development and device optimization. On the material side, higher monomer concentration can be used to form more stable polymer networks in order to suppress the electrostriction effect, but bear in mind that any excessive polymer would lead to an undesirable increase in operation voltage [105, 107]. Therefore, a delicate balance between response time, hysteresis and operation voltage need to be sought from the material development point of view. On the device side, it is strongly desired to keep the applied electric field below the critical field of the BPLC composite. For example, the sharp taper angle of the rectangular or trapezoid protrusions generates strong electric field at the edge of the electrodes [100]. To reduce the peak electric field, we can modify the trapezoid protrusion to elliptical shape so that the sharp taper angle becomes smooth.

In this way, the electrostriction is suppressed and hysteresis can be reduced.

5.4 Summary

In this chapter, we have proposed a double exponential model to characterize the dynamic response behavior of blue phase composites. This model well agrees with experimental results. Based on the model, we can quantitatively evaluate the contributions of Kerr and electrostriction effects of a blue phase composite under different electric fields. We find that electrostriction effect is the root cause for the observed slow response time and hysteresis under strong electric fields. Meanwhile, there is a critical field (E_c) determining the onset of electrostriction and hysteresis. When the applied electric field is below the critical field, Kerr effect dominates. As a result, the response time is usually within submillisecond range and hysteresis is negligible. Once the electric field exceeds the critical field, electrostriction effect gradually manifests. Under such a circumstance, response time gets slower and hysteresis becomes more severe. Our experimental results show that a higher polymer concentration helps suppress electrostriction and achieve faster response time, but the tradeoff is increased operation voltage. Thus, other approaches need to be sought in order to suppress the electrostriction effect, as will be discussed in next chapter.

CHAPTER 6. HYSTERESIS-FREE BLUE PHASE LIQUID CRYSTALS STABILIZED BY LINEAR PHOTO-POLYMERIZATION

As discussed in Chapter Five, the typical response time of Kerr effect is within submillisecond range, but the electrostriction effect usually takes several milliseconds or even longer to accomplish. When the electric field is below a critical field (E_c), the Kerr effect dominates. Consequently, the blue phase composite exhibits fast response time and negligible hysteresis. However, when the applied electric field exceeds E_c , electrostriction gradually manifests, leading both hysteresis and response time to increase dramatically. Hence, there is an urgent need for suppressing the electrostriction effect in order to achieve submillisecond response time and hysteresis-free blue phase liquid crystal devices.

In this chapter, we propose a method to suppress the electrostriction effect by polymerizing photopolymers with linearly polarized UV light instead of conventional unpolarized UV. We find that linear photo-polymerization (LPP) [108] can induce anisotropic polymer networks, leading to anisotropic electrostrictions with respect to the direction of applied electric fields. By setting the polarization direction of the crosslinking UV light perpendicular to the stripe electrodes of an IPS cell, the electrostriction effect is dramatically suppressed and consequently the hysteresis is reduced by ~20X.

6.1 Electric Field Effects

To form polymer networks for stabilizing the blue phase lattices, three types of monomers are commonly used [109]: a di-functional (e.g. RM257) monomer is mixed with a mono-functional (e.g. C12A: dodecyl acrylate) or a tri-functional monomer (e.g. TMPTA: 1,1,1-trimethylolpropane triacrylate) The chemical structures of these exemplary monomers are depicted in [Figure 6.1](#).

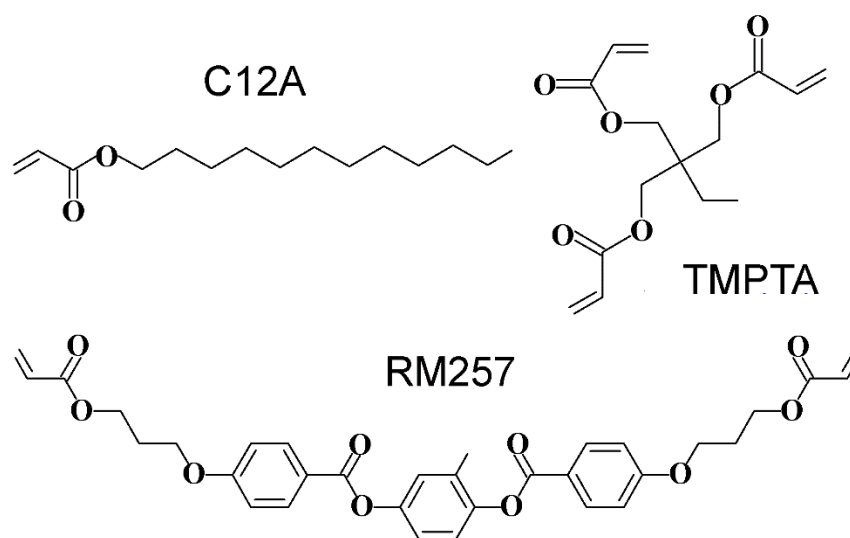


Figure 6.1. Chemical structures of monomers employed in our PS-BPLC.

Conventionally, unpolarized UV light is used in the polymerization process of monomers. However, it is widely known that the photo-crosslinking mechanism of monomers depends on the polarization of UV light [108, 110]. For instance, the crosslinking probability of a dichroic acrylate moiety is greater when exposed to UV light whose polarization axis is parallel to the double bonds instead of perpendicular. Therefore, by crosslinking double bonds of monomers with a linearly polarized UV light, anisotropy can be induced in the polymer networks. As discussed in last chapter, the severity of electrostriction mainly depends on the rigidity of polymer networks. Hence, by controlling the UV polarization axis with respect to the stripe electrodes of an IPS cell, the formed anisotropic polymer networks could result in anisotropic electrostrictions accordingly.

In our experiments, we employed a large $\Delta\epsilon$ nematic LC host JC-BP07N (JNC, Japan) [83] whose physical properties are: $\Delta n = 0.162$ at $\lambda = 633$ nm, $\Delta\epsilon = 302$ at 100 Hz and 22°C, and $T_c = 87^\circ\text{C}$. The blue phase precursor consists of 86.53 wt. % JC-BP07N, 2.82 wt. % chiral dopant R5011 (HCCH), 6.31 wt. % RM257 (Merck), 4.02 wt. % C12A (Sigma Aldrich) and 0.32 wt. % photoinitiator. The precursor was heated to an isotropic phase and then filled into IPS cells with cell gap $d \sim 7.3$ μm . The IPS cells

have interdigitated pixel electrodes on the bottom substrates (electrode width $W = 8\mu\text{m}$, electrode gap $G = 12\mu\text{m}$) without surface alignment layer. Next, the cells were placed on a Linkam temperature controllable stage, cooled to a temperature close to the chiral nematic and blue phase transition point, and then illuminated with UV light for 15 min ($\lambda \sim 365\text{nm}$, intensity 8 mW/cm^2). After UV exposure, the nanostructured BPLC composite was self-assembled. In the next step, the IPS cell was sandwiched between two crossed polarizers and a He-Ne laser was used as a probing beam ($\lambda = 633\text{ nm}$). The voltage-dependent transmitted light was focused by a lens so that multiple diffraction orders [75] were collected by the detector.

In order to investigate the effect of UV polarization on the electro-optic properties of blue phase composites, we first prepared three samples exposed under different UV polarization conditions. The directions of UV polarization were parallel and perpendicular to the stripe electrodes in Sample 1 and 2, respectively; whereas Sample 3 was cured by unpolarized UV light. Since temperature cooling rate and curing temperature play very important roles in determining the properties of polymer networks [111, 112], we kept these two parameters identical for all three samples. A linear UV polarizer was placed between the UV light source and IPS cell in all polarized UV exposure experiments, as shown in [Figure 6.2](#).

Some prior studies reported the electrostriction effect could be characterized by measuring the shift of Bragg reflection wavelength [101, 113]. In those experiments, the results were measured using LC cells with homogeneous alignment, in which the deformation of cubic lattice caused by the vertical electric field would shift the Bragg reflection wavelength. In contrast, the IPS cells employed in transmissive blue phase liquid crystal cells do not have any alignment layers, and the electric field is mainly along the lateral direction. Thus, the shift in Bragg reflection wavelength is negligible and very difficult to detect. Nevertheless, as discussed in last chapter, the degree of electrostriction effect can still be investigated from the hysteresis and dynamic response processes. In order to evaluate the severity of electrostriction, we

measured and compared the hysteresis as well as response time of these three samples. The hysteresis was measured by increasing the voltage to their individual peak transmittance and then sweeping it back to zero. To measure the rise time, we applied a voltage to the BPLC sample and recorded the transmittance change by a digital oscilloscope. Similarly, to measure decay time we removed the on-state voltage of the BPLC sample instantaneously and recorded the transient transmittance change.

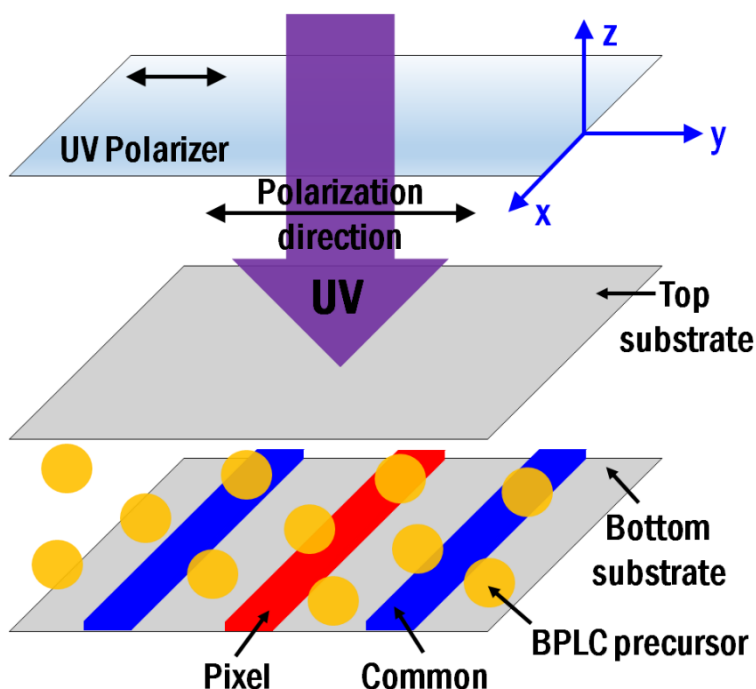


Figure 6.2. Experimental setup of curing process for LPP-stabilized blue phases.

6.2 Polarization Effect

6.2.1. Hysteresis

Figure 6.3 depicts the measured hysteresis loops of Samples 1-3 and their operation voltage and hysteresis are listed in Table 6.1. We can see that Sample 2 (UV polarization is perpendicular to the stripe IPS electrodes) exhibits a much lower hysteresis than Sample 3 (cured by unpolarized UV light).

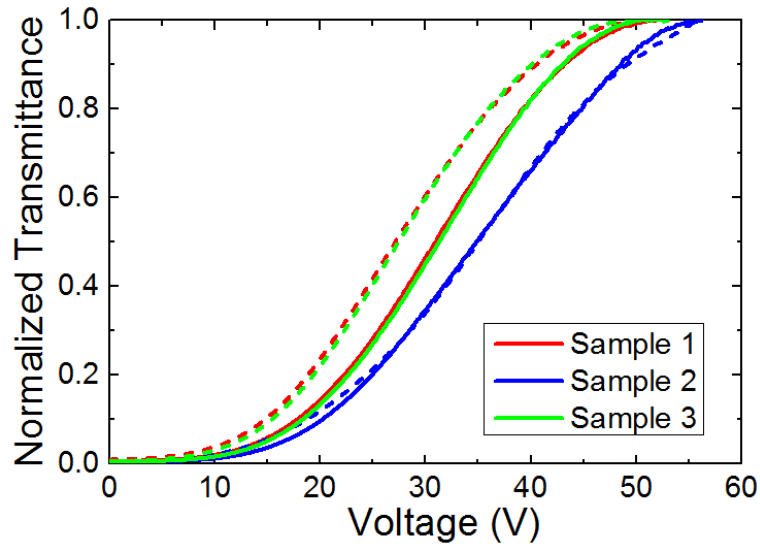


Figure 6.3. Measured hysteresis loops of Samples 1-3 (Solid lines: forward driving, dashed lines: backward driving; $\lambda = 633\text{nm}$).

The physical mechanisms underlying the observed differences are explained as follows. In the blue phase precursor containing C12A and RM257 monomers, the directional LPP photoreaction is parallel to the polarization axis of linearly polarized UV light. As a result, the formed polymer networks are more rigid along the UV polarization axis [108, 114]. The LPP-induced anisotropy in polymer networks of Samples 1 and 2 are sketched in Figures 6.4(a) and (b), respectively. In Sample 2, polymer networks are formed along the UV polarization direction; that is, parallel to the direction of the applied electric field, as Figure 6.4(b) illustrates. Thereby, the polymer networks are more robust against electric field-induced deformation along the LPP direction, leading to a suppressed electrostriction effect and consequently a reduced hysteresis. In contrast, for Sample 1, in which the UV polarization is parallel to the stripe electrodes, the polymer networks are mainly formed along the electrode direction, as shown in Figure 6.4(a), and therefore it is less robust along the direction of the applied electric field. As a result, the polymer networks, and more specifically, blue phase lattices, are more likely to be deformed by the applied electric field in the

configuration of Figure 6.4(a), resulting in a more severe electrostriction. This is indeed observed in Sample 1, which exhibits the largest hysteresis (7.56%) as depicted in Figure 6.3.

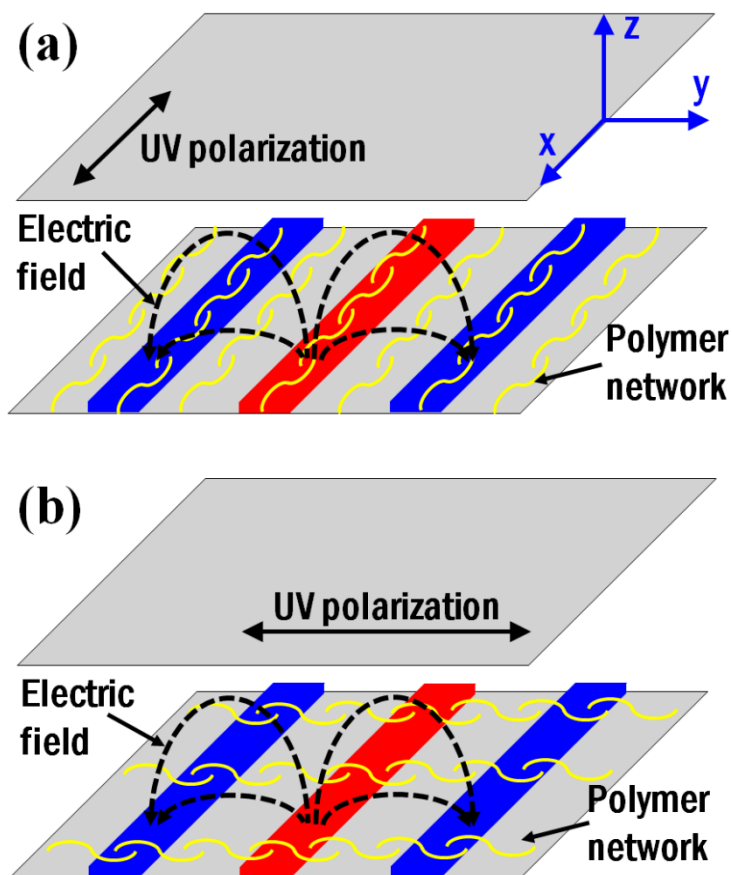


Figure 6.4. LPP-induced polymer network in (a) Sample 1 and (b) Sample 2.

Table 6.1. Measured operation voltage, hysteresis and response time of Samples 1-3.

	Sample 1	Sample 2	Sample 3
V_{on} (V)	51.8	56.2	53.0
Hysteresis	7.56%	0.36%	6.95%
τ_{rise} (μ s)	674.6	456.8	524.7
τ_{decay} (ms)	4.34	1.90	3.72

6.2.2. Dynamic Responses

On the other hand, among Samples 1-3, Sample 2 exhibits the fastest rise and decay times while Sample 1 is the slowest, as [Table 6.1](#) lists. To explain the difference, the double relaxation model is used to characterize the decay process [61]. As discussed in Chapter Five, this model well reveals the contributions of Kerr and electrostriction effects to the overall electro-optic properties of blue phase liquid crystals. In following experiments, each cell was driven to its own peak transmittance after which the voltage was removed instantaneously. The transient transmittance change was recorded by a digital oscilloscope. The measured change in transmittance T is related to the phase retardation φ by:

$$T = \sin^2(\varphi / 2). \quad (6.1)$$

The black solid line in [Figure 6.5](#) shows the measured transient phase retardation of Sample 2 during the decay process. Then the experimental data is fitted with following double relaxation equation [61]:

$$\varphi(t) = A_1 e^{-t/t_1} + A_2 e^{-t/t_2}, \quad (6.2)$$

where t_1 and t_2 are the average decay time constants while A_1 and A_2 are the phase retardations generated by the Kerr and electrostriction effect, respectively.

The fitting curve (magenta solid line) in [Figure 6.5](#) indicates that [Equation \(6.2\)](#) well describes the decay process of the phase retardation. The fitted time constants and the contribution of electrostriction effect, which is described by $A_2/(A_1 + A_2)$ in our model, are listed in [Table 6.2](#). All the values of t_1 lie in the submillisecond range while those of t_2 are around several milliseconds. These results well match the typical response time of fast Kerr effect and the slow electrostriction effect. Please note here that Sample 2 exhibits the fastest response time. This is due to the suppression of electrostriction by polarized crosslinking, which can be told from the lowest $A_2/(A_1 + A_2)$ ratio of Sample 2. However, from [Figure 6.4](#), the non-planar electric fields near the edges of planar stripe electrodes are still quite strong [100], thereby the electrostriction effect

is yet not negligible (16.9%). Nevertheless, compared to Sample 3 which is stabilized by unpolarized UV light, this ratio is reduced by more than 2X. By using protrusion electrodes instead of planar electrodes [100], the on-state voltage would drop to below 10V and the electrostriction effect should be completely suppressed. As a result, the response time should be in the submillisecond range over the entire driving voltage range.

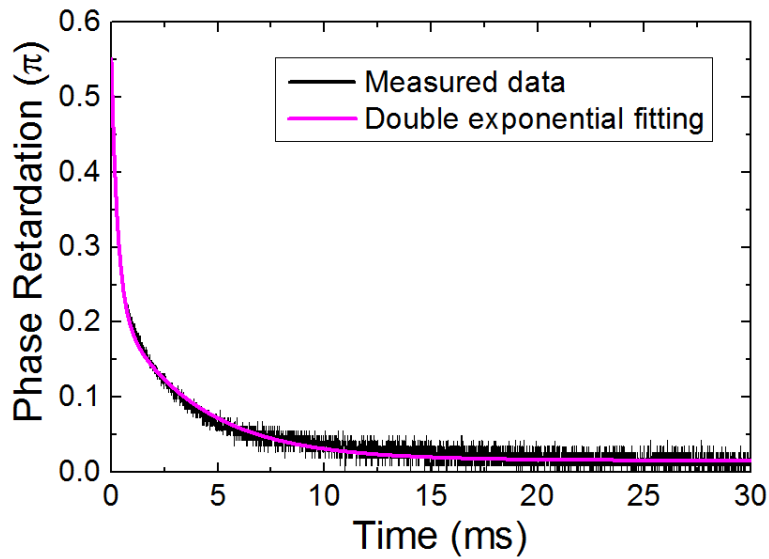


Figure 6.5. Transient decay process of Sample 2 at 56.2V.

Table 6.2. Fitted time constants and contribution of electrostriction effect for Samples 1-3.

	Sample 1	Sample 2	Sample 3
t_1 (ms)	0.51	0.27	0.39
t_2 (ms)	6.47	3.78	5.98
$A_2/(A_1 + A_2)$	43.8%	16.9%	38.7%

6.3 UV Intensity Effect

In addition, the illumination intensity of polarized UV light affects the rate the crosslinking process and consequently the anisotropy of polymer networks. Thus, UV intensity also plays an important role in

determining the performance of LPP. Using LPP-photoalignment, which employs polarized UV light to induce anisotropic LC-surface alignment [108], as an analogy, the induced surface anchoring of LPP-photoalignment is related to the intensity of the activating UV light [115]. This trend applies to polarized UV-polymerized blue phase composites as well.

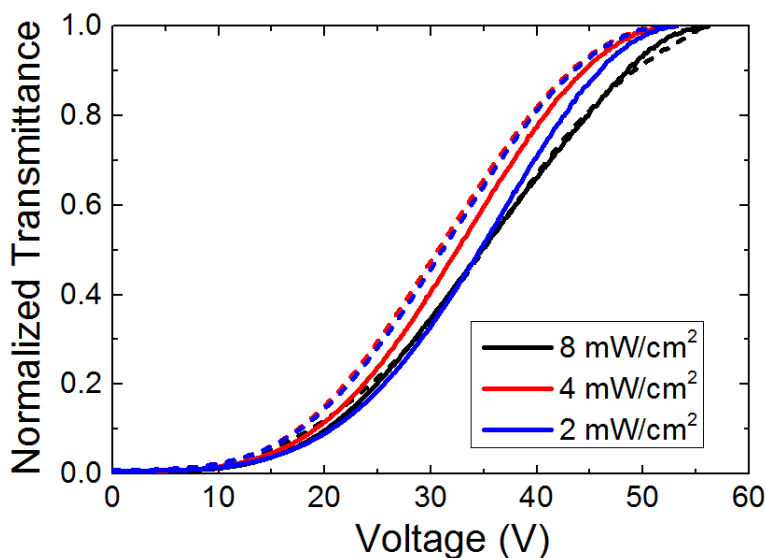


Figure 6.6. Hysteresis loops of IPS cells under different UV illumination intensities (Solid lines: forward driving, dashed lines: backward driving; $\lambda = 633\text{nm}$).

In order to investigate the effect of illumination intensity, we prepare two more samples using different UV exposure intensities in addition to Sample 2 for comparison. The UV dosage for all three samples is the same: 8 mW/cm^2 for 15 min, 4 mW/cm^2 for 30 min, and 2 mW/cm^2 for 60 min. The measured hysteresis loops of these three samples are plotted in Figure 6.6 and their operation voltages, hysteresis, and response times are listed in Table 6.3. As we can see, when UV exposure intensity increases, the response time becomes faster while the hysteresis is reduced, indicating that the electrostriction is suppressed. This trend is similar to the LPP process of azo-type monomers, in which the diffusion rate of linearly polarized pre-polymers is proportional to the illumination power according to a diffusion model of photopolymers [115]. Hence, here we use this model as an analogy to explain the correlation of UV

intensity and LPP-induced anisotropy in polymer networks. The higher diffusion rate under stronger UV illumination power expedites the anisotropic polymerization process, and accordingly induces a larger anisotropy in polymer networks. Consequently, stronger polymer networks are formed along the electric field direction, thus suppressing the electrostriction effect. In contrast, a lower UV illumination power leads to a lower anisotropy in polymer networks. Hence, a linearly polarized UV light with strong intensity is preferred in LPP-stabilization in order to induce a large anisotropy in polymer networks for the purpose of suppressing electrostriction effect.

Table 6.3. Measured operation voltage, hysteresis and response times of IPS cells under different UV illumination intensities.

UV Intensity	V_{on}	Hysteresis	τ_{rise} (μ s)	τ_{decay} (ms)
2 mW/cm ²	53.2V	6.79%	860.5	3.67
4 mW/cm ²	54.0V	3.40%	594.5	2.78
8 mW/cm ²	56.2 V	0.36%	456.8	1.90

6.4 Monomer Choice

Besides the monomer combination of RM257 and C12A discussed above, we also investigated the effect of LPP on the electro-optic properties of polymer-stabilized blue phase composites by using another monomer combination, namely the di-functional monomer RM257 and the tri-functional monomer TMPTA. The blue phase precursor consists of 86.90 wt. % JC-BP07N, 2.81 wt. % chiral dopant R5011, 5.98 wt. % RM257, 3.99 wt. % TMPTA and 0.32 wt. % photoinitiator. This time, we also prepared three IPS samples under different UV curing conditions. The directions of UV polarization were parallel and perpendicular to the stripe electrodes in Sample 4 and 5, respectively; whereas Sample 6 was illuminated by unpolarized UV light. All three samples are polymerized with the same UV dosage with: 8 mW/cm² for

15 minutes.

The measured hysteresis loops of these three samples are plotted in [Figure 6.7](#), and their operation voltage, hysteresis as well as response time are listed in [Table 6.4](#). Compared to the combination of RM257 and C12A, the samples comprising RM257 and TMPTA exhibit much faster response time. This originates from the fact that the tri-functional monomer TMPTA has three photo-crosslinking double bonds, which can form much stronger polymer network than the mono-functional monomer C12A. Nevertheless, these three samples do not exhibit large differences in terms of operation voltage, hysteresis and response time under different UV polarization directions. This is because the three photo-crosslinking double bonds of TMPTA are along different directions, thus rendering their polymer networks more likely to be isotropic no matter which direction is the UV light polarized along. Hence, in order to use the LPP stabilization for the purpose of suppressing electrostriction effect, the combination of monomer-functional and di-functional monomers should be chosen.

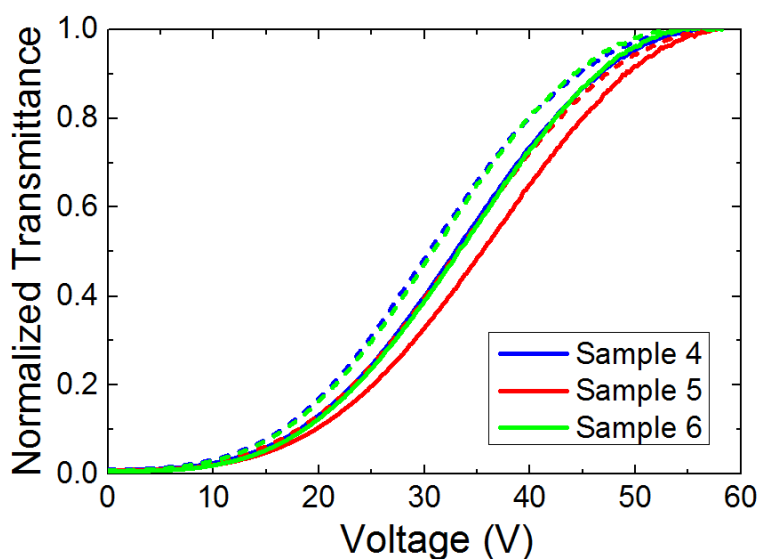


Figure 6.7. Measured hysteresis loops of Samples 4-6 (Solid lines: forward driving, dashed lines: backward driving; $\lambda = 633\text{nm}$).

Table 6.4. Measured operation voltage, hysteresis, and response time of Samples 4-6.

	V_{on}	Hysteresis	τ_{rise} (μs)	τ_{decay} (μs)
Sample 4	57.2 V	4.37%	362.9	958.4
Sample 5	58.0 V	3.97%	369.3	810.7
Sample 6	58.0 V	4.14%	345.8	871.5

6.5 Summary

In this chapter, we have proposed a method to suppress the electrostriction effect in polymer-stabilized blue phase liquid crystals via polymerizing photopolymers with linearly polarized UV light. By illuminating the mono-functional monomer C12A and the di-functional monomer RM257 with linearly polarized UV light, anisotropic polymer networks are formed, resulting in anisotropic electrostrictions. Linearly polarized UV with polarization direction perpendicular to the stripe electrodes strongly suppresses electrostriction. The resulting hysteresis of the driving voltage is reduced from 6.95% to 0.36% and the response times is reduced by a factor of two. To induce a higher anisotropy in polymer networks, a more powerful linearly polarized UV exposure is required. It is foreseeable that this method will provide a guideline for future manufacturing of the blue phase liquid crystal displays.

CHAPTER 7. SUMMARY

In this dissertation, we have investigated Kerr effect-based blue phase liquid crystal displays (BPLCDs). Compared to commonly employed nematic liquid crystals, blue phase liquid crystals (BPLCs) exhibit several attractive features: (1) self-assembled three-dimensional lattice structure so that no surface alignment layer is required; (2) optically isotropic voltage-off state which leads to high contrast ratio and wide viewing angle; (3) its electro-optical performance is insensitive to the cell gap, which is favorable for large-size panel fabrication and enabling touch panel functions, and (4) most attractively, its nanoscale double-twist cylinder diameter and short coherence length result in submillisecond response time. The fast response time not only reduces motion picture blurs but also enables color sequential displays. The elimination of spatial color filters triples optical efficiency and resolution density.

Nonetheless, there are still some technical challenges to overcome: high operation voltage, low optical transmittance and noticeable hysteresis. To solve these problems, efforts from both material development and device design sides should be made simultaneously.

The background knowledge of liquid crystal displays and blue phase are introduced in Chapter 1, following which the electro-optical properties of blue phase are discussed in Chapter 2. The device physics of Kerr effect-based blue phase LCDs are investigated. We build a numerical model based on the refraction effect for simulating the electro-optical characteristics of blue phase LCDs using in-plane-switching (IPS) structures. Our refraction model is more accurate than conventional model in computing the electro-optics of IPS structures and it well explains the electrode dimension effect. Parameters affecting the electro-optics of blue phase using IPS structures, such as electrode dimension, cell gap, saturated birefringence, and saturation field are

analyzed.

Based on the refraction model, Chapter 3 discusses approaches to achieve low operation voltage from device and material viewpoints. On the device side, with protrusion and etched electrodes, we can reduce the operating voltage to below 10V and enhance the optical transmittance to over 80%. On the material side, large Kerr constant is still helpful for lowering the operation voltage, but we also need to pay attention to the individual Δn and $\Delta \epsilon$ values of liquid crystal host according to the device structures employed. For small electrode dimension, liquid crystal host with a high birefringence is preferred because of the shallow electric field penetration depth. For large electrode dimension, high dielectric anisotropy is a better choice. High- $\Delta \epsilon$ LC hosts help enhance Kerr constant, leading to a reduced operation voltage; but they may be subject to serious TFT charging issues due to the huge dielectric anisotropy. This will provide important guidelines for future device design and material development.

The transmittance of protrusion and etched electrodes are limited to ~80% since the dead zones over the electrodes still cannot be eliminated. In order to compete with mainstream nematic LCDs, such as twisted nematic and fringe field switching modes, the transmittance of blue phase devices needs to be improved to over 90%. In Chapter 4, we propose a Z-shaped electrode structure for reducing the operating voltage and enhancing the transmittance of blue phase LCDs. By optimizing the device structure, we have successfully reduced the operating voltage to lower than 10V and improved optical transmittance to > 95% based on a lower- $\Delta \epsilon$ LC host not subjecting to charging issues. The performance is comparable to or even better than that of mainstream nematic LCDs. More attractively, this is the first device structure to achieve such a high transmittance in blue phase devices without using an oblique incident backlight. By using zigzag structure, the color shift and grayscale inversion are in unnoticeable range. With continuous development in LC

material development, the voltage can be further reduced.

In addition, hysteresis affects the accuracy of grayscale control and should be suppressed. Hysteresis usually occur when a strong electric field is applied to the blue phase cell. In order to investigate the generation mechanisms of hysteresis, we have proposed a double exponential model to analyze the dynamic responses of blue phase liquid crystals in Chapter 5. From this model, we can quantitatively evaluate the contribution of Kerr and electrostriction effects of blue phase liquid crystals under different electric fields. We find that electrostriction effect is the root cause for the observed slow response time and severe hysteresis under strong electric field. When the electric field is below a critical field, Kerr effect dominates. As a result, the response time is usually within submillisecond range and hysteresis is negligible. Once the electric field exceeds the critical field, electrostriction effect gradually manifests. Under such a circumstance, response time gets slower and hysteresis becomes more severe.

To suppress the electrostriction effect in blue phase, in Chapter 6 we introduce a method to stabilize the blue phase lattice via linear photo-polymerization. By illuminating the mono-functional and the di-functional monomers with a linearly polarized UV beam, we can form anisotropic polymer networks, which in turn lead to anisotropic electrostrictions. In experiments, we found that when the polarization of UV light is perpendicular to the stripe electrodes, the electrostriction effect can be strongly suppressed. The resulting hysteresis is reduced from 6.95% to 0.36% and response time is improved by a factor of two. To further reduce the electrostriction effect, a more powerful linearly polarized UV intensity can be employed since it helps induce a higher anisotropy in polymer networks.

In conclusion, the Kerr effect-based blue phase LCDs have been explored systematically in this dissertation. Efforts have been made on both device and material sides to improve the performance of the blue phase LCDs in terms of driving voltage, transmittance and hysteresis. The

approaches and studies presented would advance the blue phase LCDs to a new level and accelerate their emergence as next-generation displays. It is foreseeable that the widespread applications blue phase LCDs is near.

APPENDIX: STUDENT PUBLICATIONS

BOOK CHAPTER

1. **D. Xu**, F. Peng and S. T. Wu, “Polymer-Stabilized Blue Phase Liquid Crystals,” in the book “Handbook of Visual Display Technology (2nd Edition)” (Springer, 2015).

JOURNAL PUBLICATIONS

1. H. Chen, Y. Weng, **D. Xu**, N. V. Tabiryan, and S. T. Wu, “Beam steering for virtual/augmented reality displays with a cycloidal diffractive waveplate,” *Opt. Express* 24, 7287-7298 (2016).
2. Y. F. Lan, Y. Liu, P.J. Huang, **D. Xu**, C. Y. Tsai, C. H. Lin, N. Sugiura and S. T. Wu, “Non-ideal optical isotropy of blue phase liquid crystal and their self-assembly on electrode surface,” *Mol. Cryst. Liq. Cryst.* 610, 217-220 (2015).
3. (*Cover/feature article*) D. Franklin, Y. Chen, A. Vazquez-Guardado, S. Modak, J. Boroumand, **D. Xu**, S. T. Wu and D. Chanda, “Polarization-independent actively tunable colour generation on imprinted plasmonic surfaces,” *Nature Commun.* 6, 7337 (2015).
4. **D. Xu**, F. Peng, G. Tan, J. He and S. T. Wu, “A semi-empirical equation for the response time of in-plane switching liquid crystal display and measurement of twist elastic constant,” *J. Appl. Phys.* 117, 203103 (2015).
5. J. Yuan, G. Tan, **D. Xu**, F. Peng and S. T. Wu, “Low-voltage and fast-response polymer-stabilized hyper-twisted nematic liquid crystal,” *Opt. Mater. Express* 5, 1339-1347 (2015).
6. H. Chen, Z. Luo, **D. Xu**, F. Peng, S. T. Wu, et al. “A fast-response A-film-enhanced fringe field switching liquid crystal display,” *Liq. Cryst.* 42, 537-542 (2015).
7. **D. Xu**, G. Tan and S. T. Wu, “Large-angle and high-efficiency tunable phase grating using fringe field switching liquid crystal,” *Opt. Express* 23, 12274-12285 (2015).
8. **D. Xu**, H. Chen, S. T. Wu, et al. “A fringe field switching liquid crystal display with fast grayscale response time,” *J. Disp. Technol.* 11, 353-359 (2015).
9. F. Peng, **D. Xu**, H. Chen and S. T. Wu, “A low voltage polymer network liquid crystal for infrared spatial light modulators,” *Opt. Express* 23, 2361-2368 (2015).

10. **D. Xu**, F. Peng, H. Chen, J. Yuan, S. T. Wu, et al., “Image sticking in liquid crystal displays with lateral electric fields,” J. Appl. Phys. 116, 193102 (2014).
11. H. Chen, F. Peng, Z. Luo, **D. Xu**, S. T. Wu, et al. “High performance liquid crystal displays with a low dielectric constant material,” Opt. Mater. Express 4, 2262 (2014).
12. M. Xu, **D. Xu**, H. Ren, I. S. Yoo and Q. Wang, “An adaptive liquid lens with radial interdigitated electrode,” J. Opt. 16, 105601 (2014).
13. **D. Xu**, J. Yuan, M. Schadt and S. T. Wu, “Blue phase liquid crystals stabilized by linear photo-polymerization,” Appl. Phys. Lett. 105, 081114 (2014).
14. Y. Liu, S. Xu, **D. Xu**, J. Yan, Y. Gao and S. T. Wu, “A hysteresis-free polymer-stabilized blue phase liquid crystal,” Liq. Cryst. 41, 1339-1344 (2014).
15. **D. Xu**, J. Yan, J. Yuan, F. Peng, Y. Chen and S. T. Wu, “Electro-optic response of polymer-stabilized blue phase liquid crystals,” Appl. Phys. Lett. 105, 011119 (2014).
16. Y. F. Lan, Y. Liu, P. J. Huang, **D. Xu**, C. Y. Tsai, C. H. Lin, N. Sugiura and S. T. Wu, “Non-ideal optical isotropy of blue phase liquid crystal,” Appl. Phys. Lett. 105, 011903 (2014).
17. (*Invited paper, co-first author*) Z. Luo, **D. Xu**, and S. T. Wu, “Emerging quantum-dot-enhanced LCDs,” J. Disp. Technol. 10, 526-539 (2014).
18. J. Yan, **D. Xu**, H. C. Cheng, S. T. Wu, Y. F. Lan and C. Y. Tsai, “Turning film for widening the viewing angle of a blue phase liquid crystal display,” Appl. Opt. 52, 8840-8844 (2013).
19. **D. Xu**, Y. Chen, Y. Liu and S. T. Wu, “Refraction effect in an in-plane-switching blue phase liquid crystal cell,” Opt. Express 21, 24721-24735 (2013).
20. J. Yan, Y. Chen, **D. Xu** and S. T. Wu, “Angular dependent reflection of a monodomain blue phase liquid crystal,” J. Appl. Phys. 114, 113106 (2013).
21. Y. Chen, **D. Xu**, S. T. Wu, S. Yamamoto and Y. Haseba, “A low voltage and submillisecond-response polymer-stabilized blue phase liquid crystal,” Appl. Phys. Lett. 102, 141116 (2013).
22. Y. Liu, Y. F. Lan, H. Zhang, R. Zhu, **D. Xu**, S. T. Wu, et al. “Optical rotatory power of polymer-stabilized blue phase liquid crystals,” Appl. Phys. Lett. 102, 131102 (2013).

23. **D. Xu**, L. Rao, C. D. Tu and S. T. Wu, “Nematic liquid crystal display with submillisecond grayscale response time,” *J. Disp. Technol.* 9, 67-70 (2013).

CONFERENCE PROCEEDINGS

1. **D. Xu**, G. Tan, S. T. Wu, “Multi-angle beam steering for head-mounted displays.” in *SID Int. Symp. Digest Tech. Papers* **47** (2016).
2. **D. Xu**, F. Peng, G. Tan, et al. “A new single-cell measurement method for determining the twist elastic constant of liquid crystals,” in *SID Int. Symp. Digest Tech. Papers* **47** (2016).
3. **D. Xu**, H. Chen, S. T. Wu, et al. “Fast-response fringe field switching LCD with patterned common electrode,” in *SID Int. Symp. Digest Tech. Papers* **46**, 652-655 (2015).
4. **D. Xu**, F. Peng, H. Chen, J. Yuan, S. T. Wu, et al. “Image sticking reduction of fringe field switching LCDs,” in *SID Int. Symp. Digest Tech. Papers* **46**, 739-742 (2015).
5. **D. Xu**, J. Yuan, M. Schadt and S. T. Wu, “High performance blue phase liquid crystal displays stabilized by linear photopolymers,” in *SID Int. Symp. Digest Tech. Papers* **46**, 545-548 (2015).
6. (*Distinguished student paper*) H. Chen, Z. Luo, **D. Xu**, F. Peng, S. T. Wu, et al. “A fast-response A-film-enhanced fringe field switching LCDs,” in *SID Int. Symp. Digest Tech. Papers* **46**, 739-742 (2015).
7. J. Yuan, **D. Xu** and S. T. Wu, “An ultra-low voltage blue phase LCD for mobile applications,” in *SID Int. Symp. Digest Tech. Papers* **46**, 1520-1523 (2015).
8. F. Peng, **D. Xu**, H. Chen and S. T. Wu, “A low-voltage and fast-response infrared spatial light modulator,” in *SID Int. Symp. Digest Tech. Papers* **46**, 831-834 (2015).
9. (*Invited talk*) **D. Xu**, J. Yuan, M. Schadt, J. Yan and S. T. Wu, “Stabilizing blue phase liquid crystals with linearly polarized UV light,” in *Proc. SPIE* **9384**, 93840H-1 (2015).
10. (*Invited talk*) **D. Xu**, F. Peng and S. T. Wu, “Is polymer-stabilized blue phase liquid crystal ready for prime time?” in *10th SPSJ Intl. Polymer Conf.* (2014, Tsukuba, Japan).

11. *(Invited talk)* Z. Luo, Y. Chen, **D. Xu**, and S. T. Wu, "Is quantum-dot LCD ready for prime time?" in *IEEE Photonics Conference*, 40-41 (2014).
12. *(Distinguished student paper)* **D. Xu**, Y. Chen, Y. Liu, S. T. Wu, et al. "Low-voltage and high-transmittance blue phase liquid crystal displays," in *SID Int. Symp. Digest Tech. Papers* **45**, 168-171 (2014).
13. Y. Liu, S. Xu, **D. Xu**, J. Yan and S. T. Wu, "A hysteresis-free polymer-stabilized blue-phase liquid crystal," in *SID Int. Symp. Digest Tech. Papers* **45**, 176-179 (2014).
14. *(Distinguished student paper)* **D. Xu**, L. Rao, C. D. Tu and S. T. Wu, "A nematic LCD with submillisecond gray-to-gray response time", in *SID Int. Symp. Digest Tech. Papers* **44**, 435-438 (2013).
15. Y. Liu, H. Zhang, R. Zhu, **D. Xu**, S. T. Wu, et al. "Enhancing the contrast ratio of blue phase LCDs," in *SID Int. Symp. Digest Tech. Papers* **44**, 188-191 (2013).

US PATENT

1. J. Yan, **D. Xu**, H. C. Cheng, S. T. Wu, Y. F. Lan, C. Y. Tsai, "Optical film and display devices having the same," US Patent 9,121,999 B2 (Sep. 2015).

REFERENCES

- [1] J. H. Lee, D. N. Liu, and S. T. Wu, *Introduction to Flat Panel Displays* (Wiley, New York, 2008).
- [2] F. Reinitzer, "Beiträge zur kenntniss des cholestherins," *Monatsh. Chem.* **9**, 421-441 (1888).
- [3] P. G. de Gennes and J. Prost, *The Physics of Liquid Crystals*, 2nd ed. (Clarendon, Oxford, 1993).
- [4] P. Yeh and C. Gu, *Optics of Liquid Crystal Displays* (Wiley, New York, 1999).
- [5] D. K. Yang and S. T. Wu, *Fundamentals of Liquid Crystal Devices*, 2nd ed. (Wiley, Chichester, 2014).
- [6] G. H. Heilmeyer, L. A. Zanoni, and L. A. Barton, "Dynamic scattering: a new electrooptic effect in certain classes of nematic liquid crystals," in *Proc. IEEE* **56**, 1162-1171 (1968).
- [7] M. Schadt and W. Helfrich, "Voltage-dependent optical activity of a twisted nematic liquid crystal," *Appl. Phys. Lett.* **18**, 127-128 (1971).
- [8] T. J. Scheffer and J. Nehring, "A new, highly multiplexable liquid-crystal display," *Appl. Phys. Lett.* **45**, 1021-1023 (1984).
- [9] M. Schadt, "Liquid crystal materials and liquid crystal displays," *Annu. Rev. Mater. Sci.* **27**, 305-379 (1997).
- [10] R. A. Soref, "Transverse field effects in nematic liquid-crystals," *Appl. Phys. Lett.* **22**, 165-166 (1973).
- [11] A. Takeda, S. Kataoka, T. Sasaki, H. Chida, H. Tsuda, et al., "A super-high image quality multi-domain vertical alignment LCD by new rubbing-less technology," in *SID Int. Symp. Digest Tech. Papers* **29**, 1077-1080 (1998).
- [12] S. H. Lee, S. L. Lee, and H. Y. Kim, "Electro-optic characteristics and switching principle of a nematic liquid crystal cell controlled by fringe-field switching," *Appl. Phys. Lett.* **73**, 2881-2883 (1998).
- [13] D. H. Kim, Y. J. Lim, D. E. Kim, H. Ren, S. H. Ahn, et al., "Past, present, and future of

- fringe-field switching-liquid crystal display," *Liq. Cryst.* **15**, 99-106 (2014).
- [14] M. G. Craford, N. Holonyak, and F. A. Kish, "In pursuit of the ultimate lamp," *Sci. Am.* **284**, 62-67 (2001).
- [15] G. Harbers and C. Hoelen, "High performance LCD backlight using high intensity red, green and blue light emitting diodes," in *SID Int. Symp. Digest Tech. Papers* **32**, 702-705 (2001).
- [16] G. Harbers, W. Timmers, and W. Sillevs-Smitt, "LED backlighting for LCD HDTV," *J. Info. Disp. Soc.* **10**, 347-350 (2002).
- [17] M. F. Weber, C. A. Stover, L. R. Gilbert, T. J. Nevitt, and A. J. Ouderkirk, "Giant birefringent optics in multilayer polymer mirrors," *Science* **287**, 2451-2456 (2000).
- [18] R. C. Allen, L. W. Carlson, A. J. Ouderkirk, M. F. Weber, A. L. Kotz, et al., "Brightness enhancement film," U.S. Patent 6,111,696 (2000).
- [19] P. Watson and G. T. Boyd, "Backlighting of Mobile Displays," in *Mobile Displays: Technology and Applications*, 211-226 (Wiley, West Sussex, 2008).
- [20] S. H. Kim, J. D. Park, and K. D. Lee, "Fabrication of a nano-wire grid polarizer for brightness enhancement in liquid crystal display," *Nanotechnology* **17**, 4436-4438 (2006).
- [21] Z. Ge and S. T. Wu, "Nanowire grid polarizer for energy efficient and wide-view liquid crystal displays," *Appl. Phys. Lett.* **93**, 121104 (2008).
- [22] J. M. Jonza, M. F. Weber, A. J. Ouderkirk, and C. A. Stover, "Polarizing beam-splitting optical component," U.S. Patent 5,962,114 (1999).
- [23] Y. Li, T. X. Wu, and S. T. Wu, "Design optimization of reflective polarizers for LCD backlight recycling," *J. Disp. Technol.* **5**, 335-340 (2009).
- [24] S. Aratani, H. Klausmann, M. OhE, M. Ohta, K. Ashizawa, et al., "Complete suppression of color shift in in-plane switching mode liquid crystal displays with a multidomain structure obtained by unidirectional rubbing," *Jpn. J. Appl. Phys.* **36**, L27-L29 (1997).
- [25] H. Mori, "The wide view (WV) film for enhancing the field of view of LCDs," *J. Disp. Technol.* **1**, 179-186 (2005).

- [26] X. Zhu, Z. Ge, and S. T. Wu, "Analytical solutions for uniaxial-film-compensated wide-view liquid crystal displays," *J. Disp. Technol.* **2**, 2-20 (2006).
- [27] P. de Greef and H. G. Hultz, "Adaptive dimming and boosting backlight for LCD-TV systems," in *SID Int. Symp. Digest Tech. Papers* **38**, 1332-1335 (2007).
- [28] H. J. Peng, W. Zhang, C. K. Hung, C. J. Tsai, K. W. Ng, et al., "High contrast LCD TV using active dynamic LED backlight," in *SID Int. Symp. Digest Tech. Papers* **38**, 1336-1338 (2007).
- [29] Z. Luo, D. Xu, and S. T. Wu, "Emerging quantum-dots-enhanced LCDs," *J. Disp. Technol.* **10**, 526-539 (2014).
- [30] R. Zhu, Z. Luo, H. Chen, Y. Dong, and S. T. Wu, "Realizing Rec. 2020 color gamut with quantum dot displays," *Opt. Express* **23**, 23680-23693 (2015).
- [31] T. Serikawa, S. Shirai, A. Okamoto, and S. Suyama, "Low-temperature fabrication of high-mobility poly-Si TFTs for large-area LCDs," in *SID Int. Symp. Digest Tech. Papers* **30**, 137-141 (1989).
- [32] M. Kimura, I. Yudasaka, S. Kanbe, H. Kobayashi, H. Kiguchi, et al., "Low-temperature polysilicon thin-film transistor driving with integrated driver for high-resolution light emitting polymer display," *IEEE Trans. Electron Devices* **46**, 2282-2288 (1999).
- [33] K. Nomura, H. Ohta, A. Takagi, T. Kamiya, M. Hirano, et al., "Room-temperature fabrication of transparent flexible thin-film transistors using amorphous oxide semiconductors," *Nature* **432**, 488-492 (2004).
- [34] J. H. Lee, D. H. Kim, D. J. Yang, S. Y. Hong, K. S. Yoon, et al., "World's largest (15-inch) XGA AMLCD panel using IGZO oxide TFT," in *SID Int. Symp. Digest Tech. Papers* **39**, 625-628 (2008).
- [35] T. Kurita, "Moving picture quality improvement for hold-type AM-LCDs," in *SID Int. Symp. Digest Tech. Papers* **32**, 986-989 (2001).
- [36] J. Miseli, "Motion artifacts," in *SID Int. Symp. Digest Tech. Papers* **35**, 86-89 (2004).
- [37] J. Someya and H. Sugiura, "Evaluation of liquid-crystal-display motion blur with moving-

- picture response time and human perception," in *SID Int. Symp. Digest Tech. Papers* **15**, 79-86 (2007).
- [38] H. Haseba and S. Kobayashi, "A full-color sequential LCD using modulated backlight," in *SID Int. Symp. Digest Tech. Papers* **16**, 81-83 (1985).
- [39] F. C. Lin, Y. P. Huang, C. M. Wei, and H. P. D. Shieh, "Color-breakup suppression and low-power consumption by using the Stencil-FSC method in field-sequential LCDs," *J. Soc. Inf. Disp.* **17**, 221-228 (2009).
- [40] S. T. Wu and U. Efron, "Optical-properties of thin nematic liquid-crystal cells," *Appl. Phys. Lett.* **48**, 624-626 (1986).
- [41] M. Jiao, Z. Ge, Q. Song, and S. T. Wu, "Alignment layer effects on thin liquid crystal cells," *Appl. Phys. Lett.* **92**, 061102 (2008).
- [42] S. T. Wu, "Nematic liquid crystal modulator with response time less than $100\mu\text{s}$ at room temperature," *Appl. Phys. Lett.* **57**, 986-988 (1990).
- [43] H. Nakamura and K. Sekiya, "Overdrive method for reducing response times of liquid crystal displays," in *SID Int. Symp. Digest Tech. Papers* **32**, 1256-1259 (2001).
- [44] P. J. Bos and K. R. Beran, "The pi-cell: a fast liquid-crystal optical-switching device," *Mol. Cryst. Liq. Cryst.* **113**, 329-339 (1984).
- [45] T. Miyashita, Y. Yamaguchi, and T. Uchida, "Wide-viewing-angle display mode using bend-alignment liquid-crystal cell," *Jpn. J. Appl. Phys.* **34**, L177-L179 (1995).
- [46] S. Gauza, X. Zhu, W. Piecek, R. Dabrowski, and S. T. Wu, "Fast switching liquid crystals for color-sequential LCDs," *J. Disp. Technol.* **3**, 250-252 (2007).
- [47] H. Chen, M. Hu, F. Peng, J. Li, Z. An, et al., "Ultra-low viscosity liquid crystals," *Opt. Mater. Express* **5**, 655-660 (2015).
- [48] A. Saupe, "On molecular structure and physical properties of thermotropic liquid crystals," *Mol. Cryst. Liq. Cryst.* **7**, 59-74 (1969).
- [49] S. Meiboom, J. P. Sethna, P. W. Anderson, and W. F. Brinkman, "Theory of the blue phase cholesteric liquid crystals," *Phys. Rev. Lett.* **46**, 1216-1219 (1981).

- [50] R. J. Miller and H. F. Gleeson, "Order parameter measurements from the Kossel diagrams of the liquid-crystal blue phases," *Phys. Rev. E* **52**, 5011-5016 (1995).
- [51] P. P. Crooker, "Blue Phases," in *Chirality in Liquid Crystals*, 186-222 (Springer, New York, 2001).
- [52] A. Yoshizawa, "Material design for blue phase liquid crystals and their electro-optical effects," *RSC Adv.* **3**, 25475-25497 (2013).
- [53] J. Kerr, "A new relation between electricity and light: dielectrified media birefringent," *Philos. Mag.* **50**, 337-348 (1875).
- [54] H. Kikuchi, M. Yokota, Y. Hisakado, H. Yang, and T. Kajiyama, "Polymer-stabilized liquid crystal blue phases," *Nature Mater.* **1**, 64-68 (2002).
- [55] J. Yan, L. Rao, M. Jiao, Y. Li, H. C. Cheng, et al., "Polymer-stabilized optically isotropic liquid crystals for next-generation display and photonics applications," *J. Mater. Chem.* **21**, 7870-7877 (2011).
- [56] Z. Ge, S. Gauza, M. Jiao, H. Xianyu, and S. T. Wu, "Electro-optics of polymer-stabilized blue phase liquid crystal displays," *Appl. Phys. Lett.* **94**, 101104 (2009).
- [57] Z. Ge, L. Rao, S. Gauza, and S. T. Wu, "Modeling of blue phase liquid crystal displays," *J. Disp. Technol.* **5**, 250-256 (2009).
- [58] H. C. Cheng, J. Yan, T. Ishinabe, and S. T. Wu, "Vertical field switching for blue-phase liquid crystal devices," *Appl. Phys. Lett.* **98**, 261102 (2011).
- [59] H. C. Cheng, J. Yan, T. Ishinabe, N. Sugiura, C. Y. Liu, et al., "Blue-phase liquid crystal displays with vertical field switching," *J. Disp. Technol.* **8**, 98-103 (2012).
- [60] L. Rao, Z. Ge, S. T. Wu, and S. H. Lee, "Low voltage blue-phase liquid crystal displays," *Appl. Phys. Lett.* **95**, 231101 (2009).
- [61] D. Xu, J. Yan, J. Yuan, F. Peng, Y. Chen, et al., "Electro-optic response of polymer-stabilized blue phase liquid crystals," *Appl. Phys. Lett.* **105**, 011119 (2014).
- [62] C. D. Tu, C. L. Lin, J. Yan, Y. Chen, P. C. Lai, et al., "Driving scheme using bootstrapping method for blue-phase LCDs," *J. Disp. Technol.* **9**, 3-6 (2013).

- [63] M. Kim, M. S. Kim, B. G. Kang, M. K. Kim, S. Yoon, et al., "Wall-shaped electrodes for reducing the operation voltage of polymer-stabilized blue phase liquid crystal displays," *J. Phys. D: Appl. Phys.* **42**, 235502 (2009).
- [64] L. Rao, H. C. Cheng, and S. T. Wu, "Low voltage blue-phase LCDs with double-penetrating fringe fields," *J. Disp. Technol.* **6**, 287-289 (2010).
- [65] M. Jiao, Y. Li, and S. T. Wu, "Low voltage and high transmittance blue-phase liquid crystal displays with corrugated electrodes," *Appl. Phys. Lett.* **96**, 011102 (2010).
- [66] C. Y. Tsai, T. J. Tseng, L. Y. Wang, F. C. Yu, Y. F. Lan, et al., "Polymer-stabilized blue phase liquid crystal displays applying novel groove cell structure," in *SID Int. Symp. Digest Tech. Papers* **44**, 182–183 (2013).
- [67] L. Rao, J. Yan, S. T. Wu, S. Yamamoto, and Y. Haseba, "A large Kerr constant polymer-stabilized blue phase liquid crystal," *Appl. Phys. Lett.* **98**, 081109 (2011).
- [68] M. Wittek, N. Tanaka, D. Wilkes, M. Bremer, D. Pauluth, et al., "New materials for polymer-stabilized blue phase," in *SID Int. Symp. Digest Tech. Papers* **43**, 25–28 (2012).
- [69] Y. Chen, D. Xu, S. T. Wu, S. Yamamoto, and Y. Haseba, "A low voltage and submillisecond-response polymer-stabilized blue phase liquid crystal," *Appl. Phys. Lett.* **102**, 141116 (2013).
- [70] Y. Haseba, S. Yamamoto, K. Sago, A. Takata, and H. Tobata, "Low-voltage polymer-stabilized blue-phase liquid crystals," in *SID Int. Symp. Digest Tech. Papers* **44**, 254-257 (2013).
- [71] K. M. Chen, J. Yan, S. T. Wu, Y. P. Chang, C. C. Tsai, et al., "Electrode dimension effects on blue-phase liquid crystal displays," *J. Disp. Technol.* **7**, 362-364 (2011).
- [72] H. Kikuchi, "Liquid Crystalline Blue Phases," in *Structure and Bonding* **128**, 99-117 (Springer, Berlin, 2008).
- [73] J. Yan, H. C. Cheng, S. Gauza, Y. Li, M. Jiao, et al., "Extended Kerr effect of polymer-stabilized blue-phase liquid crystals," *Appl. Phys. Lett.* **96**, 071105 (2010).
- [74] M. Bass, C. DeCusatis, J. Enoch, V. Lakshminarayanan, G. Li, et al., *Handbook of Optics:*

Geometrical and Physical Optics, Polarized Light, Components and Instruments, 3rd ed. (McGraw-Hill, New York, 2010).

- [75] J. Yan, Y. Li, and S. T. Wu, "High-efficiency and fast-response tunable phase grating using a blue phase liquid crystal," *Opt. Lett.* **36**, 1404-1406 (2011).
- [76] S. W. Choi, S. Yamamoto, Y. Haseba, H. Higuchi, and H. Kikuchi, "Optically isotropic-nanostructured liquid crystal composite with high Kerr constant," *Appl. Phys. Lett.* **92**, 043119 (2008).
- [77] C. Y. Tsai, F. C. Yu, Y. F. Lan, P. J. Huang, S. Y. Lin, et al., "A novel blue phase liquid crystal display applying wall-electrode and high driving voltage circuit," in *SID Int. Symp. Digest Tech. Papers* **46**, 542-544 (2015).
- [78] S. Yoon, M. Kim, M. S. Kim, B. G. Kang, M. K. Kim, et al., "Optimisation of electrode structure to improve the electro-optic characteristics of liquid crystal display based on the Kerr effect," *Liq. Cryst.* **37**, 201-208 (2010).
- [79] J. Y. Yang, J. I. Lee, J. J. Kim, Y. K. Hwang, and J. H. Park, "Submicron pixel electrode structure in IPS mode," in *SID Int. Symp. Digest Tech. Papers* **43**, 876-878 (2012).
- [80] M. Jiao, J. Yan, and S. T. Wu, "Dispersion relation on the Kerr constant of a polymer-stabilized optically isotropic liquid crystal," *Phys. Rev. E* **83**, 041706 (2011).
- [81] Y. Li, M. Z. Jiao, and S. T. Wu, "Transflective display using a polymer-stabilized blue-phase liquid crystal," *Opt. Express* **18**, 16486-16491 (2010).
- [82] P. R. Gerber, "Electro-optical effects of a small-pitch blue-phase system," *Mol. Cryst. Liq. Cryst.* **116**, 197-206 (1985).
- [83] F. Peng, Y. Chen, J. Yuan, H. Chen, S. T. Wu, et al., "Low temperature and high frequency effects on polymer-stabilized blue phase liquid crystals with large dielectric anisotropy," *J. Mater. Chem. C* **2**, 3597-3601 (2014).
- [84] F. C. Frank, "I. Liquid crystals. On the theory of liquid crystals," *Discuss. Faraday Soc.* **25**, 19-28 (1958).
- [85] L. M. Blinov, *Electro-optical and Magneto-optical Properties of Liquid Crystals* (Wiley,

New York, 1983).

- [86] G. Wyszecki and W. S. Stiles, *Color Science: Concepts and Methods, Quantitative Data and Formulae*, 2nd ed. (Wiley, New York, 1982).
- [87] R. Lu, Q. Hong, Z. Ge, and S. T. Wu, "Color shift reduction of a multi-domain IPS-LCD using RGB-LED backlight," *Opt. Express* **14**, 6243-6252 (2006).
- [88] J. S. Steckel, J. Ho, C. Hamilton, J. Q. Xi, C. Breen, et al., "Quantum dots: the ultimate down-conversion material for LCD displays," *J. Info. Disp. Soc.* **23**, 294-305 (2015).
- [89] L. Rao, Z. Ge, and S. T. Wu, "Zigzag electrodes for suppressing the color shift of Kerr effect-based liquid crystal displays," *J. Disp. Technol.* **6**, 115-120 (2010).
- [90] S. S. Kim, B. H. Berkeley, K. H. Kim, and J. K. Song, "New technologies for advanced LCD-TV performance," *J. Soc. Info. Disp.* **12**, 353-359 (2004).
- [91] D. Xu, Y. Chen, Y. Liu, and S. T. Wu, "Refraction effect in an in-plane-switching blue phase liquid crystal cell," *Opt. Express* **21**, 24721-24735 (2013).
- [92] P. Bos, T. Buzak, and R. Vatne, "A full-color field sequential color display," in *SID Int. Symp. Digest Tech. Papers* **26**, 157-161 (1985).
- [93] C. H. Chen, F. C. Lin, Y. T. Hsu, Y. P. Huang, and H. P. D. Shieh, "A field sequential color LCD based on color fields arrangement for color breakup and flicker reduction," *J. Disp. Technol.* **5**, 34-39 (2009).
- [94] Y. Chen, J. Yan, J. Sun, S. T. Wu, X. Liang, et al., "A microsecond-response polymer-stabilized blue phase liquid crystal," *Appl. Phys. Lett.* **99**, 201105 (2011).
- [95] K. M. Chen, S. Gauza, H. Xianyu, and S. T. Wu, "Submillisecond gray-level response time of a polymer-stabilized blue-phase liquid crystal," *J. Disp. Technol.* **6**, 49-51 (2010).
- [96] V. Fréedericksz and V. Zolina, "Forces causing the orientation of an anisotropic liquid," *Trans. Faraday Soc.* **29**, 919-930 (1933).
- [97] H. J. Coles and H. F. Gleeson, "Electric-field induced phase-transitions and color switching in the blue phases of chiral nematic liquid-crystals," *Mol. Cryst. Liq. Cryst.* **167**, 213-225 (1989).

- [98] V. E. Dmitrienko, "Electro-optic effects in blue phases," *Liq. Cryst.* **5**, 847-851 (1989).
- [99] H. S. Kitzerow, P. P. Crooker, S. L. Kwok, J. Xu, and G. Heppke, "Dynamics of blue-phase selective reflections in an electric-field," *Phys. Rev. A* **42**, 3442-3448 (1990).
- [100] L. Rao, J. Yan, S. T. Wu, Y. C. Lai, Y. H. Chiu, et al., "Critical field for a hysteresis-free BPLC device," *J. Disp. Technol.* **7**, 627-629 (2011).
- [101] H. Yoshida, S. Yabu, H. Tone, Y. Kawata, H. Kikuchi, et al., "Secondary electro-optic effect in liquid crystalline cholesteric blue phases," *Opt. Mater. Express* **4**, 960-968 (2014).
- [102] J. Yan, D. Xu, H. C. Cheng, S. T. Wu, Y. F. Lan, et al., "Turning film for widening the viewing angle of a blue phase liquid crystal display," *Appl. Opt.* **52**, 8840-8844 (2013).
- [103] Y. Liu, Y. F. Lan, H. Zhang, R. Zhu, D. Xu, et al., "Optical rotatory power of polymer-stabilized blue phase liquid crystals," *Appl. Phys. Lett.* **102**, 131102 (2013).
- [104] J. Yan, Y. Chen, S. T. Wu, S. H. Liu, K. L. Cheng, et al., "Dynamic response of a polymer-stabilized blue-phase liquid crystal," *J. Appl. Phys.* **111**, 063103 (2012).
- [105] J. Yan and S. T. Wu, "Effect of polymer concentration and composition on blue phase liquid crystals," *J. Disp. Technol.* **7**, 490-493 (2011).
- [106] Y. F. Lan, C. Y. Tsai, J. K. Lu, and N. Sugiura, "Mechanism of hysteresis in polymer-network stabilized blue phase liquid crystal," *Polymer* **54**, 1876-1879 (2013).
- [107] J. Zhu, S. Ni, C. Chen, X. Song, C. Chen, et al., "The influence of polymer system on polymer-stabilised blue phase liquid crystals," *Liq. Cryst.* **41**, 891-896 (2014).
- [108] M. Schadt, K. Schmitt, V. Kozinkov, and V. Chigrinov, "Surface-induced parallel alignment of liquid-crystals by linearly polymerized photopolymers," *Jpn. J. Appl. Phys.* **31**, 2155-2164 (1992).
- [109] G. Nordendorf, A. Hoischen, J. Schmidtke, D. Wilkes, and H.-S. Kitzerow, "Polymer-stabilized blue phases: promising mesophases for a new generation of liquid crystal displays," *Polym. Adv. Tech.* **25**, 1195-1207 (2014).
- [110] M. Schadt, H. Seiberle, and A. Schuster, "Optical patterning of multidomain liquid-crystal displays with wide viewing angles," *Nature* **381**, 212-215 (1996).

- [111] C. Y. Fan, H. C. Jau, T. H. Lin, F. C. Yu, T. H. Huang, et al., "Influence of polymerization temperature on hysteresis and residual birefringence of polymer stabilized blue phase LCs," *J. Disp. Technol.* **7**, 615-618 (2011).
- [112] S. Ni, J. Zhu, J. Tan, X. Sun, E. Zhong, et al., "Critical temperature in phase transition of blue phase liquid crystal," *Opt. Mater. Express* **3**, 928-934 (2013).
- [113] S. Y. Lu and L. C. Chien, "Electrically switched color with polymer-stabilized blue-phase liquid crystals," *Opt. Lett.* **35**, 562-564 (2010).
- [114] D. Xu, J. Yuan, M. Schadt, and S. T. Wu, "Blue phase liquid crystals stabilized by linear photo-polymerization," *Appl. Phys. Lett.* **105**, 081114 (2014).
- [115] V. Chigrinov, S. Pikin, A. Verevochnikov, V. Kozenkov, M. Khazimullin, et al., "Diffusion model of photoaligning in azo-dye layers," *Phys. Rev. E* **69**, 061713 (2004).